CATION EXCHANGE MECHANISM OF DIVALENT METALS IONS IN SYNTHETIC NaX AND LTA ZEOLITES: EFFICIENCY AND SELECTIVITY

Zeinab Ezzeddine[a,b]*, Isabelle Batonneau-Gener[a] and Yannick Pouilloux[a]

Keywords: : NaX zeolite; LTA zeolite; exchange mechanism; heavy metals; selectivity.

In this investigation, the removal of divalent heavy metals by two types of zeolites has been studied. The mechanism of cation exchange for Cu^{2+}, Ni^{2+}, Cd^{2+} and Pb^{2+} on NaX Faujasite and Linde type A (LTA) zeolites was studied. Both zeolites are very efficient in divalent heavy metals removal from water. Ion exchange isotherms were performed and the thermodynamic parameters were calculated as well. Kielland plots showed that the order of selectivity is not the same for both the zeolites. For NaX it followed the following order $Pb^{2+} > Cu^{2+} > Cd^{2+} > Ni^{2+}$ while for LTA the order is $Pb^{2+} > Cd^{2+} > Cu^{2+} > Ni^{2+}$. Exchange velocity ($k_w$) and the radii of the hydrated metals ions are involved in determining this order of selectivity.

* Corresponding Authors
Fax:
E-Mail: zeinab.ezzeddine@univ-poitiers.fr
[a] Institut de chimie des milieux et matériaux de Poitiers (IC2MP) - UMR 7285, Poitiers University, Poitiers, France
[b] Platform for research and analysis in environmental sciences, Lebanese University, Lebanon

Introduction

Zeolites are cation exchangers that occur naturally, the Swedish mineralogist Axel Fredrick Crønstedt first discovered them in 1756.[1] The framework of zeolites is a three-dimensional arrangement of tetrahedral SiO_4 and AlO_4^- units. The aluminate units in the framework are responsible for its net negative charge which is balanced by the presence of extra framework cations located on defined crystallographic positions. These cations are responsible for zeolite exchange properties and the rich ion-exchange chemistry of these materials. The elevated cation exchange capacity made zeolite attractive for wastewater treatment especially for removing heavy metals.

Nowadays, many water resources are contaminated due to the direct release of industrial influents. Heavy metals are one of the most serious environmental pollutants since they accumulate in living organisms even at low concentration causing dangerous diseases.[2] Natural zeolites have been used to remove heavy metal from aqueous solutions because they are inexpensive and highly abundant. Several researches showed that zeolites have good cation-exchange capacities under different experimental conditions.[3-5] One of The most frequently studied natural zeolites is Clinoptilolite.[6,7] The cation exchange capacity is usually between 0.6 and 2.3 meq g^{-1}.[8] Recently, a great deal of attention has been paid to synthetic zeolites due to their enhanced properties including higher cation exchange capacity compared to natural ones. Synthetic Faujasite zeolite, NaX ($Na_{88}Al_{88}Si_{104}O_{384}$ and Si/Al ratio = 1.18) and Zeolite A, LTA ($Na_{96}Al_{96}Si_{96}O_{384}$ and Si/Al ratio=1) are more favourable for heavy metals adsorption since they contain more exchangeable Na^+ ions in their framework.

There are several studies dealing with divalent heavy metals adsorption onto synthetic zeolites,[9,10] but no detailed analysis for the cation exchange mechanism is available. The current study highlights the theory of ion exchange in synthetic NaX and LTA zeolites. The efficiency and selectivity of divalent heavy metals binding (Cu^{2+}, Ni^{2+}, Cd^{2+} and Pb^{2+}) were analyzed in detail based on the cation exchange theory including calculation of thermodynamic parameters which allows better understanding the selectivity of these zeolites toward metal ions.

Experimental

Materials

The French Institute of Petroleum (IFP Energie Nouvelle) provided the synthetic NaX Faujasite and LTA zeolite samples. These samples were used as received without any further chemical modification. Copper nitrate trihydrate ($Cu(NO_3)_2.3H_2O$), cadmium nitrate tetrahydrate ($Cd(NO_3)_2.4H_2O$), nickel nitrate hexahydrate ($Ni(NO_3)_2.6H_2O$) and anhydrous lead nitrate ($Pb(NO_3)_2$) were purchased from Sigma Aldrich, and used as received. Ultrapure water was used throughout.

Batch adsorption experiments

Metal ions solutions (Cu^{2+}, Ni^{2+}, $Pb^{2+}$and Cd^{2+}) were prepared from their corresponding nitrate salts in ultrapure water to obtain solutions of different concentrations. In batch studies, 20 mg of the solid zeolite powder was placed in 100 mL of a metal solution of desired concentration. For obtaining the isotherms, the initial metal ions concentrations were varied between 0.17 mmol L^{-1} and 5 mmol L^{-1}. The solutions were stirred for 120 min at 25 °C then filtered by a 0.45 µm syringe filter and the remaining metal ions were measured by AAS (Perkin Elmer AA200). The adsorption capacity (mmol g^{-1}) of the adsorbent at equilibrium was calculated by eqn. (1).

$$q_e = \frac{(C_0 - C_e)V}{m} \quad (1)$$

where

C_0 is the initial concentration

C_e is the concentration at equilibrium,

V is the volume of metal solution in litre and

m is the mass of the adsorbent in g.

Theory of cation exchange in zeolites

The sodium–divalent metal ion exchange process in zeolite can be expressed by eqn. (2)

$$2\overline{Na}^+ + M^{2+} \leftrightarrows 2Na^+ + \overline{M}^{2+} \quad (2)$$

The bar above the symbols represents the ion exchanger phase. The thermodynamic equilibrium constant, K, of the reversible ion-exchange reaction is defined by eqn. (3).[11]

$$K = \frac{[[Na]^+]^2 \bar{X}_M \gamma_{Na}{}^2 f_M}{[M^{2+}] \bar{X}_{Na}{}^2 \gamma_M f_{Na}{}^2} \quad (3)$$

$[Na^+]$ and $[M^{2+}]$ are the molarities of the ions in solution, γ_i and f_i are the activity coefficients in the aqueous phase and in the ion-exchanger phase, respectively. The standard states for the ion-exchanger phase are taken as the exchanger in its pure Na^+ and M^{2+} forms, and the activity coefficients, f_{Na} and f_M, are chosen as unity when the exchanger is at the standard state of the Na^+ form and the M^{2+} form, respectively. $\bar{X}_i$ is an equivalent fraction of ion i in the ion-exchanger phase, defined by Eqns. (4) and (5).

$$\bar{X}_{Na} = \frac{[\overline{Na}^+]}{2[\overline{M}^{2+}] + [\overline{Na}^+]} \quad (4)$$

$$\bar{X}_M = \frac{2[\overline{M}^{2+}]}{2[\overline{M}^{2+}] + [\overline{Na}^+]} \quad (5)$$

The equivalent fractions of the ions in the solution (X_i) can replace the molarities $[Na^+]$ and $[M^{2+}]$ leading to eqns. (6 – 8).

$$X_{Na} = \frac{2[Na^+]}{2[M^{2+}] + [Na^+]} \quad (6)$$

$$X_M = \frac{2[M^{2+}]}{2[M^{2+}] + [Na^+]} \quad (7)$$

$$[Na^+] + 2[M^{2+}] = TN \quad (8)$$

where TN represents the total normality of the solution. By using a corrected selectivity coefficient, K_{Na}^M, the thermodynamic equilibrium constant can be rewritten eqn. (9).[12]

$$K_{Na}^M = \frac{X_{Na}{}^2 \bar{X}_M \gamma_{Na}{}^2}{X_M \bar{X}_{Na}{}^2 \gamma_M} [2(TN)] \quad (9)$$

where,

$$K = K_{Na}^M \frac{f_M}{f_{Na}{}^2} \quad (10)$$

When the total normality, TN= $[Na^+] + 2[M^{2+}]$, is lower than 0.01 N, γ^2_{Na}/γ_M will be close to unity. K_{Na}^M depends on the total normality. When the corrected selectivity coefficient is larger than unity ($\ln K_{Na}^M > 0$), the zeolite is selective for the ion M^{2+}. If K_{Na}^M is smaller than unity ($\ln K_{Na}^M < 0$), Na^+ ions are more preferred. When K_{Na}^M is equal to unity ($\ln K_{Na}^M = 0$), there will be no preference between these ions. K_{Na}^M is also related to the Kielland coefficient as given below. Kielland plots show the details of the ion exchange selectivity as a function of the equivalent fraction $\bar{X}_M$.

$$\log K_{Na}^M = \sum_{m=1} (m+1) C_m \bar{X}_M^m + \log(K_{Na}^M)_{\bar{X}_{M \to 0}} \quad (11)$$

The coefficient, C_m, is called generalized Kielland coefficient. These plots often give linear relationships with a slope $2C_1$.

$$\log K_{Na}^M = 2C_1 \bar{X}_M + \log(K_{Na}^M)_{\bar{X}_{m \to 0}} \quad (12)$$

If the Gibbs–Duhem equation is applied to the ion-exchange reaction, the thermodynamic equilibrium constant, K, is given by the integration of Kielland plot from $\bar{X}_M = 0$ to $\bar{X}_M = 1$.

$$\ln K = (Z_{Na} - Z_M) + \int_0^1 \ln K_{Na}^M \, d\bar{X}_M + \Delta \quad (13)$$

Thus, the thermodynamic equilibrium constant is determined by the valences of the exchanged and exchanging cations, the generalized Kielland coefficient C_1 and the intercept of Kielland plot, $\left(K_{Na}^M\right)_{\bar{X}_{M \to 0}}$.

The Gibbs standard free energy change $\Delta G°$ can be calculated by eqn. (14).

$$\Delta G^0 = -RT \ln K \quad (14)$$

Results and Discussion

Exchange equilibrium curves for NaX Zeolite

The exchange isotherms are shown in Figure 1 and are represented as the equivalent fraction of the divalent metal ions fraction ($\bar{X}_M$) inside the NaX zeolite as a function of the equivalent ion fraction in the solution (X_M).

The obtained exchange isotherms almost have the same shape, they showed a steeper increase in the initial stage of $X_M{}^{2+} < 0.2$ and then the isotherms increased more gently. This shape is characteristic of a favourable exchange process.

For $2Na^+ \rightarrow Pb^{2+}$ exchange reaction, the isotherm proceeds more steeply up to $\bar{X}_{Pb}$ ~0.6 which indicates higher selectivity for Pb^{2+} than for the other three heavy metals (Figure 1). The theoretical exchange capacity was calculated from the Na^+ ions contained in NaX ($Na_{88}Al_{88}Si_{104}O_{384}$). 1 g of NaX zeolite contains 6.54 mmol Na^+, so theoretically, it has a maximum adsorption capacity for divalent ions equals to 3.27 mmol g^{-1} since every two Na^+ ions are exchanged for

one divalent metal cation so this value was supposed to be the theoretical exchange capacity of NaX. The ion exchange capacities for all metal ions were determined from their corresponding isotherms and were found to be 93, 87, 95, and 96% of the theoretical exchange capacity for Cu^{2+}, Ni^{2+}, Cd^{2+} and Pb^{2+} respectively. These values were calculated from the equivalent fraction of cations in zeolite when the maximum exchange capacity was reached.

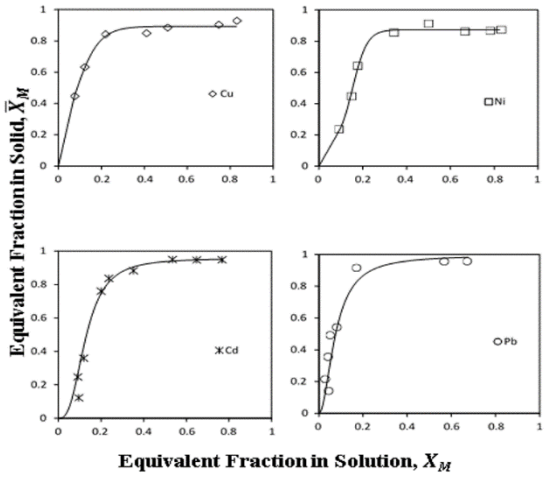

Figure 1. Cation exchange isotherm for $2Na^+ \rightarrow M^{2+}$ (M= Cu, Ni, Cd and Pb) exchange on the NaX zeolite.

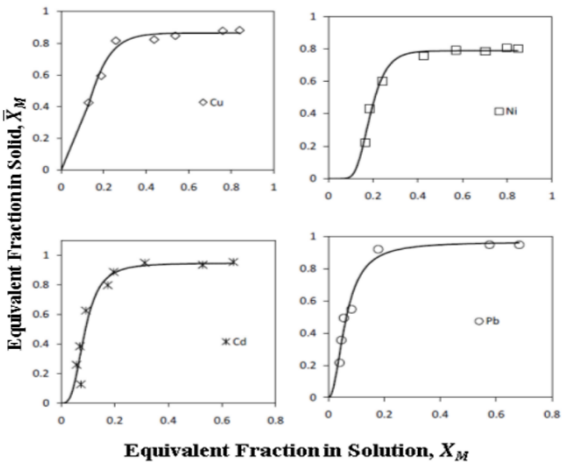

Figure 2. Cation exchange isotherm for $2Na^+ \rightarrow M^{2+}$ (M= Cu, Ni, Cd and Pb) exchange on the LTA zeolite.

Exchange Equilibrium Curves for LTA Zeolite

The exchange reactions of the four heavy metals ions Cu^{2+}, Ni^{2+}, Cd^{2+} and Pb^{2+} were done for LTA zeolite as well under the same conditions. The corresponding isotherms are shown in Figure 2. As in the case of NaX zeolite, the exchange isotherms for LTA showed a favourable exchange process with a steep increase in the initial stage of $X_M{}^{2+} < 0.2$ that proceeds more gently afterwards. Similarly, for $2Na^+ \rightarrow Pb^{2+}$ exchange reaction, the isotherm proceeded more steeply up to $\bar{X}_{Pb}$ ~0.6 which indicates higher selectivity for Pb^{2+} than for the other three heavy metals. The theoretical exchange capacity was calculated from the Na^+ ions contained in LTA ($Na_{96}Al_{96}Si_{96}O_{384}$). 1 g of LTA zeolite contains 7 mmol Na^+. So theoretically, it has a maximum adsorption capacity for divalent ions equals to 3.5 mmol g^{-1} since every two Na^+ ions are exchanged for 1 metal divalent cation so this value was supposed to be the theoretical exchange capacity of LTA. The ion exchange capacities for all were determined from their corresponding isotherms and were found to be 88, 82, 96, and 95% of the theoretical exchange capacity for Cu^{2+}, Ni^{2+}, Cd^{2+} and Pb^{2+} respectively. These values were calculated from the equivalent fraction of cations in zeolite when the maximum exchange capacity was reached.

Cation exchange selectivities: $2Na^+ \rightarrow M^{2+}$

The selectivity of both NaX and LTA zeolites is further analyzed through Kielland plots where the logarithm of the selectivity coefficient is plotted as a function of the equivalent fraction of cations in zeolites (X_M).

Table 1. Thermodynamic data for $2Na^+ \rightarrow M^{2+}$ exchange on NaX at 25 °C.

M^{2+}	$\ln\left(K_{Na}^{M}\right)_{\bar{X}_{M\rightarrow 0}}$	C_1	ΔG^0 (kJ mol^{-1})
Cu^{2+}	2.32	1.10	-5.80
Ni^{2+}	1.69	1.50	-4.20
Cd^{2+}	1.77	1.70	-4.40
Pb^{2+}	2.65	1.60	-6.40

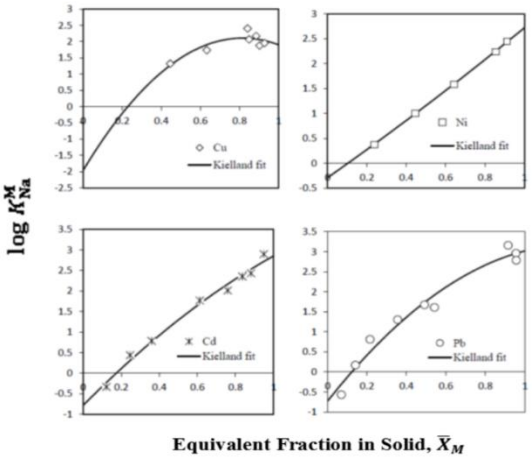

Figure 3. Kielland plots for $2Na^+ \rightarrow M^{2+}$ (M= Cu, Ni, Cd and Pb) exchange on the NaX zeolite.

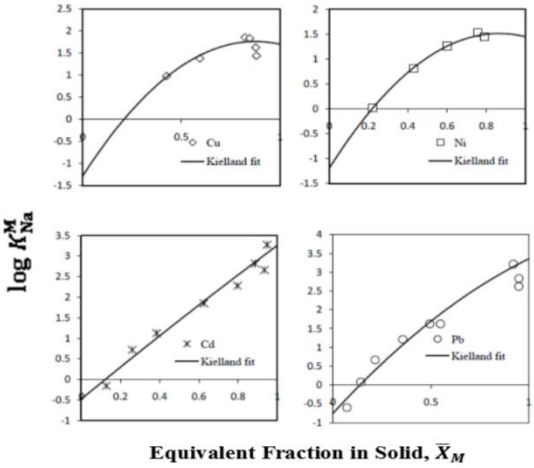

Figure 4. Kielland plots for $2Na^+ \rightarrow M^{2+}$ (M= Cu, Ni, Cd and Pb) exchange on the LTA zeolite.

The Kielland plots are represented in figure 3 and 4 for NaX and LTA respectively. The plots gave a linear relation for all metals except for Cu^{2+}. The line at 0 indicates that the corrected selectivity coefficient is equal to unity ($K_{Na}^{M} = 1$) where there is no preference between Na^{+} and M^{2+} ions. If the plots fall below this line this means that the zeolite is more selective for Na^{+} while if they fall above it this indicates that the zeolite is more selective for M^{2+}. From these Kielland plots, it can be deduced that for Cd^{2+} and Pb^{2+} ions the zeolite becomes more selective for the metal ions at $\bar{X}_M > 0.2$ since all Kielland plots fall above the 0 line above this value. For Cu^{2+} and Ni^{2+}, M^{2+} ions are more preferred almost throughout the $2Na^{+} \rightarrow M^{2+}$ exchange reaction. From the Kielland plots, the Kielland coefficient C_1, and ΔG^0 values were estimated. The obtained values are listed in Table 1.

For NaX, ΔG^0 value for Pb^{2+} was the smallest while that of Ni^{2+} was the highest. Based on this results, the order of selectivity will be $Pb^{2+} > Cu^{2+} > Cd^{2+} > Ni^{2+}$ which is in accordance with what was found before using the distribution coefficient K_d. The Kielland coefficient, C_1, is related to the energy of the steric limitation or jumping barrier for the exchanging ions in the sodalite cages. In general, the energy term for the steric limitation is larger as the $|C1|$ value is larger. For NaX zeolite, the energy of the steric limitation increases in the order of $Cd^{2+} > Pb^{2+} > Ni^{2+} > Cu^{2+}$ but the order of selectivity didn't follow the same order. These findings are related to the nature of the metal ions and mainly to the exchange velocities between the ligands and the aqueous metal ions which is generally expressed as eqn. (15).[13]

$$(Me(H_2O)_m)^{n+} + L \leftrightarrows (Me(H_2O)_{m-1}L)^{n+} + H_2O \qquad (15)$$

where L represents H_2O or other ligands and Me the metal ion. The exchange velocity constant (k_w) of water molecules with metallic ions (Table 2) is the fundamental step controlling the rate of ions removal from water.

Table 2. The exchange velocity constant (k_w) and Hydrated ionic radius (R) for the four studied metal ions.

Cation	$k\_w(s^{-1})$	R (nm)
Ni^{2+}	3.10^4	0.302
Cd^{2+}	3.10^8	0.275
Cu^{2+}	1.10^9	0.297
Pb^{2+}	7.10^9	0.261

Table 3. Thermodynamic data for $2Na^{+} \rightarrow M^{2+}$ exchange on LTA at 25 °C.

M^{2+}	$\ln(K_{Na}^{M})_{\bar{X}_{M\rightarrow 0}}$	C_1	ΔG^0 (kJ mol^{-1})
Cu^{2+}	1.6	0.870	-4.162
Ni^{2+}	0.985	1.27	-2.44
Cd^{2+}	2.27	1.85	-5.62
Pb^{2+}	2.60	2.07	-6.45

The obtained selectivity results vary with the order of the exchange velocity (k_w) values which seem to be the main parameter that controls their adsorption. Pb^{2+} has the greatest exchange velocity (k_w) so it is the first to be adsorbed while Ni^{2+} has the lowest k_w value so its adsorption is less favorable compared to Pb^{2+}, Cu^{2+} and Cd^{2+}.

For LTA zeolite, the energy of the steric limitation increases in the order of $Pb^{2+} > Cd^{2+} > Ni^{2+} > Cu^{2+}$ (Table 3) but the order of selectivity didn't also follow the same order. The order of selectivity according to ΔG^0 values will be $Pb^{2+} > Cd^{2+} > Cu^{2+} > Ni^{2+}$. LTA is more selective for Pb^{2+} and less selective for Ni^{2+} like in the case of NaX zeolite but the selectivity of Cu^{2+} and Cd^{2+} is reversed. So in the case LTA zeolite, the selectivity might be affected by the radii of the hydrated metal ions (Table 2) in addition to exchange velocity (k_w) since the pore size of LTA are smaller than that of NaX zeolite.

Conclusions

NaX and LTA zeolites were found to be very efficient in the removal of heavy metals from water. The theory of cation exchange was applied in order to understand the mechanism of heavy metals adsorption. For both zeolites, Kielland plots showed that Cd^{2+} and Pb^{2+} have higher selectivity over Ni^{2+} at $\bar{X}_M > 0.2$ while for Cu^{2+} and Ni^{2+}, M^{2+} ions are more preferred almost throughout the $2Na^{+} \rightarrow M^{2+}$ exchange reaction.

For NaX, the order of selectivity is $Pb^{2+} > Cu^{2+} > Cd^{2+} > Ni^{2+}$ while for LTA the selectivity order is $Pb^{2+} > Cd^{2+} > Cu^{2+} > Ni^{2+}$. This order was directly controlled by exchange velocity (k_w) for NaX and the radii of the hydrated metal ions for LTA.

References

[1]Bekkum, V. H., Flanigen, E. M., Jacobs, P. A., Jansen. J. C., *Introduction to Zeolite Science and Practice*, 2nd Revised Edn, Elsevier, Amsterdam, **1991**; Crønstedt, A. F., *Kongl Svenska Vetenskaps Acadademiens Handlingar*. **1756**, *17*, 120.

[2]Fu, F., Wang, Q., *J. Environ. Manage.*, **2011**, *92*, 407-418. https://doi.org/10.1016/j.jenvman.2010.11.011

[3]Motsi, T., Rowson, N. A., Simmons. M. H., *Int. J. Miner. Process*, **2009**, *92*, 42-48. https://doi.org/10.1016/j.minpro.2009.02.005

[4]Ostroski, I., Barros, M., Silva, E., Dantas, J., Arroyo, P., Lima, O., *J. Hazard. Mater.*, **2009**, *161*, 1404-1412. https://doi.org/10.1016/j.jhazmat.2008.04.111

[5]Taffarel, S. R., Rubio. J., *Miner. Eng.*, **2009**, *22*, 336-343. https://doi.org/10.1016/j.mineng.2008.09.007

[6]Inglezakis, V. J., Styliano, M. A., Gkantzou, D., Loizidou. M. D., *Desalination*, **2007**, *210*, 248-256. https://doi.org/10.1016/j.desal.2006.05.049

[7]Athanasiadis, K., Helmreich. B., *Water Res.*, **2005**, *39*, 1527-1532. https://doi.org/10.1016/j.watres.2005.01.024

[8]Wang, S. Peng. Y., *Chem. Eng. J.*, **2010**, *156*, 11–24. https://doi.org/10.1016/j.cej.2009.10.029

[9]Nibou, D., Mekatel, H., Amokrane, S., Barkat, M., Trari, M., *J. Hazard. Mater.*, **2010**, *173*, 637–646. https://doi.org/10.1016/j.jhazmat.2009.08.132

[10]Hui, K.S., Chao, C.Y.H., Kot, S.C., *J. Hazard. Mater.*, **2005**, *127*, 89–101. https://doi.org/10.1016/j.jhazmat.2005.06.027

[11]Kodama, T., Komarneni, S., *J. Mater. Chem*., **1999**, *9*, 533–539. http://dx.doi.org/10.1039/A806758I

[12]Barrer, R. M., Klinowski, J., *J. Chem. Soc., Faraday Trans. 1*., **1974**, *70*, 2080. http://dx.doi.org/10.1039/F19747002080

[13]Sigg, L., Behra, P., Stumm, W., *Chimie des milieu aquatiques*, 5th Edition, Dunod, Paris, **2014**.

Received: 10.04.2018.
Accepted: 28.05.2018.

MODELING OF THE FUNCTION OF THE OZONE CONCENTRATION DISTRIBUTION OF SURFACE TO URBAN AREAS

Amaury de Souza,[a]* Soetânia S. de Oliveira,[b] Flavio Aristone,[a] Zaccheus Olaofe,[c] Shiva Prashanth Kumar Kodicherla,[d] Milica Arsić,[e] Nabila Ihaddadene[f] and Ihaddadene Razika[g]

Keywords: Ozone distribution of probability, air monitoring, Weibull distribution.

In large urban centers, the major contributors to much of the degradation of air quality are motor vehicles on the road. In some cities, the levels of concentrations of air pollutants have reached levels that pose a risk to human health. Ozone (O_3) is a secondary pollutant formed from photochemical reactions of nitrogen oxides (NO_x). Numerous studies have found associations between daily levels of ozone with a number of health effects. In the state of South Mato Grosso (MS), there has been a growing increase of ozone levels in the atmosphere in recent years. Considering the above, this study aimed to identify the best estimator for the Weibull distribution, in analyzing the ozone concentration, for the city of Campo Grande-MS. For this, electronic data from the continuous air monitoring station located on the campus of the Federal University of South Mato Grosso (UFMS), Campo Grande was utilized. According to the results presented by the tests, it was verified that the LSRM method presented the poorest performance. The EPFM, MOM and MSDM are most efficient methods to adjust the Weibull distribution curves for the evaluation of ozone concentrations in the atmosphere.

*Corresponding Authors
E-Mail: amaury.de@uol.com.br
[a] Universidade Federal de Mato Grosso do Sul, Campo Grande, MS, Brasil
[b] University of Campina Grande, PB, Brazil.
[c] University of Cape Town: Rondebosch, Western cape, South Africa
[d] Department of Civil Engineering, Room No. EB 577, Engineering Building (EB), Xi'an Jiaotong-Liverpool University (XJTLU), Suzhou Industrial Park, Suzhou, P. R. China.
[e] University of Belgrade, Technical faculty in Bor, Serbia.
[f] Department of Mechanical Engineering, M'Sila University, B.P 166 Ichbelia, M'Sila 28000, Algeria.
[g] Department of Mechanics, Mohamed Boudiaf University, M'sila, Algeria.

Introduction

Ozone (O_3) and nitrogen oxides (NO_x) comprising of nitrogen dioxide (NO_2) and nitric oxide (NO) are among the most important contaminants in urban areas as they have adverse effects on human health and the natural environment. The main source of NOx in urban areas is the exhaustion of motor vehicles. The main proportion of NOx is emitted as NO, while a smaller proportion is emitted directly as NO_2. Even if the concentration of NOx has a downward trend, NO_2 share in NOx emissions has increased in recent years and depends on vehicle type fuel technology, exhaust treatment technology and the driving conditions.[1]

In South Mato Grosso, measurement of ozone concentration at ground level began in 2004. The ozone concentration has shown an increasing trend in the state of South Mato Grosso since the first measurements took place in 2004, and this has been the main pollutant in many areas of the state.[2-4]

Since most existing policies to reduce tropospheric levels of O_3 in urban areas focus on reducing precursor emissions, their success depends heavily on an accurate development of the sensitivity of the O_3 production. The European Union (EU) has established air quality standards for ambient ozone concentrations. Directive 2008/50 defines information and alert thresholds which refer to hourly values and equal to 180 and 240 mg m^{-3}. The same directive also defines a guideline for the protection of human health and the maximum daily average value of 8 hours should not exceed the target value of 120 mg m^{-3} on more than 25 days per the calendar year over a period of three years.

In Brazil, there is the CONAMA Resolution of July 28, 1990, which defines atmospheric pollution and establishes the pollution limits of any form of matter or energy with intensity and in quantity, concentration, time or characteristics in disagreement with the established levels, that renders the air inappropriate, harmful or offensive to health, inconvenience to the public welfare, damage to materials useful for fauna and flora, detrimental to safety, use and enjoyment of property, and normal community activities.[5]

Monitoring data and scientific studies on ambient air quality show that some of the air pollutants in several major cities were increasing over time and not always at acceptable levels according to WHO standard. There are very limited sampled data and few case studies focusing on air pollution in Brazil, while most air modelling cases using probability distribution have been applied in foreign countries. Although such application is almost non-existent in Brazil, it is an attractive analytical option since it can reasonably predict the return period and its concentration in the subsequent period to meet evolving information needed for environmental quality management.

The use of statistics is important in the analysis and interpretation of sample data in which the results can be used as forecasting tools that have become the main objective of environmental engineering.[6] Many types of

probability distributions have been used to adjust the concentrations of air pollutants which include Weibull distribution.[7] lognormal distribution,[8] range distribution,[9] Rayleigh distribution,[10] distribution of Gumbel[11] and distribution of Frechet.[12] From scientific findings, Lu [13] and Chen et al.[14] studied the fit for selected probability distributions using various performance indicators, such as the mean absolute error (MAE), root mean square error (RMSE), concordance index (d2), bias (B), absolute normalized error (NAE), prediction accuracy (BP) and determination coefficient (R^2). The objective of this study is to analyze and compare the Weibull distribution parameters in five cities with the results obtained for Campo Grande for modelling of the ozone concentration in MS, Brazil.

Experimental

Studied area and observational data

Campo Grande is the capital city of South Mato Grosso (MS) state, located in the south of Brazil Midwest region, and sited in the centre of the state. Geographically the considered city is near to the Brazilian border with Paraguay and Bolivia. It is located at 20°26'34'' South and 54°38'47'' West. Figure 1 shows the location of Campo Grande in the state of South Mato Grosso.

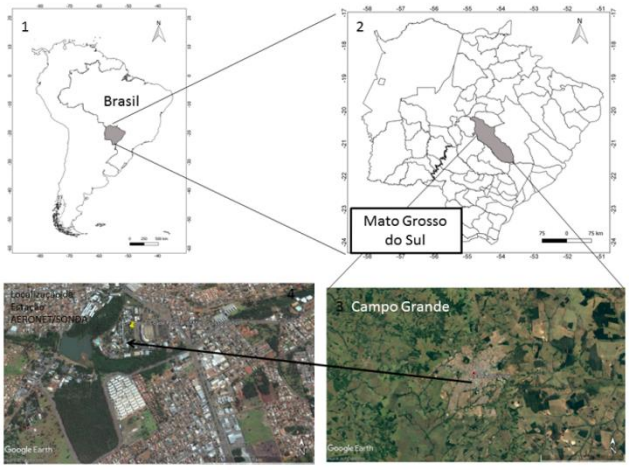

Figure 1. Location of the Municipality of Campo Grande in the State of South Mato Grosso, and the continuous air monitoring station.

The city occupies the total area of 8,096.051 km² or 3,126 mi², representing 2.26 % of the total state area, within 860,000 inhabitants (2016) and a corresponding HDI of 0.78. The urban area is approximately 154.45 km² or 60 mi², where tropical climate and dry seasons predominate, with two clearly defined seasons: warm and humid in summer, and less rainy and mild temperatures in winter. During the months of winter, the temperature can drop considerably, arriving on certain occasions to the thermal sensation of 0ºC or 32ºF with occasional light freezing.

The yearly average precipitation is estimated at 1,534 mm, with small up or down variations. The main pollution problems in the city are attributed to the traffic of vehicles, the rise of building activities, the presence of dumping grounds, the use of small power generators running on oil to supply electric grids power, and to the induced fire outbreak used to clean up local terrains.

The instruments used for the measurements are recorded in Table 1.

Meteorology

For the development of this work, we used electronic data from the continuous air monitoring station located on the campus of the Federal University of Mato Grosso do Sul, Campo Grande (MS), as shown in Figure 1.

Table 1. Instrumentation for measuring the atmospheric pollutants and meteorological parameters

Parameter	Ozone
Instrument model	Thermo Environmental 49C
Detector	Chemiluminescence
PA Equivalent Method	EQOA-0880-047
Error (±)	1 ppb

Probability Distributions

In order to model the sampled data sets for South Mato Grosso, Weibull probability distributions were used. Performance indicators are calculated by comparing the observed values with predicted values. The observed values are the classified values of the monitoring data, while the predicted values are the values obtained from the adjusted distribution of any statistical function.

Weibull distribution

The distribution function of Weibull two parameters for the concentration of ozone emission is expressed by the probability density function (eqn.1) where $f(v)$ is the probability of observed ozone concentration (v), k is the dimensionless Weibull parameter/factor and c is the Weibull scale parameter (m s^{-1}). The scale parameter can be related to the mean ozone concentration through the shape factor, which is the consistency of ozone concentration at a given location.

$$F(v) = \frac{df(v)}{dv} = \left(\frac{k}{c}\right)\left(\frac{v}{c}\right)^{k-1} exp\left[-\left(\frac{v}{c}\right)^{k}\right] \qquad (1)$$

The cumulative distribution $F(v)$ is an integral part of the probability density function and can be expressed eqn. (2).

$$F(v) = \int_{V} f(v)dv = 1 - e^{\left(\frac{v}{V}\right)^{k}} \qquad (2)$$

The entire distributions can be used to resolve the probability of occurrence affecting the shape of probability curve of the wind regime. The cumulative curve probability nature typically fits the Weibull distribution function.

Various methods for estimation of Weibull parameters as reported in the literature are furnished below.

Energy pattern factor method (EPFM)

The energy pattern factor is connected to the average data of ozone concentration and can be defined as the ratio of the mean of cubic ozone concentration to the cube of mean ozone concentration. The energy pattern factor (EPF) can be expressed as eqn. (3), where v_i is the wind speed in meter per second for i^{th} observation, N is the total number of ozone concentration observations, and $\bar{v}$ is the monthly mean wind speed.

$$EPF = \frac{1}{\bar{v}^3}\left(\sum_{i=1}^{n}\frac{{v_i}^3}{N}\right) = \frac{\Gamma\left(1+\frac{3}{k}\right)}{\Gamma^3\left(1+\frac{1}{k}\right)} \quad (3)$$

Once EPF is calculated, the Weibull shape and scale factors can be estimated from the following formulae.

$$k = 1 + \frac{3.69}{EPF^2} \quad (4)$$

$$c = \frac{\bar{v}}{\Gamma\left(1+\frac{1}{k}\right)} \quad (5)$$

Least-squares regression method (LSRM)

LSRM is well known as a graphical method implemented by plotting a graph in such a way that the cumulative Weibull distribution becomes a straight line where the time - series data must be sorted into bins. The equation of PDF,[15] after transformation and taking into consideration of natural logarithms on both sides, the expression can be written as eqn. (6)

$$ln\left[-ln\left(1-F(v)\right)\right] = k.ln(v) - k.ln(c) \quad (6)$$

Therefore, eqn. (6) is linear and can be fitted using the following least square regression method.

$$y = ax + b,\ y = ln\left[-ln\left(1-F(v)\right)\right],\ x = ln(v),$$
$$b = -k\ln(c), k = a;\ c = e^{-\frac{b}{k}} \quad (7)$$

The cumulative distribution function, $F(v)$ can be easily estimated from an estimator (eqn. 8), which is the median rank according to Benard's approximation, where i is the number of the wind speed measurements and N is the total number of observations.[16]

The relationship between $\ln(v)$ as a function of $\ln(-\ln(1-F(v)))$ represents a straight line with slope k, and the intersection point with Weibull line gives the value of scale parameter (c) derived from ozone concentration in part per billion (ppb).

$$F(v) = \frac{i-0.3}{N+0.4} \quad (8)$$

Method of moments (MOM)

MOM is one of the iterative techniques commonly used in the field of applied sciences for evaluating the Weibull parameters. It is based on the numerical iteration of mean ($\bar{v}$) and standard deviations (σ) of ozone concentration and expressed as follows.

$$\bar{v} = \frac{1}{n}\sum_{i=1}^{n}(v_i) \quad \text{and} \quad \sigma = c\left[\Gamma\left(1+\frac{2}{k}\right) - \Gamma^2\left(1+\frac{1}{k}\right)\right]^{\frac{1}{2}}$$

$$\frac{\sigma}{\bar{v}} = \sqrt{\frac{\Gamma\left(1+\frac{2}{k}\right)}{\left[\Gamma\left(1+\frac{1}{k}\right)\right]^2} - 1} \quad (9)$$

The dimensionless Weibull and scale parameters can be calculated by eqns. (10) and (11).

$$k = \left(\frac{0.9874}{\varphi/v}\right)^{1.0983} \quad (10)$$

$$\bar{v} = c\Gamma\left(1+\frac{1}{k}\right) \quad (11)$$

The average ozone concentration can be expressed as a function of Weibull scale parameter (c) and dimensionless Weibull shape parameter (k) derived from the Gamma function defined in eqn. (12), where $y = (v/c)^k \times e(v/c) = y^{x-1}\ and\ x = 1 + 1/k$. Therefore, the expression is reduced to eqn. (13).

$$\Gamma(x) = \int_0^\infty y^{x-1}\, e^{-y} dx \quad (12)$$

$$\bar{v} = c\Gamma\left(1+\frac{1}{k}\right) = 0.8525 + 0.0135k + e^{-(2+3(k-1))} \quad (13)$$

Mean standard deviation method (MSDM)

MSDM is used where only the two parameters such as the mean wind speed and standard deviations are available. It is well known as an empirical method and could be considered as a unique case of MOM method, in which the Weibull shape and scale parameters are estimated by eqns. (14) and (15), where σ is the standard deviation and $\bar{v}$ is the mean ozone concentration in ppb. Alternatively, Weibull scale parameter can be projected from the following expression given by eqn. (16).

$$k = \left(\frac{\sigma}{v}\right)^{1.086} \quad (14)$$

$$c = \frac{\bar{v}}{\Gamma\left(1+\frac{1}{k}\right)} \quad (15)$$

$$c = \frac{\bar{v}\, k^{2.6674}}{0.184+0.816k^{2.73855}} \quad (16)$$

Statistical Accuracy Analysis / Goodness of Fit

To find the best model method for analysis, several statistical tools have been used by researchers to analyze the efficiency of above-mentioned methods. The following tests are utilized as follows:

(a) Relative percentage error (RPE)

$$RPE\ (\%) = \left(\frac{x_{i,w} - y_{i,m}}{y_{i,m}}\right) \times\ 100 \qquad (17)$$

(b) Root mean square error (RMSE)

$$RMSE = \left[\frac{1}{N}\sum_{i=1}^{n}\left(x_{i,w} - y_{i,m}\right)^2\right]^{\frac{1}{2}} \qquad (18)$$

(c) Mean percentage error (MPE)

$$MPE = \frac{1}{N}\sum_{i=1}^{n}\left(\frac{x_{i,w} - y_{i,m}}{y_{i,m}}\right) * 100\% \qquad (19)$$

(d) Mean absolute percentage error (MAPE)

$$MAPE = \frac{1}{N}\sum_{i=1}^{n}\left|\frac{x_{i,w} - y_{i,m}}{y_{i,m}}\right| * 100\% \qquad (20)$$

(e) Chi square error

$$\chi^2 = \frac{\sum_{i=1}^{n}\left(x_{i,w} - y_{i,m}\right)^2}{y_{i,m}} \qquad (21)$$

(f) Kolmogorov – Smirnov test

$$Q_{95} = \frac{1.36}{\sqrt{N}} \qquad (22)$$

(g) Analysis of variance (or) Regression coefficient

$$R^2 = \frac{\sum_{i=1}^{N}\left(y_{i,m} - z_{i,\bar{v}}\right)^2 - \sum_{i=1}^{N}\left(y_{i,m} - x_{i,w}\right)^2}{\sum_{i=1}^{N}\left(y_{i,m} - z_{i,\bar{v}}\right)^2} \qquad (23)$$

where

N is the number of ozone concentration observations, $y_{i,m}$ is the frequency of observation of i^{th} calculated value from measured data,

x_{iw} is the frequency of i^{th} calculated value from the Weibull distribution and

$z_{i,v}$ is the mean of i^{th} calculated value from the measured dataset.

In general, *RPE* shows the percentage deviation between the calculated values from the Weibull distribution and the calculated values from measured data. Similarly, the *MPE* shows an average of percentage deviation between the calculated values of the Weibull distribution and the calculated values from measured data, and *MAPE* shows the absolute average of percentage deviation between the calculated values of the Weibull distribution and the calculated values from measured data. Perfect results are obtained when these values are nearest to zero. Regression coefficient (R^2) determines the linear relationship between the calculated values from the Weibull distribution and measured data. An ideal value of regression coefficient is equal to 1.

Coefficient of Variation (COV)

COV is defined as the ratio between the mean standard deviation to the mean ozone concentration expressed in terms of percentage. It demonstrates the uncertainty of ozone concentration and can be expressed as eqn. (24), where σ is the standard deviation and v is the mean wind speed (m s^{-1}).

$$COV(\%) = \frac{\sigma}{\bar{v}} \times 100 \qquad (24)$$

RESULTS AND DISCUSSION

The description of statistics of ozone concentration for the sampling period of 2015 is shown in Table 2. The mean value of the ozone concentration was higher than the median indicating that there was a high concentration recorded during the study period, the positive numbers indicate roughness effect that defines the occurrence of extreme events and the emissions of ozone gas.

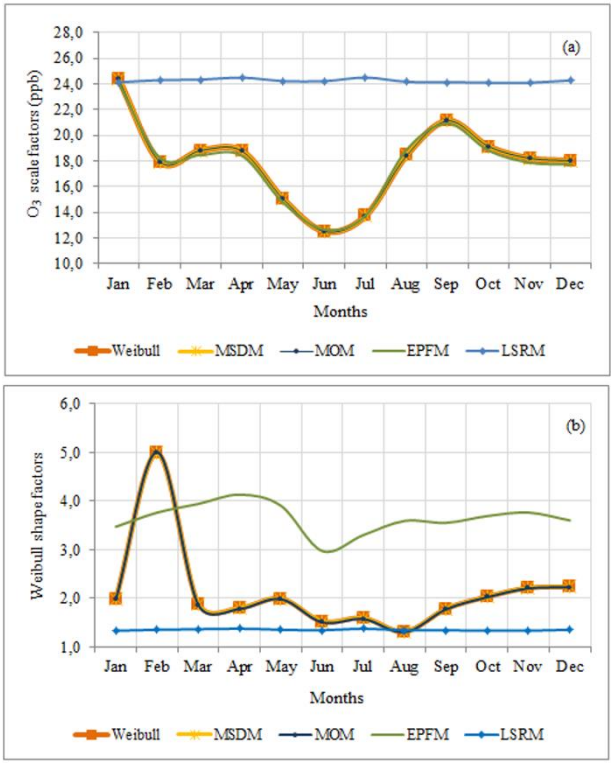

Figure 2. Weibull scale (a) and shape factors (b) designed by statistical approaches in Campo Grande.

Table 2. Descriptive analysis of ozone concentration for the sampling period (2015)

Months	Jan	Feb	Mar	Apr	May	Jun	Jul	Aug	Sep	Oct	Nov	Dec
Mean	21.60	16.46	16.75	16.70	13.23	11.28	12.41	17.01	18.88	16.94	16.11	15.97
StDev	11.45	9.09	9.36	9.73	7.06	7.69	8.04	13.20	11.06	8.83	7.75	7.61
$C_{variation}$	53.00	55.26	55.89	58.27	53.38	68.15	64.76	77.60	58.57	52.13	48.10	47.66
Median	18.90	15.25	15.80	15.50	13.20	10.20	12.10	15.55	17.60	15.80	15.20	14.75
Minimum	1.90	2.20	2.20	2.10	2.00	2.00	2.00	1.60	2.00	2.00	2.30	1.00
Maximum	79.7	70.9	58.5	61.2	41.3	34.5	44.4	55.9	57.7	47.7	46.6	36.4
Skewness	1.13	1.39	0.96	1.11	0.40	0.38	0.47	0.65	0.71	0.71	0.67	0.42
Kurtosis	2.11	4.98	1.49	1.95	0.11	-1.04	-0.32	-0.44	0.38	0.47	0.44	-0.54
Count	742	672	742	742	742	720	742	742	720	742	720	742
k	1.99	4.98	1.88	1.80	1.99	1.52	1.59	1.31	1.78	2.03	2.21	2.23
O_3 (ppb)	24.36	17.93	18.81	18.76	15.03	12.51	13.71	18.43	21.13	19.11	18.19	18.00

These results also show how ozone distributions were distorted to the right. Most of the sampled data was concentrated to the left of the PDF chart (Figure 3b) with few high values of ozone concentration (ppb). An average, a median, roughness and persuasion values have increased, indicating a growing problem of air pollution in Campo Grande.

Figure 2 shows the plots of monthly variations of the Weibull distributions generated by four statistical approaches considered for the Weibull shape and scale parameters. It can be seen that the divergence of the parameters of the form and the methods is more significant than the parameters of the scale. The dimensionless Weibull shape parameters observed less significant values obtained from EPFM and LSRM. Consistency is achieved in the Weibull scale parameters, and both MOM and MSDM have a comparable range of Weibull scale and shape parameters.

Table 2 lists the expressive ozone concentration statistics, which show evident variations for different time periods. The range of the ozone concentration can be represented as the discrepancy between the maximum and minimum ozone concentration. The concentration of ozone varies between 1 and 79.7 ppb with a mean value of 16.1 ppb. Likewise, standard deviations range from 13.2 to 7.06 ppb.

The critical values at 95 % confidence level in the Kolmogorov-Smirnov (Q95) test are 0.0248 and 0.0246 for months at 31 days and 30 days, respectively. In the end, the maximum error in the CDF never exceeds the corresponding significant values, which implies that the proposed technique is applicable to generate the necessary variables in the selection of the site.

Figure 3 shows the histogram and the comparison of the Weibull probability functions of the monthly average ozone concentration. The ozone data robustly characterized by the Weibull probability density function (PDF) and the cumulative distribution function (CDF). The maximum CDF errors are below or close to critical values in the Kolmogorov-Smirnov test at the 95 % confidence level. A similar behaviour was observed and the least squares regression method does not satisfy precisely all other methods.

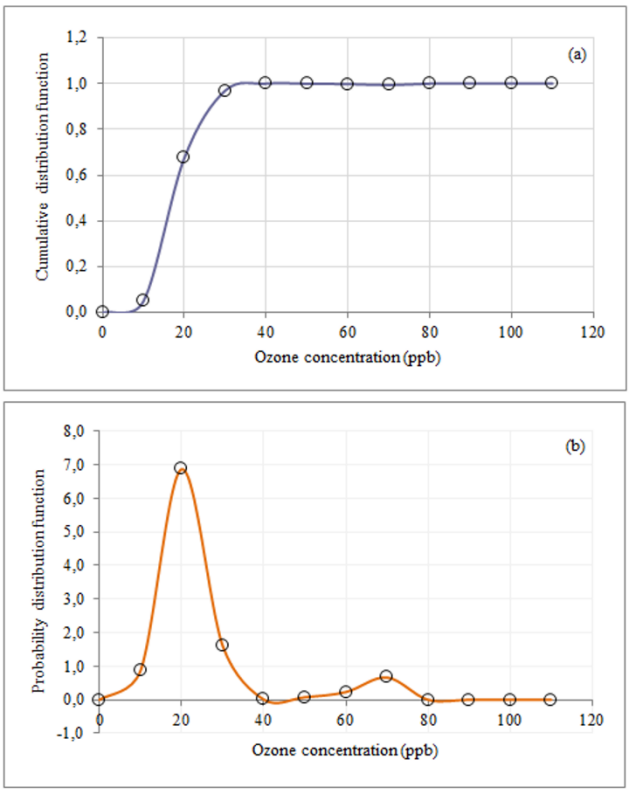

Figure 3. CDF (a) and PDF (b) plots for Weibull distribution obtained for 2015.

It is observed that for the Weibull distribution, the parameter of form *k* oscillated considerably in the comparison between the months, varying from 4.9815 to 1.3137, with the lowest value occurring in August and the highest value in the month of February, it is observed that the value of *k* is inversely related to the variance of the ozone concentration, which implies low variances if *k* is high and vice versa. In this sense, the values of *k* obtained for Campo Grande were in full agreement with the previous statement, where the highest values of *k* were related to the smallest variances shown in Table 2. The scale parameter *c* also varied within the range of 24.4 to 12.5 ppb, with minimum values, suggesting for this period a higher probability of occurrence of lower ozone concentration.

In order to compare the quality of the PDFs to sample variable concentration data, several statistics were used in related studies for O_3 analysis. The most used are the coefficient of determination, the results of the Chi-square test (χ^2), and the mean square error (RMSE). In most studies, a visual evaluation of the adjusted PDFs superimposed on the data histograms is also performed. The RMSE is applied in theoretical cumulative probabilities against empirical or theoretical cumulative probabilities of the concentrations of the observed variables. These statistics are also calculated with variable data in the form of frequency histograms.

In addition to the analysis performed on the variable distributions, some authors also evaluated the adequacy of PDFs to adjust the concentration distributions obtained by the sample variables or to predict the concentrations. In this case, the PDFs are first adjusted to the variables data. Then, the theoretical density distributions are derived from the PDFs adjusted for the variables. Finally, the fit quality measures are calculated using the theoretical density distributions and the distribution estimated from the O_3 variables of the sample.

The performance of these PDFs to evaluate the concentrations of the variables was also analyzed and the results are summarized in Table 2. It can be said that the evaluation of these distribution functions based on the quality of the adjustment criteria alone is not enough. These criteria should be used to identify appropriate distributions before a detailed analysis is done. Because these installed PDFs can be used for different applications by industries, public decision-makers, the performance of these PDFs for specific applications, such as the predicted concentration of pollutants, should also be evaluated. The results show that there are underestimation and overestimation of the concentration density of the pollutant in general, depending on the concentration range. The percentage errors show mainly that this underestimation and overestimation of the concentrations of these pollutants, which may be due to the effect of heating and the atmosphere.

The concentration of ozone increases slowly after sunrise, peaking during the day and then decreasing until the following morning. This is due to the photochemical formation of O_3. The shape and amplitude of ozone cycles are strongly influenced by climatic conditions (solar radiation) and by prevailing levels of precursors (NO_x).

For example, Hsieh and Liao[17] argued that the probability distributions for all air pollutants in Taiwan were approximate to be a lognormal distribution. Besides that, Neustadter et al[18] revealed that the total suspended particulate is obviously logically distributed, whereas sulfur dioxide and nitrogen dioxide are rationally estimated by lognormal distributions. However, Oguntunde et al[19] showed that the Gamma distribution is the best distribution for carbon monoxide concentration modelling in Lagos State, Nigeria. Kan and Chen[20] indicated that the best fit distributions for PM10 concentrations in Shanghai were lognormal.

In Malaysia, Noor et al[21] found that the best distribution fits of the PM10 observations in Nilai was the Gamma distribution while the log-normal distribution is more appropriate in Shah Alam. Razali et al[22] refer to the lognormal distribution as the best distribution corresponding to carbon monoxide data in Bangi, Malaysia. Consequently, there is no common distribution of air pollutants and it differs by region and time studied. It is important to conduct a comparative analysis to find out which distribution best fits the air pollutants at a specific location in order to provide a better estimate of the air quality at that location.

The four methods mentioned above were used to estimate the two Weibull parameters, i.e., shape and scale parameters. These values are averaged and presented in Figures 2a and 2b It can be clearly seen that a strong linear relationship between the monthly parameters of the Weibull average scale and the mean concentration measure of ozone. The values of the regression coefficients (R^2) are extremely high and show a counterpart to the linear model (R^2 = 0.999927). Figure 4 shows the linear relationship between the Weibull scale parameter and the monthly mean values observed in Campo Grande, the correlation between the monthly scale parameter, and the monthly average ozone concentration measured, a linear relationship was found with a directly proportional slope to the average of the monthly parameters of the scale *k*.

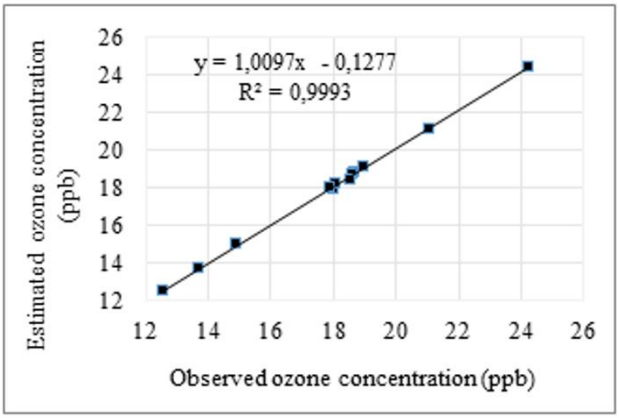

Figure 4. The relation between Weibull O_3 parameters monthly scaled (averages of all four methods) and the mean values of the average ozone concentration.

The ozone concentration can be demonstrated by the coefficient of variation. It can be defined as the ratio between the standard deviation of the ozone concentration and is an indicator and not an absolute value. The average monthly VOC values are shown in Table 2. The coefficient of variation varies from 77.60 to 47.65 % and the highest percentage variation in the month of August. In general, the VOC is lower when the concentration of ozone is maximum and vice versa.

To judge the relative efficiency of the statistical methods, six statistical tools, i.e., RPE, RMSE, MPE, MAPE, χ^2 and R^2 are employed. Many researchers have already used methods at different geographic locations to estimate ozone concentration. In general, only one column is needed to classify statistical methods, since the above approaches give virtually identical results. For a more accurate diagnosis, these six statistical tools were used to classify the methods.

From Table 5, it is clear that MSDM, MOM, and EPFM give very close results and perform better than LSRM. The most important criteria are chi-square error (ideally $\chi^2 = 0$) and regression coefficient (ideally $R^2 = 1$).

Table 5. Relative efficiency of statistical methods used.

Method	*K*	O_3 (ppb)	Bias	*MAE*	*MSE*	*RMSE*	χ^2	R^2
MSDM	2.1088	17.9975	0.0000	0.0000	0.0000	0.0000	0.0000	1.0000
MOM	2.0990	17.9897	0.0078	0.0078	0.0002	0.0000	0.0000	0.9990
EPFM	3.6383	17.8638	0.1338	0.1338	0.0902	0.3004	0.0049	0.9920
LSRM	1.3463	2.4239	-6.2416	6.2416	48.5026	6.9644	3.1889	0.2000

The average monthly variation of the amplitude observed in the ozone concentration (10.32 ppb) can be attributed to the fact that it is related to the winter solstice. At this time, the region under study suffers from the constant penetration of cold fronts coming from the South, these cold fronts alter the fields of atmospheric pressure and can directly influence the direction and speed of the wind. The north-east, northwest-northeast, north-west, north-east and north-northwest winds occur every month of the year. In these directions, the northwest direction is what predominates more in the region.

With the entry of cold front, there is a decrease in pressure, causing the wind to recede and increase its speed. During its passage, there is an increase in atmospheric pressure, causing sudden changes in the direction of the wind, which is usually accompanied by bursts. As with the front, the pressure rises slowly and continuously and can present bursts with subsequent stability.[23]

It is known that the climate of the region and the entire state is influenced by several factors, such as the infiltration of cold air masses, especially during the winter months, possibly the Atlantic Polar Mass. Another mechanism that has been changing the region's climate in recent years is the "El Niño" and "La Niña" phenomena.[24]

With respect to the Atlantic Polar Mass, with continental dislocation, it originates on the sub-Antarctic waters to the south of South America, penetrates in the state by West and Southwest and predominates in autumn and winter. It is dry and does not get moisture throughout the season. The Atlantic Polar Mass with maritime displacement also originates to the south of the South American continent, predominates during the winter and the spring. It is dry at the source and absorbs moisture from the ocean, mainly from the warm current of Brazil.[25]

These results prove the need to carry out regional studies by testing a greater number of probabilistic models for the adjustment of this climatic variable, since physical space peculiarities and the interference of climatic phenomena in the region, in monthly, daily and even hourly, are able to change the behavior of the ozone-climate variable significantly. As shown in Tables 3 and 4 discussed above, the Weibull distribution adequately adjusted the mean wind concentration data. This extremely important result could only be verified by the investigation of a probabilistic model less used in other studies and regions.

CONCLUSIONS

Parameter estimation is one of the important steps in assembling distribution, allowing predictions to be made accurately. The objective of this study was to compare several parameter estimators and to find the most appropriate estimator and distribution to predict ozone concentration. The quality and reliability of the models developed were evaluated through four performance indicators and the result of this study shows that the EPFM, MOM and MSDM is the most appropriate method to estimate the parameter for Campo Grande using the Weibull distribution.

From the analysis of the test results, it was evidently revealed that LSRM presented worse performance than other methods. The EPFM, MOM and MSDM methods are the most efficient methods to adjust the Weibull distribution curves for the evaluation of ozone concentration data.

The study revealed that the air quality status was not good at all times. Four distributions were compared and the Weibull distribution offers the best fit because three performance indicators offer the best results for this distribution. The scatter plot of observed O_3 concentrations versus predicted values obtained from the Weibull distribution shows a very good fit with the coefficient of determination of 0.999.

REFERENCES

[1]Carslaw, D. C., Evidence of an increasing NO2/NOX emissions ratio from road traffic emissions, *Atmos. Environ*., **2005**, *39(26)*, 4793-4802. DOI: https://doi.org/10.1016/j.atmosenv.2005.06.023

[2]Souza, A., Aristone, F., Kumar, U., Kovač-Andrić, Arsić, M., Ikefuti, Sabbah, I., Analysis of the correlations between NO, NO2 and O3 concentrations in Campo Grande – MS, Brazil, *Eur. Chem. Bull*., **2017**, *6*(7), 284-291. DOI: http://dx.doi.org/10.17628/ecb.2017.6.284-291

[3]Souza, A., Fernandes, W. A., Surface ozone measurements and meteorological influences in the urban atmosphere of Campo Grande, Mato Grosso do Sul State, *Acta Sci. Technol*., **2014**, *36(1)*, 141-146. DOI: 10.4025/actascitechnol.v36i1.18379

[4]Pires, J. C. M., Souza, A., Pavão, H.G., Martins, F. G., Variation of surface ozone in Campo Grande, Brazil: meteorological effect analysis and prediction, *Environ. Sci. Pollut. Res. Int*., **2014**, *21(17)*, 10550-10559. DOI: 10.1007/s11356-014-2977-6

[5]BRASIL Ministério do Meio Ambiente. Resolução CONAMA 3/1990, Brasília, **1990**.

[6]Hoshmand, A. R., *Statistical Method for Environmental and Agricultural Sciences.* CRC Press LLC, Florida, **1998**.

[7]Wang, X., *Atmos Environ*., **2004**, *38(74)*, 4383-4402. Characterizing distributions of surface ozone and its impact on grain production in China, Japan and South Korea: 1990 and 2020. DOI: https://doi.org/10.1016/j.atmosenv.2004.03.067

[8]Hadley, A., Toumi R., *Atmos Environ*., **2003**, *37(11)*, 1461-1474. Assessing changes to the probability distribution of sulphur dioxide in the UK using a lognormal model, DOI: https://doi.org/10.1016/S1352-2310(02)01003-8.

[9]Singh, P., Simultaneous confidence intervals for the successive ratios of scale parameters, *J. Stat. Plan. Infer.*, **2006**, *136(3)*, 1007-1019. DOI: https://doi.org/10.1016/j.jspi.2004.08.006

[10]Celik, A. N., A statistical analysis of wind power density based on the Weibull and Rayleigh models at the southern region of Turkey, *Renew. Energ*., **2004**, *29(4)*, 593-604. DOI: https://doi.org/10.1016/j.renene.2003.07.002

[11]Phien, H. N., A computer assisted learning package for flood frequency analysis with the Gumbel distribution, *Adv. Eng. Softw*., **1989**, *11(4)*, 206-212. DOI: https://doi.org/10.1016/0141-1195(89)90051-X

[12]Caleyo, F., Velázquez, J. C., Valor, A., Hallen, J. M., Probability distribution of pitting corrosion depth and rate in underground pipelines: A Monte Carlo study, *Corros. Sci*., **2009**, *51(9)*, 1925-1934. DOI: https://doi.org/10.1016/j.corsci.2009.05.019

[13]Lu, H. C., Estimating the emission source reduction of PM10 in central Taiwan, *Chemosphere*, **2004**, *54(7)*, 805-814. DOI: https://doi.org/10.1016/j.chemosphere.2003.10.012

[14]Chen, J. L., Islam, S., Biswas, P., Nonlinear dynamics of hourly ozone concentrations: nonparametric short term prediction, *Atmos. Environ*., **1998**, *32(11)*, 1839-1848. DOI: https://doi.org/10.1016/S1352-2310(97)00399-3

[15]Johnson, N. L., Kotz, S., *Continuous Univariate Distributions*, v. 2, 2nd Edition, Houghton Mifflin, **1970**.

[16]Benard, A., Bos-Levenbach, E. C., Het uitzetten van waarnemingen op waarschijnlijkheids, *Stat. Neederl*., **1953**, *7(3)*, 163–173. DOI: https://doi.org/10.1111/j.1467-9574.1953.tb00821.x

[17]Hsieh,N. H,. Liao, C. M., Fluctuations in air pollution give risk warning signals of asthma hospitalization, *Atmos. Environ.*, **2013**, *75*, 206-216. DOI: https://doi.org/10.1016/j.atmosenv.2013.04.043

[18]Neustadter, H. E., Sidik, S. M., On Evaluating Compliance With Air Pollution Levels "Not To Be Exceeded More Than Once A Year", *J. Air Poll. Control Assoc.*, **1974**, *24(6)*, 559-563. DOI: 10.1080/00022470.1974.10469940

[19]Oguntunde, P. E., Odetunmibi, O. A., Adejumo, A. O., A Study of Probability Models in Monitoring Environmental Pollution in Nigeria, *J. Probab. Stat*., **2014**, Article ID 864965, *2014*, 6. DOI: http://dx.doi.org/10.1155/2014/864965

[20]Kan, H. D., Chen, B. H., A case-crossover and time-series study of ambient air pollution and daily mortality in Shanghai, China, *Epidemiology*, **2004,** *15(4)*, S55.

[21]Noor, N. M., Tan, C.-Y., Ramli, N. A., Yahaya, A. S., Yusof, N. F. F. M., Assessment of various probability distributions to model Pm 10 concentration for industrialized area in peninsula Malaysia: A case study in Shah Alam and Nilai, *Aust. J. Basic and Appl. Sci*, **2011**, *5(12)*, 2796-2811. https://doi.org/10.1063/1.4966829

[22]Razali, A. M., Desvina, A. P., Sapuan, M. S., Zaharim, A., Distributional fit of carbon monoxide data, *Adv. Environ. Comput. Chem. Biosci.*, Wseas LLC, 147-152, **2012**.

[23]Ayoade, J. O., *Introdução à climatologia para os trópicos*, 12th Edition, Bertrand Brasil, **2007**.

[24]Cruz, G. C. F., *Alguns aspectos do clima nos Campos Gerais*. In: Melo, M. S., Moro, R. S., Guimarães, G. B., (orgs.). *Patrimônio Natural dos Campos Gerais do Paraná*. UEPG, 59-72, **2007**.

[25]Wons, I., *Geografia do Paraná com fundamentos de Geografia geral*. 4th Edition, Ensino Renovado, **1982**.

Received: 10.04.2018.
Accepted: 28.05.2018.

POTENTIAL ENVIRONMENTAL IMPACT OF NANOENERGETICS

Nancy N. Perreault[a]*

Keywords: Nanomaterial, nanothermite, environmental fate, nanotoxicity.

Nanoenergetics has the potential to become the next generation of explosives and propellants. Nano-explosives often show better performances in terms of energy release, ignition and mechanical properties compared to their bulk counterparts. In addition to monomolecular explosives such as nano-TNT and nano-RDX, diverse energetic nanocomposites have been developed, including the nanometer-sized versions of conventional thermites (nanothermites) and those using carbon-based nanomaterials (e.g., fullerenes and carbon nanotubes). While the unique characteristics of nanomaterials allow groundbreaking applications, they also result in distinct environmental fate, transport and toxicity. The high surface to volume ratio and reactivity of nanomaterials make them highly dynamic in environmental systems. Once released in the environment, nanoenergetic chemicals will undergo transportation and transformation processes including dissolution, aggregation, adsorption, photolysis and biotransformation, which will also affect their persistence and bioavailability. This review was conducted to better understand the potential environmental fate and ecological impact of the use of nanoenergetics.

* Corresponding Authors
Fax: 514-496-6265
E-Mail: Nancy.perreault@cnrc-nrc.gc.ca
[a] National Research Council Canada, 6100 Royalmount Ave., Montréal, Québec H4P 2R2

Introduction

Over the past decades, remarkable progress has been made in military science and technology to design energetic materials with higher burning rate, density and reactivity, lower sensitivity and smaller critical diameter. While explosives of coarse size are reaching their capacity limit, the emergence of nanotechnology brings new possibilities to meet the increasing military demands for high performance, safety, and environmentally friendly munitions. Nanomaterials, which are made of components with at least one dimension below 100 nm, have attractive characteristics allowing to decrease the sensitivity of explosives to impact, friction and shock waves and to increase energy release and burning rate. Increase in burning rate due to the addition of nanoenergetics to propellants is due primarily to the i) increased reactivity of nanomaterials compared to bulk materials (micrometer-sized particles), ii) increased rate of diffusion of the reactants, and iii) increased rate of energy release due to the much shorter combustion time of nanoparticles.[1] Nanoenergetics has the potential to become the next generation of explosives and propellants.

Many high explosives have been synthesized at the nanometer size including nano-nitramines (RDX, HMX, CL-20), nano-TATB (2,4,6-triamino-1,3,5-trinitrobenzene), nano-NTO (5-nitro-2,4-dihydro-3H-1,2,4-triazole-3-one) and nano-TNT (2,4,6-trinitrotoluene). Compared to their micron-sized counterparts, the shock sensitivities of nano-nitramine explosives were shown to be decreased by 59.9% (RDX), 56.4% (HMX) and 58.1% (CL-20).[2]

Nanothermites, mixtures of a metal (e.g. Al) and metal oxide (e.g. Fe_2O_3) at the nanoscale, are much more reactive than traditional thermites. Nanothermites are the most intensively investigated nanoenergetics and the only one currently in use by the military. Nano-aluminum is the most common component of metal-based nanomaterials and considered as a potential replacement for the conventional aluminum powders and flakes widely used in explosives and propellants.

Carbon-based nanomaterials, including single- or multi-walled nanotubes and fullerene C_{60}, have become important due to their unique combinations of chemical and physical properties (e.g. thermal and electrical conductivity, high mechanical strength) and are used for many industrial applications. Carbon-based nanomaterials can be functionalized with energetic groups or filled with high energetic molecules, mixed with nanothermites or doped with metal oxide catalysts for use as nanoenergetics. Carbon nanotubes (CNTs) are long, thin, hollow cylinders, composed of one (single-walled carbon nanotubes, SWCNTs) or many (multi-walled carbon nanotubes, MWCNTs) concentric layers of graphenic carbon. Fullerene C_{60} has a cage-like fused-ring structure (truncated icosahedron) that resembles a soccer ball, comprising 60 carbon atoms. The use of functionalized carbon nanomaterials in energetic compositions greatly improves their combustion performances, thermal stability and sensitivity. Choi et al.[3] obtained a burning rate exceeding more than 103 times the value of bulk RDX when using 7-nm RDX annular shell around a MWCNT. When energetic materials 4-nitrobenzenediazonium nitrate, 4-nitroaniline, 2,4-dinitroaniline and RDX were loaded on CNTs, the exothermic reaction speeds of all energetic materials increased by approximately 100 times compared with those of the energetic materials alone.[4] CNT-supported metal oxide nanoparticles significantly enhanced thermal decomposition of nitrocellulose-absorbed nitroglycerin, RDX, ammonium perchlorate and N-guanylurea-dinitramide (FOX-12). Moreover, the encapsulation of FOX-7 (1,1-diamino-2,2-dinitroethylene), RDX and HMX inside a CNT was shown to stabilize these energetic chemicals, thereby reducing their sensitivity.[5] Because of heat energy coming from the high density of covalent energy stored by the carbon-carbon bonds in the C_{60}, fullerenes are of interest for use in nanoscale explosives. A study showed that fullerene C_{60} can enhance the burning rate of double-based

propellants, broaden the plateau region and lower the concentration of NO_x in gas products.[6] Fullerenes C_{60} were also shown to reduce the friction and impact sensitivities of HMX.[7]

Environmental Fate

Nanoenergetics will enter the environment either in the pristine state from spills during manufacture, transport and storage of munitions, or will be disseminated in their post-combustion (or post-detonation) state. Poda et al.[8] found that residues of Al/Fe_2O_3-based nanothermite comprise particles, generally larger than 75 μm, consist of a mixture of FeO, Al_2O_3 and $FeAl_2O_4$. In the same study, Al/Bi_2O_3 formulations fully transformed to small (< 5 μm) particles consisting of metallic Bi and Al_2O_3. These products are largely resistant to wetting, settle quickly, and evidence suggests that transport in aqueous environments would be limited. Due to the particle size ranges found, it has been speculated that aerosolization should be a major transport route for the nanothermite residues. The high surface to volume ratio and reactivity of nanomaterials make them highly dynamic in environmental systems and energetic nanomaterials are likely to undergo transportation and transformation processes including dissolution, aggregation, adsorption, photolysis and biotransformation.

Transport

Solubility and dissolution

Transport is positively correlated with solubility. Theoretically, the solubility of a particle increases as size decreases. Furthermore, the rate of dissolution is dependent on particle surface area. Nanoparticles should thus dissolve faster than larger particles. The dissolution behaviour of metallic nanoparticles will affect their overall stability in the aquatic environment and their potential ecotoxicity, since toxicity has often been attributed to the release of ionic species rather than being induced by the nanoparticles themselves.[9] Most metal-based nanoparticles have very low solubility, however, their solubility is significant (e.g. in the mg L^{-1} range) from an environmental and toxicological perspective. For example, zinc oxide is classified as insoluble in water with a solubility of ~1 mg L^{-1} at pH 8; nevertheless, one gram of ZnO nanoparticles added to one litre of water at pH 7.8 will generate ~10 mg L^{-1} of dissolved Zn. While only representing dissolution of less than 2 % of ZnO, the Zn is well in excess of the 5 mg L^{-1} that would be toxic to most aquatic biota.

Pristine C_{60} fullerene and CNTs are insoluble in water. Solubility of C_{60} fullerene was estimated to be as low as 10^{-8} ng L^{-1} at 25 °C, equivalent to ten C_{60} molecules per ml of water.[10] Direct solubility is however not the most relevant measure of the availability of fullerenes to organisms, particularly to aquatic organisms. Indeed, although C_{60} is not soluble in water or other polar solvents, water-soluble colloidal aggregates (nano-C_{60} or nC_{60}) readily form when pristine C_{60} is added to water. The aggregates have reported diameters of 5 to 500 nm and allow for C_{60} concentrations up to 100 mg L^{-1}, eleven orders of magnitude more than the estimated solubility.[11] Recent developments in chemical modification and functionalization of CNTs have greatly improved the solubility and dispersion of CNTs in water. The solubility of monomolecular nano-explosives such as RDX and TNT has not been reported yet.

Aggregation and adsorption

Environmental fate and transport of nanoparticles can be significantly impacted by aggregation in water and adsorption onto the soil matrix and other particles. Because of their high surface area, nanoparticles have a tendency to sorb to sediments and soil particles, which greatly reduce their transport and bioavailability. Although assumption is often made than nanoparticles will be more mobile in porous media due to their small size, they may in fact be less mobile in porous media such as groundwater aquifer if they readily sorb to mineral surfaces. Thus, all other factors being equal (ionic strength and composition, media grain size and hydrodynamics), smaller particles should be less mobile due to their relatively large diffusivity that produces more frequent contacts with the surfaces of the porous media.[12] On the other hand, dissolved organic matter ubiquitous in aquatic ecosystems also adsorbs onto nanoparticles and this should favour their transport in aquatic environments.

Particles up to a few microns in size, that are present as individual particles, do not readily settle from solution. However, nanoparticles have the propensity to form larger micron-sized water-stable aggregates. Aggregation of nanoparticles typically leads to sedimentation and thus, to their removal from the aqueous phase and their immobilization. Aggregates of nanoparticles that settle can be expected to accumulate in sediments of lakes or rivers in the absence of nanoparticle degradation. Aggregation was shown to increase as the ionic strength of a solution increases and as the concentration of divalent cations such as Ca^{2+} and Mg^{2+} increases. Nanoparticles will thus tend to aggregate more in seawater (high ionic strength) than in freshwater. A study tested the stability of three metal oxide nanoparticles (TiO_2, ZnO and CeO_2) in aqueous samples.[13] In the low organic matter concentration and high ionic strength of seawater, the rate of sedimentation of the three nanoparticles was very high. At high nanoparticle concentrations, the concentration of suspended particles decreased by more than 80 % in less than 100 min; the rate decreased as nanoparticle aggregates were removed from solution, lowering the concentration of suspended particles. Metal oxide nanoparticles entering seawater are thus expected to be removed from the water column in a few hours. This suggests that marine organisms in the water column may only be significantly affected if the loading is frequent or continuous; benthic organisms may be at higher risk of exposure, although the exposure would be in the form of relatively large aggregates (> 1 μm) of nanoparticles.

A completely different behaviour occurred when the metal oxide nanoparticles were dispersed in freshwater, with high organic matter concentration and low ionic strength.[13] In freshwater, the size of the aggregates remained stable at slightly above 300 nm for the three metal oxides, with a very low rate of sedimentation. The significant amount of organic molecules that can be adsorbed onto the nanoparticle surfaces provided an additional barrier to aggregation. In the presence of NOM at realistic concentrations (1–30 mg of carbon L^{-1}), nanoparticles are

stabilized and aggregation is limited.[14,15] Thus, under these conditions, aquatic organisms within the water column (e.g. fish, algae, filter-feeders) will be exposed to small nanoparticle aggregates for a longer time. Eventually, within a few days the particles will sediment out, exposing benthic organisms as well. Chekli et al.[16] evaluated that 20 % of dissolved organic matter was adsorbed to nanoparticles of Fe_2O_3 in river and lake waters; adsorption was lower in groundwater (10 %) and seawater (5 %). As expected, the size of Fe_2O_3 aggregates was higher in ground- and seawater than in river and lake waters.

Nanoparticle mobility will be significantly reduced in terrestrial compared to aquatic systems. Adsorption of nanoparticles by soil minerals and soil organic matter has not been evaluated, but is likely to be a function of particle size, shape and surface properties (specific surface area and surface charge). Most soil particles have a negative charge: small hydrophilic nanoparticles (< 20 nm) with net negative surface charges are likely to be mobile, while large hydrophilic positively-charged particles are likely to be sorbed by soil. Strongly hydrophobic nanoparticles should be strongly retained by soil organic matter.[17] In addition, aggregation in soil leads to entrapment of particles in pores through which the dispersed nanoparticles could have passed, thus restricting mobility.

Transformation

Abiotic transformation

Redox reactions can alter the surface chemistry of nanoparticles and therefore affect their mobility, toxicity and ultimate fate in the environment. Despite the limited studies of redox transformations, most metal and metal oxide nanoparticles are expected to weather slowly overtime, similar to chemical weathering of minerals in the environment. Studies on the photochemical transformation of nanoparticles compared to their bulk counterparts are not available in the literature. Photochemical transformation may be an important fate process of fullerene C_{60} in surface waters due to its strong absorption within the solar spectrum. When exposed to light, the cluster size of nC_{60} was shown to decrease as the irradiation time increased.[18] Water-soluble products were formed and, with continued light exposure, these intermediates eventually mineralized, volatilized, or converted to other products. The decay rate of C_{60} in small clusters (150-nm diameter) was greater than for C_{60} in larger clusters (500 nm), with half-lives of 19 and 41 h, respectively. This suggests that release of C_{60} into surface waters will result in photochemical production of currently unknown products. Unfunctionalized SWCNTs are not, or only slowly, photo-transformed under sunlight, however, they can undergo indirect phototransformation through reactions with hydroxyl radicals.[19] A carboxylated SWCNT solution was also shown to produce ROS when exposed to sunlight or when irradiated in a solar simulator, which in turn oxidized CNTs and modified their surface.[20]

Biotransformation

Unlike organic pollutants, metals and metal oxides cannot be degraded. Therefore, biodegradation processes do not apply to nanothermite constituents. Biodegradation studies of nano-explosives are nonexistent in the literature and very few studies are available on the biotransformation of nanoparticles in general. Nano-sized explosives have a larger surface area compared to their micron-sized counterparts and this could possibly allow faster degradation by microorganisms.

A very limited number of microorganisms and enzymes have been found to transform or degrade nanomaterials. The physical and chemical nature of CNTs, fullerenes and their derivatives make them inert, stable and difficult to degrade. Nevertheless, some fungi and fungal enzymes were successful at transforming carbon-based nanomaterials. Lignin peroxidase (LiP) secreted by the mushroom *Sparassis latifolia* degraded carboxylated SWCNTs.[21] In addition, manganese peroxidase (MnP) from the white rot fungus *Phanerochaete chrysosporium* was reported to decompose SWCNTs.[22] Another white rot fungus, *Trametes versicolor*, showed a weak ability to degrade SWCNTs.[23] *Phlebia tremellosa* and *T. versicolor* mineralized fullerol, a water-soluble hydroxylated derivative of fullerene C_{60}, after 32 weeks of decay.[24] C_{60} itself was shown to be resistant to mineralization in sandy loam soil for at least 11 months and in silt loam for at least 2 years.[25] In addition, three bacteria (*Burkholderia kururiensis*, *Delftia acidovorans* and *Stenotrophomonas maltophilia*) were reported to form a consortium that degrade MWCNTs to CO_2 with several intermediate products such as 2-methoxynaphthalene, 2-naphthol, cinnamaldehyde and isophthalic acid.[26] Although individual bacteria in this community could weakly degrade MWCNTs, they were much more efficient degraders in combination. Chouhan et al.[27] isolated bacteria from a soil contaminated with nanomaterials and showed that the bacteria were adaptive and tolerant to the nanomaterials and thus could well survive in the contaminated soil. The bacteria were also able to transform MWCNTs by an oxidation process. The persistence of nanoenergetics in the environment will highly depend on their ability to be biodegraded. However, CNTs and fullerenes are not readily biodegradable and their fate upon release in the environment may end up being similar to polychlorinated biphenyls and other types of persistent organic pollutants (POPs), which also tend to be associated with particles in the environment.[12]

Potential ecotoxicity of nanomaterials and nanoenergetics

The fundamental properties of matter change at the nanoscale, therefore toxicity of nanoparticles cannot be predicted from the known properties of larger-sized particles of the same substance. The majority of studies have arrived at a similar conclusion: smaller particles induce a higher degree of cell death. For example, studies clearly indicated that tissue distribution of Al_2O_3 was size-dependent, and that metal oxide nanoparticles (Al_2O_3, Fe_2O_3) were able to cause more size- and dose-dependent toxicity in vivo compared to bulk materials.[28,29] Other factors influencing toxicity include shape, chemical composition, surface structure, surface charge, aggregation and solubility. As yet, little work has been conducted to determine the effects of nanoparticles to the biota in aquatic and terrestrial habitats. The current understanding of the toxicity mechanisms and impacts of nanomaterials to different ecosystems and trophic levels,

including bacteria, algae, crustaceans, fish, plants and soil invertebrates are summarized.

Mechanisms of nanotoxicity

Living organisms may be exposed to nanoparticles via several routes, including inhalation of airborne particles (respiratory tract), ingestion (gastrointestinal tract) and dermal contact (skin). Because of their small size, nanoparticles are often more readily taken up than larger particles. Nanoparticles can cross biological membranes and access cells, tissues and organs than larger-sized particles normally cannot. Inhalation of nanoparticles may become the major route for unwanted exposure to nanothermites and nano-explosives residues. Studies over the last 25 years have suggested that smaller particles made of low-toxicity, low-solubility materials are more potent at inducing lung inflammation than the same materials at larger particle sizes. Furthermore, smaller particles exhibit enhanced penetration across the lung epithelium and into the interstitium of the lung tissue. On the other hand, nanoparticles naturally tend to aggregate into larger particles that can be microns in size, thereby reducing the likelihood of free nanoparticles being respired. However, surface modifications designed to limit particle-particle interactions may reduce the tendency for nanoparticle aggregation and increase the potential for inhalation and deposition within the lungs. Inhaled particles of different sizes exhibit different fractional depositions within the human respiratory tract. Although inhaled ultrafine particles (< 100 nm) deposit in all regions, tracheobronchial deposition is highest for particles < 10 nm in size, whereas alveolar deposition is highest for particles approximately 10–20 nm in size.[30,31] Fullerenes, CNTs, metal and metal oxide nanoparticles were all shown to induce pulmonary inflammation and fibrosis in in vivo and in vitro studies. Once nanomaterials reach the blood stream, they are transported around the body and taken up by the organs and tissues. CNTs, for example, have been found to rapidly enter and disseminate in the organism, initially accumulating in lungs and brain and later reaching the liver and kidney via the bloodstream.[32] Many nanoparticles are capable of crossing the blood–brain barrier, potentially damaging the central nervous system and inducing neurotoxic effects.[33]

Reactive oxygen species (ROS) and free radical production has been identified as a primary mechanism of nanoparticle toxicity. Nanomaterial-induced ROS may result in oxidative stress, inflammation, and consequent damage to cellular constituents.[34] ROS can damage cell membrane, particularly through lipid peroxidation, as well as mitochondria, proteins and DNA, leading to cytotoxicity, genotoxicity and cancer. Another problematic phenomenon is the adsorption of proteins on nanoparticle surface that leads to the formation of nanoparticle-protein complexes commonly referred to as the nanoparticle-protein corona. Nanoparticles induce changes in the structure of adsorbed proteins and therefore impair their function. SWCNTs was shown to induce loss of structure and catalytic activity of enzymes.[35] Strong protein binding onto metal oxides is well documented, so adsorption unto metal oxide nanoparticles is likely. Nanoparticles can also induce conformational changes in proteins that can lead to fibril formation. Linse et al.[36] showed that a range of nanoparticles, including CNTs, are capable of inducing fibrillation of β2-microglobulin due to increased protein localization on the nanoparticle surface. Fibrillation of proteins is associated with diseases such as Parkinson's and Alzheimer's.

Dissolution is an essential factor to consider when evaluating toxicity of metal-containing nanoparticles. Toxicity of metal-based nanoparticles, such as ZnO, CuO and Ag, partly results from the release of metal ions.[9] Table 1 presents toxicity values[37] for some organism groups. In most cases, the free metal ions are significantly more toxic. Yet, the issue is relatively complex as also other nano-specific factors may complement the effect of dissolved metal ions and the distinct role of each factor remains unknown for the moment.[38]

As mentioned earlier, although fullerenes are highly insoluble in water, they are modified during mixing in water to form stable aggregates, known as nC_{60}, enabling C_{60} concentrations up to 100 mg L^{-1}. This ability to be dispersed in water increases their mobility in aquatic environments and makes them available to aquatic organisms.

Table 1. Toxicity of Ag, ZnO and CuO nanoparticles (NPs) and their respective ions to bacteria, yeasts, algae, crustaceans and fish. Adapted from Ivask et al.[38]

	MIC[a]	L(E)C$_{50}$[b]			
	Bacteria	**Yeasts**	**Algae**	**Crustaceans**	**Fish**
Ag NPs	7.1	7.9	0.36	0.01	1.36
Ag^+ ions	3.3	2.2	0.0076	0.00085	0.058
Zn NPs	500	121	0.08	2.3	3.0
Zn^{2+}	30	78	0.09	1.3	7.5
Cu NPs	200	17	2.8	2.1	100
Cu^{2+}	32	11	0.07	0.024	0.28

Values selected and summarized from Bondarenko et al.[37] [a] Minimal inhibitory concentration (mg L^{-1}); [b] Half-lethal or half-effective concentration (mg L^{-1})

Aquatic ecotoxicity

Nanomaterials can enter natural water systems by numerous direct (through aerial deposition, effluents, dumping and run-off) and indirect routes (e.g. via river systems). Most of the currently available ecotoxicological data regarding nanoparticles are limited to species used in regulatory testing or freshwater species, and there are discrepancies in the reported effects of nanoparticles on aquatic organisms. One of the key problems encountered when assessing aquatic ecotoxicology is the protocol used to prepare the nanoparticles. For CNTs and fullerenes, there is a general consensus that they have poor aqueous solubility and that some combination of chemical dispersants, stirring or sonication is necessary to maintain them in aqueous solution. A number of ecotoxicology studies have used the organic solvent tetrahydrofuran (THF) to disaggregate nanoparticles such as C_{60} prior to treatment of organisms. It was demonstrated that even after filtration and evaporation, THF remains trapped between the aggregated C_{60} particles,[39] suggesting that studies using THF investigated the effects of C_{60} combined with THF rather than the effects of C_{60} per se. THF is classified by many regulatory bodies as a neurotoxin, and so could in part explain some of the effects observed in the fish. For these reasons, it is worth considering some ecotoxicological studies with caution.

Uptake and toxicity from primary producers (algae), microscopic invertebrates, up through the trophic chain is probable. Sorption onto aquatic organisms has been reported as a dominant toxicity mechanism of nanoparticles as it affects the molting behavior and swimming speed of daphnids,[40] and alter filtering efficiency. Nanoparticle coating of gills can affect respiration, cause hypoxia in blood and spleen and reduce the locomotion of fish. Nanoparticles were also shown to cover algal cell surface, increasing the cellular weight by more than 2 fold, affecting the algae's ability to float, and reducing sunlight availability for photosynthesis.[41]

Effects on freshwater organisms

The early studies on freshwater invertebrates focused on crustaceans, with *Daphnia magna* being the most studied test species. It has been shown that daphnids take up significant amounts of both fullerene C_{60} aggregates (nC_{60}) and nano-iron from aqueous media.[42] Tissue levels of > 2 mg L^{-1} were reached when daphnids were exposed for 72 h to 30 mg L^{-1} of nC_{60} stirred in water. nC_{60} could not be prepared at high enough concentration levels to cause 50 % mortality (LC_{50}) at 48 or 96 h, and no mortality was observed before 5 to 6 days of exposure. Mortality was observed at concentrations of 1, 2.5, and 5 mg L^{-1}, with the highest mortality (40 %) achieved at 2.5 mg L^{-1}. Exposure for 21 days to 2.5 and 5 mg L^{-1} fullerenes resulted in a significant delay in *D. magna* molting and significantly reduced offspring production, which could have negative impacts at the population level. The ingested C_{60} did not visibly bind to the daphnid exoskeleton and antennae.

Exposure of *D. magna* to nano-iron only resulted in significant mortality at 62.5 mg L^{-1} (50 % level achieved in 24 h), which is considered a very large dose in environmental toxicology term. In addition, these organisms exhibited significant binding of the nano-iron particles to their exoskeleton surface and antennae as well as significant ingestion of the particles.

Exposure of up to 500 µg nano-Ag L^{-1} for 48 h did not cause mortality in *D. magna*;[43] in contrast, the crustacean was extremely sensitive to free Ag ion (Ag^+ added as $AgNO_3$), with a measured 48 h 50 % lethal concentration of 2.51 µg L^{-1}, suggesting that the acute toxicity of Ag nanoparticles was caused by the release of Ag^+ into solution. TiO_2 nanoparticles were shown to transfer through food chain from *Daphnia* to zebrafish.[44] Overall, toxicity studies on *D. magna* indicate that the lethality of the nanoparticles tested is relatively low, but that there may still be cause for concern.

C_{60} fullerene prepared with THF has been reported to cause significant oxidative damage *in vivo* in largemouth bass (*Micropterus salmoides*).[45] Fish exposed to 0.5 and 1 mg L^{-1} nC_{60} for 48 h exhibited signs of lipid peroxidation in the brain. Zhu et al.[46] reported that nC_{60} generated by water stirring had no impact on lethality within 6 to 18 h of exposure in adult fathead minnow (*Pimephales promelas*); however, as for the largemouth bass, lipid peroxidation was observed. Exposure of zebrafish to nC_{60} caused negative developmental effects that were mitigated after treatment with an antioxidant, supporting the notion that nC_{60} exerts oxidative stress.[47] On the other hand, a critical review of evidence (2007–2011) by Henry et al.[48] suggested that aqueous nC_{60} has minimal potential to produce ROS and that oxidative stress in fish is not induced by environmentally relevant exposure to nC_{60}. A detailed study by Smith et al.[49] demonstrated that SWCNTs was a respiratory toxicant in rainbow trout and caused cellular defects indicative of systemic pathologies.

Effects on marine organisms

Few ecotoxicological studies on marine bacteria, diatoms and other algae, marine invertebrates and fish have been reported. Studies of conventional explosives such as TNT, RDX and HMX have shown that the dissolution rate, transformation rate and sorption testing were generally in close agreement under saline and freshwater conditions. However, nanoparticles in seawater and freshwater have different aggregation behaviour; this will undoubtedly have an impact on the toxicity of nanoenergetics towards marine versus freshwater receptors, even at high dilutions.

It was proposed that marine bivalves, such as *Mytilus edulis*, might take up nanoparticles using endocytosis.[50] Indeed, such modes of uptake may be especially relevant in marine ecosystems, because aggregation of nanoparticles is favoured and should occur on the surface of the organisms. Aggregation was shown to significantly enhance the uptake of 100-nm particles of polystyrene in two marine bivalve species[51].

A study by Wei et al.[52] on the marine green alga *Dunaniella tertiolecta* also supports this theory by showing that only large aggregates (2 µm range) of functionalized MWCNT were able to induce cytotoxic effects. Crustaceans and molluscs are well known for their ability to sequester toxic metals in granules in the hepato-pancreas and other tissues; it might therefore be possible for them to do the same with metal nanoparticles, and this would make these organisms potent bio-accumulators of this type of nanoparticles. In this regard, in *M. edulis* exposed to SiO_2 (3–7 µm length), endocytosis resulted in entry of SiO_2 nanoparticles in gill and digestive gland cells and their distribution in mitochondria, lysosomes and nuclei.[53] Accumulation and oxidative stress were also reported in the digestive glands of *M. edulis* exposed to gold citrate nanoparticles (13 nm) and in the digestive glands of *Crassostrea gigas* exposed to C_{60}-fullerene in vitro and in vivo.[54,55] Another mussel species (*M. galloprovincialis*) exposed to C_{60}-fullerene also exhibited oxidative stress, a number of alterations in hemocytes (invertebrate immune cells) and a decrease in lysosomal stability in the digestive glands.[56,57] Similar effects were reported in *M. edulis* hemocytes exposed to C_{60}-fullerene in the same concentration range,[58] while no effects were observed after exposure to CNT. Studies thus suggest that the major targets of nanoparticle toxicity in marine bivalve molluscs are the immune and digestive systems.

Terrestrial ecotoxicity

Very few data exist by which to assess the potential environmental risk of nanoparticles to soil biota, and this is seen as a key knowledge gap by regulators. In fact, most toxicity studies with soil organisms have been performed

using simple aqueous media instead of soil, and persistence of the nanoparticles in the test media were rarely assessed.

Effects on soil microorganisms

Soil properties are important in determining the toxic effects of nanoparticles. Organic matter content, pH and texture influence the type of microorganisms living in the soil and nanoparticle bioavailability. Tong et al.[59] examined the toxicity of nC_{60} to soil microorganisms using soil respiration, microbial biomass, phospholipid fatty acid analysis and enzyme activities as endpoints. They found no effect of nC_{60} to any endpoint in the soil medium used (silty clay loam, 4 % organic matter, pH 6.9). This was attributed to the strong binding of nC_{60} to soil organic matter. A similar set of experiments examined the effect of nC_{60} added to a neutral soil with low organic carbon content (1.5 %). No effect was found on soil respiration, biomass C and protozoan abundance, but a reduction in bacterial abundance was observed.[60] Metal nanoparticles are generally more toxic for soil microorganisms than carbon-based nanoparticles. Metal and metal oxide nanoparticles can negatively affect microbial activity, abundance and diversity even at concentrations below 1 mg kg^{-1}. For example, silver nanoparticles were shown to reduce some enzyme activities in microorganisms, while copper- and zinc-based nanoparticles reduced bacterial growth and biomass.[61]

Effects on soil invertebrates

Earthworms play an important role in soil biological functioning and organic matter dynamics and therefore many nanoecotoxicology studies have focused on earthworms. Petersen et al.[62] exposed ^{14}C-labeled MWCNTs and SWCNTs to *Eisenia fetida* in two different soils and concluded that they were not readily absorbed into organism tissues. CNTs and C_{60} did not affect the hatchability, growth and survival of earthworms when provided in food, but were toxic to reproduction (cocoon production) at high concentration, i.e., 495 mg kg^{-1} CNT and 1000 mg kg^{-1} of C_{60}.[63] Exposure of earthworms to up to 10,000 mg kg^{-1} of Al_2O_3 nanoparticles resulted in 100 % survival;[64] earthworms avoided the nanoparticle-amended soil at 5000 mg kg^{-1} of Al_2O_3. Bioaccumulation in earthworm tissues increased as the Al_2O_3 particle size decreased.[64] Roh et al.[65] evaluated genotoxicity, survival, growth and reproduction of nano-Ag on the soil nematode *Caenorhabditis elegans*. Silver nanoparticles exerted considerable toxicity, decreasing the reproduction potential and increasing enzyme induction and protein formation. Ma et al.[66] reported that ZnO nanoparticles did not cause significant effect on lethality, behavior, reproduction and transgene expression of *C. elegans*.

Effects on terrestrial plants

Nanoparticles absorbed by plants may enter the food chain and cause serious alterations in humans and animals. Some nanoparticles can enter the plants via the root cell walls.[67,68] Nanoparticles with sizes smaller than the pore diameter may pass through the plant cell wall while others may increase the permeability of cell walls under stress and then penetrate the cells. They may also cross membranes using embedded transport carrier proteins or through ion channels. Airborne nanoparticles that accumulate over leaf surface can penetrate through leaf stomata are then be translocated to various tissues.[69] Accumulation of nanoparticles on photosynthetic surfaces may reduce sunlight availability and hence reduce photosynthetic rate. In the cytoplasm, nanoparticles can bind different organelles and interfere with normal metabolic processes, possibly via the production of ROS.[70]

Nanotoxicity studies on plants have been conducted with various species and nanoparticles. In early studies, Yang and Watts reported inhibition of root elongation as an effect of 13-nm sized Al_2O_3 in maize, cucumber, soybean, cabbage and carrot.[71] Later, Lin and Xing, using larger particles of Al_2O_3 (60 nm), reported no phytotoxicity to radish, rape, ryegrass, lettuce and cucumber, while the root elongation was reduced by 35 % in maize.[72] Other studies indicated that 100-nm and 150-nm Al_2O_3 particles had no adverse effect on the growth of *Phaseolus vulgaris* and *Lolium perenne*, and *Arabidopsis thaliana*, respectively.[73,70] One of the possible reasons for conflicting root elongation results is the variability among the applied nanoparticle size. In a study by Yanik and Vardar,[74] different concentrations of 13-nm Al_2O_3 inhibited wheat root growth consistent with the study of Yang and Watts.[71] Their results also confirmed that toxicity was closely associated with a decrease in particle size. Asztemborska et al.[75] investigated the effects of Al_2O_3 particle size (nano or micro) on bioaccumulation by four different plant species. The most effective uptake and transport through the plants was observed for Al_2O_3 nanoparticles.

Zhu et al.[76] evaluated uptake, translocation and accumulation of Fe_3O_4 nanoparticles in pumpkin and lima bean. The results varied depending on the test-media and the plant species. Fe_3O_4 nanoparticles were detected in roots, stems and leaves in pumpkin plant when grown in liquid medium; they were not detected in lima bean. No uptake was observed when plants were grown in soil and reduced uptake when grown on sand; this may be due to the adherence of nanoparticles to soil and sand grains.

Lin et al.[77] investigated the uptake and translocation of carbon nanomaterials by rice plants (*Oryza sativa*) and they found that fullerene C_{70} could be easily taken up by roots and transported to shoots. Their study also suggested that C_{70} can be transported downward from leaves to roots through phloem if C_{70} enters into plants through plant leaves. Similar results were not observed for MWCNTs even at high concentration (800 mg L^{-1}),[77] which could be due to the relatively larger size of MWCNTs compared to fullerenes.

Conclusion

The use of nanomaterials opens a vast potential for innovative applications in military areas. Several high explosives have been successfully synthesized at the nanometer size including RDX, HMX, CL-20, TNT, TATB, NTO, and PETN, for which the environmental fate and ecotoxicity have been studied only at the micrometer size. The environmental fate and ecological impact of nanoparticles/nanomaterials are far from being completely understood.

Extrapolations from their micrometer-sized counterparts must be made with caution since the extremely small size of nanoparticles results in novel properties and reactivity. Nanoenergetics will contaminate the environment either in the pristine or post-combustion state. It was shown that post-detonation residues of nanothermites settle quickly and thus their transport in aqueous environments should be limited. Most nanoparticles tend to form aggregates that should sediment and accumulate in soils and sediments rather than remaining in suspension in water or in the atmosphere. Aggregation and adsorption of nanoparticles by soil minerals will also limit their mobility. Consequently, the highest concentrations of nanoenergetic residues in the environment should be at or near their source of release.

Due to the extent of environmental contamination associated with the use of traditional explosives such as TNT, RDX and HMX, the military industry is now seeking more environmentally friendly alternatives; however, the physical and chemical nature of CNTs, fullerenes and their derivatives, currently tested in energetic nanocomposites, make them difficult to degrade. Nanoenergetic residues could possibly persist for long periods of time in the environment and accumulate in the food chain. Data in the literature diverge regarding toxicity of nanoparticles depending on the concentrations and the tests used. As particle size decreases, some metal-based nanoparticles are showing increased toxicity to ecological receptors, even if the same material is relatively inert in its bulk form (e.g. Ag, Al_2O_3 and Fe_2O_3).

Overall, the behavior of nanomaterials in the environment remains largely unknown, even for first-generation nanoparticles such as metals and metal oxides (Al, Ag, Fe_2O_3, Fe_3O_4, CeO_2) and carbonaceous materials (CNTs, C_{60}) currently being investigated for their use in energetic materials. A better understanding of the interactions of nanoenergetic components with diverse environmental matrices and evaluation of the ecotoxicological effects of low level exposures will help in performing appropriate environmental risk assessment and to guide military munitions suppliers, munitions acquirement managers, site managers and environmental officers as regards to the future use of nanoenergetics.

Acknowledgements

This work was supported by Defence Research Development Canada (Valcartier), Department of National Defence. The author particularly thanks Dr. Sonia Thiboutot.

References

[1]Berner, M. K., Zarko, V. E., Talawar M. B., *Combust. Explos. Shock Waves*, **2013**, *49(6)*, 625-647. https://doi.org/10.1134/S0010508213060014

[2]Liu, J., Jiang, W., Yang, Q., Song, J., Hao, G., Li, F. S., *Def. Technol.*, **2014**, *10(2)*, 184-189. https://doi.org/10.1016/j.dt.2015.07.002

[3]Choi, W., Hong, S., Abrahamson, J. T., Han, J. H., Song, C., Nair, N., Baik, S., Strano, M. S., *Nat. Mater.*, **2010**, *9(5)*, 423-429. https://doi.org/10.1038/nmat2714

[4]Um, J. E., Yeo, T., Choi, W., Chae, J. S., Kim, H. S., Kim, W. J., *Sci. Adv. Mater.*, **2016**, *8(1)*, 164-170. https://doi.org/10.1166/sam.2016.2622

[5]Smeu, M., Zahid, F., Ji, W., Guo, H., Jaidann, M., Abou-Rachid, H., *J. Phys. Chem.*, **2011**, *115(22)*, 10985-10989. https://doi.org/10.1021/jp201756p

[6]Li, S. F., Gao, F., Zhao, F. Q., Li, S. W., *J. Propul. Technol.*, **2000**, *21(3)*, 75-78.

[7]Jin, B., Peng, R., Chu, S., Huang, Y., Wang, R., *Propellants, Explos., Pyrotech.*, **2008**, *33(6)*, 454-458. https://doi.org/10.1002/prep.200700255

[8]Poda, A. R., Moser, R. D., Cuddy, M. F., Doorenbos, Z., Lafferty, B. J., Weiss, C. A., Harmon, A., Chappell, M. A., Steevens, J. A., *J. Nanomater. Mol. Nanotechnol.*, **2013**, *2(1)*.https://doi.org/10.4172/232 4-8777.1000105

[9]Franklin, N. M., Rogers, N. J., Apte, S. C., Batley, G. E., Gadd, G. E., Casey, P. S., *Environ. Sci. Technol.*, **2007**, *41(24)*, 8484-8490. https://doi.org/10.1021/es071445r

[10]Heymann, D., *Fullerene Sci. Technol.*, **1996**, *4(3)*, 509-515. https://doi.org/10.1080/10641229608001567

[11]Fortner, J. D., Lyon, D. Y., Sayes, C. M., Boyd, A. M., Falkner, J. C., Hotze, E. M., Alemany, L. B., Tao, Y. J., Guo, W., Ausman, K. D., Colvin, V. L., Hughes, J. B., *Environ. Sci. Technol.*, **2005**, *39(11)*, 4307- 4316. https://doi.org/10.1021/es048099n

[12]Lowry, G. V., Wiesner, M. R., *Nanotoxicology: Characterization, Dosing and Health Effects*, Eds: N.A. Monteiro-Riviere, C.L. Tran, Informa Healthcare USA, Inc., New York, **2007**, pp. 369-389. https://doi.org/10.3109/9781420045154-23

[13]Keller, A. A., Wang, H., Zhou, D., Lenihan, H. S., Cherr, G., Cardinale, B. J., Miller, R., Ji, Z., *Environ. Sci. Technol.*, **2010**, *44(6)*, 1962-1967. https://doi.org/10.1021/es90298 7d

[14]Chowdhury, I., Hong, Y., Walker, S. L., *Colloids Surf., A*, **2010**, *368*, 91-95. https://doi.org/10.1016/j.colsurfa.2010.07.019

[15]Liu, J., Legros, S., Ma, G., Veinot, J. G. C., von der Kammer, F., Hofmann, T., *Chemosphere*, **2012**, *87(8)*, 918-924. https://doi.org/10.1016/j.chemosphere.2012.01.045

[16]Chekli, L., Zhao, Y. X., Tijing, L. D., Phuntsho, S., Donner, E., Lombi, E., Gao, B. Y., Shon, H. K., *J. Hazard. Mater.*, **2015**, *284*, 190-200. https://doi.org/10.1016/j.jhazmat. 2014.11.003

[17]Batley, G. E., McLaughlin, M. J., *CSIRO Niche Manufacturing Flagship Report 2008*, Lucas Heights, NSW, **2008**.

[18]Hou, W. C., Jafvert, C. T., *Environ. Sci. Technol.*, **2009**, *43(14)*, 5257-5262. https://doi.org/10.1021/es900624s

[19]BeigzadehMilani, S., Doctoral dissertation, Purdue University, **2015**.

[20]Chen, C. Y., Jafvert, C. T., *Environ. Sci. Technol.*, **2010**, *44(17)*, 6674-6679. https://doi.org/10.1021/es101073p

[21]Chandrasekaran, G., Choi, S. K., Lee, Y. C., Kim, G. J., Shin, H. J., *J. Ind. Eng. Chem.*, **2014**, *20*, 3367-3374. https://doi.org/10.1016/j.jiec.2013.12.022

[22]Zhang, C., Chen, W., Alvarez, P. J., *Environ. Sci. Technol.*, **2014**, *48(14)*, 7918-7923. https://doi.org/10.1021/ es5011175

[23]Parks, A. N., Chandler, G. T., Ho, K. T., Burgess, R. M., Ferguson, P. L., *Environ. Toxicol. Chem.*, **2015**, *34(2)*, 247-251. https://doi.org/10.1002/etc.2791

[24]Schreiner, K. M., Filley, T. R., Blanchette, R. A., Bowen, B. B., Bolskar, R. D., Hockaday, W. C., Masiello, C. A., Raebiger, J. W., *Environ. Sci. Technol.*, **2009**, *43(9)*, 3162-3168. https://doi.org/10.1021/es801873q

[25]Avanasi, R., Jackson, W. A., Sherwin, B., Mudge, J. F., Anderson, T. A., *Environ. Sci. Technol.*, **2014**, *48(5)*, 2792-2797. https://doi.org/10.1021/es405306w

[26]Zhang, L., Petersen, E. J., Habteselassie, M. Y., Mao, L., Huang, Q., *Environ. Pollut.*, **2013**, *181*, 335-339. https://doi.org/10.1016/j.envpol.2013.05.058

[27]Chouhan, R. S., Qureshi, A., Yagci, B., Gülgün, M. A., Ozguz, V., Niazi, J. H., *Chem. Eng. J.*, **2016**, *298*, 1-9. https://doi.org/10.1016/j.cej.2016.04.019

[28]Prabhakar, P. V., Reddy, U. A, Singh, S. P, Balasubramanyam, A., Rahman, M. F., Indu Kumari, S., Agawane, S. B., Murty, U. S. N., Grover, P., Mahboob, M., *J. Appl. Toxicol.*, **2012**, *32(6)*, 436-445. https://doi.org/10.1002/jat.1775

[29]Kumari, M., Rajak, S., Singh, S. P., Kumari, S. I., Kumar, P. U., Murty, U. S., Mahboob, M., Grover, P., Rahman, M. F., *J. Nanosci. Nanotechnol.*, 2012, *12*, 2149-2159. https://doi.org/10.1166/jnn.2012.5796

[30]Asgharian, B., Price, O. T., *Inhal. Toxicol.*, **2007**, *19(13)*, 1045-1054. https://doi.org/10.1080/08958370701626501

[31]Oberdörster, G., Stone, V., Donaldson, K., *Nanotoxicology*, **2007**, *1*, 2-25. https://doi.org/10.1080/17435390701314761

[32]Albini, A., Pagani, A., Pulze, L., Bruno, A., Principi, E., Congiu, T., Gini, E., Grimaldi, A., Bassani, B., De Flora, S., de Eguileor, M., *Int. J. Nanomedicine*, **2015**, *10*, 6133.

[33]Feng, X., Chen, A., Zhang, Y., Wang, J., Shao, L., Wei, L., *Int. J. Nanomedicine*, **2015**, *10*, 4321-4340.

[34]Nel, A., Xia, T., Mädler, L., Li, N., *Science*, **2006**, *311(5761)*, 622-627. https://doi.org/10.1126/science.1114397

[35]Karajanagi, S. S., Vertegel, A. A., Kane, R. S., Dordick, J. S., *Langmuir*, **2004**, *20(26)*, 11594-11599. https://doi.org/10.1021/la047994h

[36]Linse, S., Cabaleiro-Lago, C., Xue, W.-F., Lynch, I., Lindman, S., Thulin, E., Radford, S. E., Dawson, K. A., *Proc. Natl. Acad. Sci.*, **2007**, *104(21)*, 8691-8696. https://doi.org/10.1073/pnas.0701250104

[37]Bondarenko, O., Juganson, K., Ivask, A., Kasemets, K., Mortimer, M., Kahru, A., *Arch. Toxicol.*, **2013**, *87(7)*, 1181-1200.https://doi.org/10.1007/s00204-013-1079-4

[38]Ivask, A., Juganson, K., Bondarenko, O., Mortimer, M., Aruoja, V., Kasemets, K., Blinova, I., Heinlaan, M., Slaveykova, V., Kahru, A., *Nanotoxicology*, **2014**, *8*, 57-71. https://doi.org/10.3109/17435390.2013.855831

[39]Brant, J., Lecoanet, H., Hotze, M., Wiesner, M., *Environ. Sci. Technol.*, **2005**, *39(17)*, 6343-6351. https://doi.org/10.1021/es050090d

[40]Noss, C., Dabrunz, A., Rosenfeldt, R. R., Lorke, A., Schulz, R., Three-dimensional analysis of the swimming behavior of *Daphnia magna* exposed to nanosized titanium dioxide, *PloS One*, **2013**, *8*, e80960. https://doi.org/10.1371/journal.pone.0080960

[41]Navarro, E., Baun, A., Behra, R., Hartmann, N. B., Filser, J., Miao, A. J., Quigg, A., Santschi, P. H., Sigg, L., *Ecotoxicology*, 2008, *17(5)*, 372-386. https://doi.org/10.1007/s10646-008-0214-0

[42]Oberdörster, E., Zhu, S., Blickley, T. M., McClellan-Green, P., Haasch, M. L., *Carbon*, **2006**, *44(6)*, 1112-1120. https://doi.org/10.1016/j.carbon.2005.11.008

[43]Zhao, C. M., Wang, W. X., *Environ. Toxicol. Chem.*, **2011**, *30(4)*, 885-892. https://doi.org/10.1002/etc.451

[44]Zhu, X., Chang, Y., Chen, Y., *Chemosphere*, **2010**, *78*, 209-215. https://doi.org/10.1016/j.chemosphere.2009.11.013

[45]Oberdörster, E., *Environ. Health Perspect.*, **2004**, *112(10)*, 1058-1062. https://doi.org/10.1289/ehp.7021

[46]Zhu, S., Oberdörster, E., Haasch, M. L., *Mar. Environ. Res.*, **2006**, *62*, S5-S9. https://doi.org/10.1016/j.marenvres.2006.04.059

[47]Zhu, X., Zhu, L., Li, Y., Duan, Z., Chen, W., Alvarez, P. J. J., *Environ. Toxicol. Chem.*, **2007**, *26(5)*, 976–979. https://doi.org/10.1897/06-583.1

[48]Henry, T. B., Petersen, E. J., Compton, R. N., *Curr. Opin. Biotechnol.*, **2011**, *22(4)*, 533-537. https://doi.org/10.1016/j.copbio.2011.05.511

[49]Smith, C. J., Shaw, B. J., Handy, R. D., *Aquat. Toxicol.*, **2007**, *82(2)*, 94-109. https://doi.org/10.1016/j.aquatox.2007.02.003

[50]Moore, M. N., *Environ. Int.*, **2006**, *32(8)*, 967-976. https://doi.org/10.1016/j.envint.2006.06.014

[51]Ward, J. E., Kach, D. J., *Mar. Environ. Res.*, **2009**, *68(3)*, 137-142. https://doi.org/10.1016/j.marenvres.2009.05.002

[52]Wei, L., Thakkar, M., Chen, Y., Ntim, S. A., Mitra, S., Zhang, X., *Aquat. Toxicol.*, **2010**, *100(2)*, 194-201. https://doi.org/10.1016/j.aquatox.2010.07.001

[53]Koehler, A., Marx, U., Broeg, K., Bahns, S., Bressling, J., *Mar. Environ. Res.*, **2008**, *66(1)*, 12-14. https://doi.org/10.1016/j.marenvres.2008.02.009

[54]Tedesco, S., Doyle, H., Redmond G., Sheehan, D., *Mar. Environ. Res.*, **2008**, *66(1)*, 131-133. https://doi.org/10.1016/j.marenvres.2008.02.044

[55]Tedesco, S., Doyle, H., Blasco, J., Redmond, G., Sheehan, D., *Comp. Biochem. Physiol., Part C: Toxicol. Pharmacol.*, **2010**, *151(2)*, 167-174.

[56]Canesi, L., Ciacci, C., Betti, M., Fabbri, R., Canonico, B., Fantinati, A. Marcomini, A., Pojana, G., *Environ. Int.*, **2008**, *34(8)*, 1114-1119. https://doi.org/10.1016/j.envint.2008.04.002

[57]Canesi, L., Fabbri, R., Gallo, G., Vallotto, D., Marcomini, A., Pojana, G., *Aquat. Toxicol.*, **2010**, *100(2)*, 168-177. https://doi.org/10.1016/j.aquatox.2010.04.009

[58]Moore, M. N., Readman, J. A., Readman, J. W., Lowe, D. M., Frickers, P. E., Beesley, A., *Nanotoxicology*, **2009**, *3(1)*, 40-45. https://doi.org/10.1080/17435390802593057

[59]Tong, Z., Bischoff, M., Nies, L., Applegate, B., Turco, R. F., *Environ. Sci. Technol.*, **2007**, *41(8)*, 2985-2991. https://doi.org/10.1021/es061953l

[60]Johansen, A., Pedersen, A. L., Karlson, U., Hansen, B. J., Scott-Fordsmand, J. J., Winding, A., *Environ. Toxicol. Chem.*, **2008**, *27(9)*, 1895-1903. https://doi.org/10.1897/07-375.1

[61]Simonin, M., Richaume, A., *Environ. Sci. Pollut. Res.*, **2015**, *22(18)*, 13710-13723. https://doi.org/10.1007/ s11356-015-4171-x

[62]Petersen, E. J., Huang, Q., Weber Jr., W. J., *Environ. Sci. Technol.*, **2008**, *42(8)*, 3090-3095. https://doi.org/10.1021/es071366f

[63]Scott-Fordsmand, J. J., Krogh, P. H., Schaefer, M., Johansen, A., *Ecotoxicol. Environ. Saf.*, **2008**, *71(3)*, 616-619. https://doi.org/10.1016/j.ecoenv.2008.04.011

[64]Coleman, J. G., Johnson, D. R., Stanley, J. K., Bednar, A. J., Weiss, C. A., Boyd, R. E., Steevens, J. A., *Environ. Toxicol. Chem.*, **2010**, *29(7)*, 1575-1580. https://doi.org/10.1002/etc.196

[65]Roh, J. Y., Sim, S. J., Yi, J., Park, K., Chung, K. H., Ryu, D. Y., Choi, J., *Environ. Sci. Technol.*, **2009**, *43(10)*, 3933-3940.

https://doi.org/10.1021/es803477u

[66]Ma, H., Bertsch, P. M., Glenn, T. C., Kabengi, N. J., Williams, P. L., *Environ. Toxicol. Chem.*, **2009**, *28(6)*, 1324-1330. https://doi.org/10.1897/08-262.1

[67]Cifuentes, Z., Custardoy, L., de la Fuente, J. M., Marquina, C., Ibarra, M. R., Rubiales, D., Pérez-de-Luque, A., *J. Nanobiotechnol.*, **2010**, *8(1)*, 26. https://doi.org/10.1186/1477-3155-8-26

[68]Hischemöller, A., Nordmann, J., Ptacek, P., Mummenhoff, K., Haase, M., *J. Biomed. Nanotechnol.*, **2009**, *5(3)*, 278-284. https://doi.org/10.1166/jbn.2009.1032

[69]Hong, J., Peralta-Videa, J. R., Rico, C., Sahi, S., Viveros, M. N., Bartonjo, J., Zhao, L., Gardea-Torresdey, J. L., *Environ. Sci. Technol.*, **2014**, *48(8)*, 4376-4385. https://doi.org/10.1021/es404931g

[70]Lee, C. W., Mahendra, S., Zodrow, K., Li, D., Tsai, Y. C., Braam, J., Alvarez, P. J., *Environ. Toxicol. Chem.*, **2010**, *29(3)*, 669-675. https://doi.org/10.1002/etc.58

[71]Yang, L., Watts, D. J., *Toxicol. Lett.*, **2005**, *158(2)*, 122-132. https://doi.org/10.1016/j.toxlet.2005.03.003

[72]Lin, D., Xing, B., *Environ. Pollut*., **2007**, *150(2)*, 243-250. https://doi.org/10.1016/j.envpol.2007.01.016

[73]Doshi, R., Braida, W., Christodoulatos, C., Wazne, M., O'Connor, G., *Environ. Res*., **2008**, *106(3)*, 296-303. https://doi.org/10.1016/j.envres.2007.04.006

[74]Yanik, F., Vardar, F., *Water, Air, Soil Pollut*., **2015**, *226(9)*, 296. https://doi.org/10.1007/s11270-015-2566-4

[75]Asztemborska, M., Steborowski, R., Kowalska, J., Bystrzejewska-Piotrowska, G., *Int. J. Environ. Res*., **2015**, *9(1)*, 109-116.

[76]Zhu, H., Han, J., Xiao, J. Q., Jin, Y., *J. Environ. Monit*., **2008**, *10(6)*, 713–717. https://doi.org/10.1039/ b805998e

[77]Lin, S., Reppert, J., Hu, Q., Hudson, J. S., Reid, M. L., Ratnikova, T. A., Rao, A. M., Luo, H., Ke, P. C., *Small*, **2009**, *5(10)*, 1128-1132. https://doi.org/10.1002/smll. 200801556

Received: 01.05.2018.
Accepted: 07.06.2018.

INFLUENCE OF RICE HUSK ASH (RHA) ON THE DRYING SHRINKING OF MORTAR

Benyamin Rasoul[a]*

Keywords: Physical properties; chemical composition; fineness; drying shrinkage, crystalline silica; rice husk ash.

The possibility of using of rice husk ash (RHA) in the mortar has been studied. The impact of physical properties and chemical composition of RHA on dry-shrinkage of mortar is a potential problem, especially in the context of the increased use of new generation solutions and the development of new materials to ensure sustainability. In this study, the effects of RHA content, RHA particles size (fineness) and silica structure have been evaluated. Comparisons are made over the full test period and at specific periods ranging from 3 days to 180 days. Incorporation of RHA provided lower dry shrinkage, where the amount of decrease in dry shrinkage increased with increase crystalline silica content and coarse particles size when compared to the control Ordinary Portland Cement (OPC) mixture, with finer RHA giving better improvement. Fine RHA exhibited the highest shrinkage value due to the effect of microfine particles which increases its shrinkage values considerably.

* Corresponding Authors
Fax:
E-Mail: br86@brighton.ac.uk
[a] University of Brighton
[b] 7 Manton road, Brighton/UK

Introduction

Cracking in the concrete bridge decks is a well-documented problem. The problem is particularly severe for a large structure, such as a large concrete floor. Cracking contributes to the deterioration of the structures and allows the ingress of water to the reinforcement, which may lead to corrosion. Cracking increases the maintenance costs, reduces the service life and may result in disruptive and costly repairs. Experience shows that a combination of shrinkage and thermal stresses causes most structure cracking. Efforts have been made to reduce the cracking by designing concrete mixes for minimal shrinkage and improving methods of construction, placement, and finishing. Various admixtures such as silica fume,[1] and carbon fibres[2] have been used to reduce the drying shrinkage. Moreover, to conserve raw materials involved in the production process, eliminate wastes that impact the environment, and to improve the technical properties of concrete, previous studies have demonstrated the feasibility of replacing cement with agro-industrial sub-products. One such example is the ash obtained from burning rice husks, as rice is one of the most cultivated grains in the world. Research has shown that rice husks can improve concrete's mechanical properties[3] and durability.[4] However, few studies have focused on the influence of the rice husk ash content on dry mortar shrinkage.

Experimental

Materials

Three types of RHA (A, B and C) were used in the experimental research are brought from India, While RHA-D obtained by re-burned RHA-C at relatively high temperatures (550 ºC) for 6 h. Properties of rice husk ash, the typical physical properties and chemical composition are given in Tables 1 and 2.

Table 1. Physical properties of RHA samples.

Physical properties	RHA			
	A	B	C	D
Specific surface area, $m^2\ g^{-1}$	0.537	0.587	0.692	0.808
Mean particle size, µm	23.397	20.948	15.804	12.64

Test procedures

The dry-shrinkage of RHA mortar mixtures were measured according to the recommendations made by ASTM standards ASTM C 490 standard.[5] For each mix under investigation, four specimens with dimensions of 400 mm × 50 mm × 50 mm were studied for each composition. After preparing and mixing, each mixture was carefully filled into two prisms moulds. The moulds kept for 24 h then de-moulded and the first reading, which is the initial reading, was recorded by using the apparatus of measurement of dry-shrinkage. The values of dry shrinkage represent the average of two specimens for each batch. The samples were stored in a room at 23 ± 2 °C at a relative humidity of 50 ± 10 % for air drying. Shrinkage readings were performed at 7, 14, 21, 28, 35, 56, 91, and 180 days. These readings were performed in an expandable comparator with a digital marker accurate to 0.001 mm.

Measurement of length change of specimens

To calculate the length change in OPC and RHA mortars, the ASTM C 490 formula was used (eqn. 1), where L = % change in length at x age, L_x = comparator reading of specimen at x age minus comparator reading of reference bar at x age in mm, L_i = Initial comparator reading of specimen minus comparator reading of reference bar at that same time in mm and G = nominal gage length 250.

$$L = \frac{L_x - L_i}{G} 100 \quad (1)$$

Table 2. Chemical composition of RHA samples.

RHA sample	Chemical composition (% wt. of ash)							
	SiO_2	Al_2O_3	Fe_2O_3	CaO	K_2O	P_2O_5	SO_3	MnO
RHA-A	92.10	1.066	0.241	0.719	1.366	0.403	0.076	0.109
RHA-B	89.31	1.389	0.391	0.987	1.813	0.747	1.104	0.166
RHA-C	84.30	1.066	0.175	0.729	1.522	0.675	0.083	0.144
RHA-D	93.49	1.186	0.202	0.971	1.587	0.663	0.084	0.115

Table 3. The mix proportion of RHA mortar dry-shrinkage test.

Batch No.	Cement, kg m^{-3}	RHA, kg m^{-3}	Water, kg m^{-3}	SP*, kg m^{-3}	SP (% wt. of binder)
OPC	587	0	292	1.47	0.25
5	558	29	292	1.47	0.25
10	528	59	292	1.47	0.25
15	499	88	292	1.47	0.25
20	470	117	292	1.47	0.25
30	411	176	290.56	2.94	0.50
40	352	235	287.63	5.87	1.00
50	293.5	293.5	281.76	11.74	2.00
60	235	352	270.02	23.48	4.00

Mix proportion and Curing

The mix proportions of the batches are given in table 3. Where the water binder ratio (w/b) was constant at 0.50 and the fine aggregate (silica sand) used was 1320 kg m^{-3}.

Results and Discussion

The dry shrinkage results for the RHA mortars mixes under investigation are presented in Figure 1 and Table 4. These results correspond to the average micro deformations (mm mm^{-1}) of two specimens tested for each replacement ratio. In general, the dry shrinkage of all the mixes ranged from 32 to 1016×10^{-4} mm mm^{-1} (RHA-A), 18 to 1052×10^{-4} mm mm^{-1} (RHA-B), 8 to 1242×10^{-4} mm mm^{-1} (RHA-C), 134 to 1391×10^{-4} mm mm^{-1} (RHA-D), compare to 424 to 1143×10^{-4} mm mm^{-1} for OPC mortar, over 180 days. The mixes containing RHA-A and RHA-B had values ranging from 18 to 1052×10^{-4} mm/mm, which is considered low for OPC mortar even at 60 % replacement ratio. The RHA-D displayed the highest values of dry shrinkage among all RHA mixes including the OPC mortar reference, at all replacement ratio and curing time.

Table 4. Dry shrinkage strain (mm/mm) of RHA mortars at different replacement ratio compare to OPC mortar at different ages.

Days	5 % RHA mortar				OPC mortar
	A	B	C	D	
3	0.0118	0.004	0.0388	0.0462	0.0424
7	0.0246	0.0224	0.0476	0.0644	0.0500
14	0.0386	0.0482	0.0580	0.0770	0.0590
28	0.0554	0.0714	0.0766	0.0990	0.0794
56	0.0758	0.0912	0.0996	0.1154	0.1004
91	0.0776	0.0980	0.1054	0.1264	0.1120
180	0.0796	0.0995	0.1068	0.1298	0.1143

Days	10 % RHA mortar				
	A	B	C	D	
3	0.0112	0.0034	0.0172	0.0254	
7	0.0328	0.0214	0.0370	0.0408	
14	0.0414	0.0458	0.0502	0.0532	
28	0.0576	0.0612	0.0636	0.0742	
56	0.0646	0.0776	0.0832	0.0890	
91	0.0678	0.0816	0.0882	0.0882	
180	0.0689	0.0823	0.0891	0.1024	
Days	**15 % RHA mortar**				
	A	**B**	**C**	**D**	
3	0.0056	0.0018	0.0158	0.0300	
7	0.0270	0.0158	0.0336	0.0396	
14	0.0396	0.0390	0.0438	0.0530	
28	0.0502	0.0550	0.0598	0.0680	
56	0.0568	0.0662	0.0694	0.0794	
91	0.0646	0.0762	0.0806	0.0862	
180	0.0659	0.0785	0.0819	0.0881	
Days	**20 % RHA mortar**				
	A	**B**	**C**	**D**	
3	0.0148	0.0046	0.0138	0.0178	
7	0.0216	0.0232	0.0298	0.0358	
14	0.0290	0.0362	0.0390	0.0506	
28	0.0484	0.0536	0.0564	0.0660	
56	0.0596	0.0646	0.0670	0.0780	
91	0.0672	0.0700	0.0744	0.0840	
180	0.0685	0.0711	0.0768	0.0852	
Days	**30 % RHA mortar**				
	A	**B**	**C**	**D**	
3	0.0034	0.0032	0.0100	0.0152	
7	0.0284	0.0246	0.0306	0.0400	
14	0.0304	0.0334	0.0362	0.0512	
28	0.0444	0.0484	0.0538	0.0648	
56	0.0624	0.0670	0.0754	0.0788	
91	0.0664	0.0706	0.0808	0.0890	
180	0.0670	0.0723	0.0827	0.0910	

Days	40 % RHA mortar				
	A	**B**	**C**	**D**	
3	0.0092	0.0110	0.0008	0.0134	
7	0.0330	0.0282	0.0084	0.0406	
14	0.0490	0.0464	0.0228	0.0529	
28	0.0604	0.0664	0.0462	0.0730	
56	0.0794	0.0848	0.0826	0.0966	
91	0.0818	0.0868	0.0928	0.1016	
180	0.0829	0.0881	0.0937	0.1043	
Days	**50 % RHA mortar**				
	A	**B**	**C**	**D**	
3	0.0122	0.014	0.0076	0.0176	
7	0.0388	0.035	0.018	0.0406	
14	0.0590	0.056	0.0322	0.0656	
28	0.0770	0.0786	0.0626	0.0856	
56	0.0874	0.0892	0.0826	0.1076	
91	0.0926	0.0994	0.1018	0.1164	
180	0.0939	0.1002	0.1065	0.1198	
Days	**60 % RHA mortar**				
	A	**B**	**C**	**D**	
3	0.0176	0.0144	0.0116	0.0234	
7	0.055	0.0436	0.0312	0.0582	
14	0.0644	0.0712	0.053	0.0768	
28	0.0832	0.0872	0.0732	0.0944	
56	0.0934	0.0972	0.108	0.1176	
91	0.0994	0.1014	0.1242	0.1326	
180	0.1016	0.1052	0.1267	0.1391	

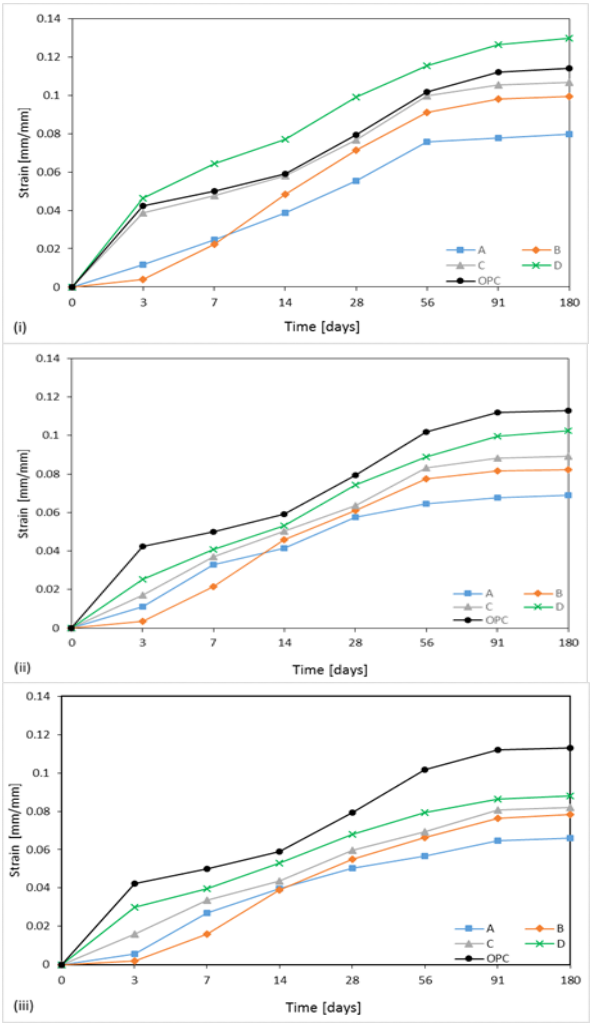

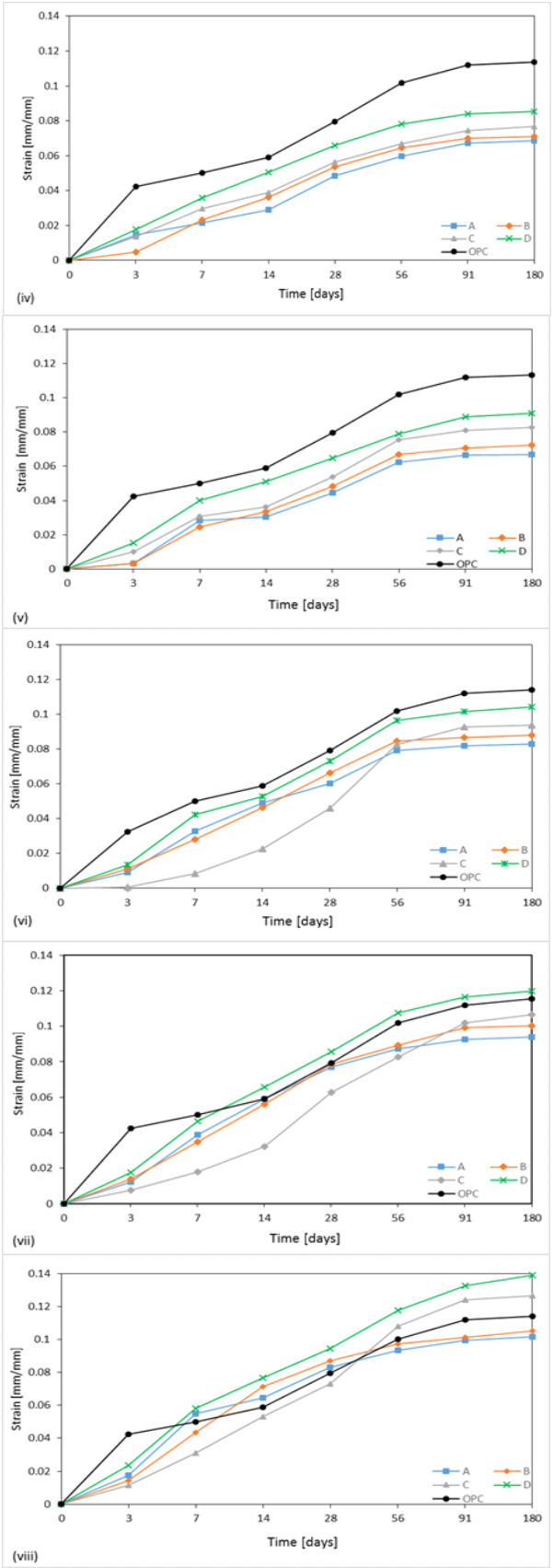

Figure 1. Effect of RHA properties to the replacement ratio on the dry shrinkage of RHA mortars compared to OPC at; (i) 5%, (ii) 10%, (iii) 15%, (iv) 20%, (v) 30%, (vi) 40%, (vii) 50%, and (viii) 60% replacement ratio.

Table 5. Effect of RHA on the dry-shrinkage of mortar at different ages.

RHA %	Strain (mm mm^{-1})						
	RHA-A						
Days →	3	7	14	28	56	91	180
5	-0.0118	-0.0246	-0.0386	-0.0554	-0.0758	-0.0776	-0.0796
10	-0.0112	-0.0334	-0.0414	-0.0576	-0.0646	-0.0678	-0.0689
15	-0.0056	-0.0270	-0.0396	-0.0502	-0.0568	-0.0646	-0.0659
20	-0.0148	-0.0216	-0.0290	-0.0484	-0.0596	-0.0652	-0.0685
30	-0.0034	-0.0284	-0.0304	-0.0444	-0.0624	-0.0664	-0.0670
40	-0.0092	-0.0330	-0.0490	-0.0604	-0.0794	-0.0818	-0.0829
50	-0.0122	-0.0388	-0.059	-0.0770	-0.0874	-0.0926	-0.0939
60	-0.0176	-0.0550	-0.0644	-0.0832	-0.0934	-0.0954	-0.1016

RHA %	Strain (mm mm^{-1})						
	RHA-B						
Days →	3	7	14	28	56	91	180
5	-0.004	-0.0224	-0.0482	-0.0714	-0.0912	-0.098	-0.0995
10	-0.0034	-0.0214	-0.0458	-0.0612	-0.0776	-0.0816	-0.0823
15	-0.0018	-0.0158	-0.0390	-0.0550	-0.0662	-0.0762	-0.0785
20	-0.0046	-0.0232	-0.0362	-0.0536	-0.0646	-0.0700	-0.0711
30	-0.0032	-0.0246	-0.0334	-0.0484	-0.0670	-0.0706	-0.0723
40	-0.0110	-0.0282	-0.0464	-0.0664	-0.0848	-0.0868	-0.0881
50	-0.0140	-0.0350	-0.0560	-0.0786	-0.0892	-0.0994	-0.1002
60	-0.0144	-0.0436	-0.0712	-0.0872	-0.0972	-0.1004	-0.1052

RHA %	Strain (mm mm^{-1})						
	RHA-C						
Days →	3	7	14	28	56	91	180
5	-0.0388	-0.0476	-0.0580	-0.0766	-0.0996	-0.1054	-0.1068
10	-0.0172	-0.0370	-0.0502	-0.0636	-0.0832	-0.0882	-0.0891
15	-0.0158	-0.0336	-0.0438	-0.0598	-0.0694	-0.0806	-0.0819
20	-0.0138	-0.0298	-0.0390	-0.0564	-0.0670	-0.0744	-0.0768
30	-0.0100	-0.0306	-0.0362	-0.0538	-0.0754	-0.0806	-0.0827
40	-0.0008	-0.0086	-0.0228	-0.0462	-0.0806	-0.0928	-0.0937
50	-0.0076	-0.0180	-0.0322	-0.0626	-0.1064	-0.1018	-0.1065
60	-0.0116	-0.0312	-0.0530	-0.0732	-0.1120	-0.1242	-0.1267

RHA %	Strain (mm mm^{-1})						
	RHA-D						
Days →	3	7	14	28	56	91	180
5	-0.0462	-0.0644	-0.0770	-0.0990	-0.1154	-0.1264	-0.1298
10	-0.0254	-0.0408	-0.0532	-0.0742	-0.0890	-0.0996	-0.1024
15	-0.0300	-0.0396	-0.0530	-0.0680	-0.0794	-0.0862	-0.0881
20	-0.0178	-0.0358	-0.0506	-0.0660	-0.0780	-0.0840	-0.0852
30	-0.0152	-0.0400	-0.0512	-0.0648	-0.0788	-0.0890	-0.0910
40	-0.0134	-0.0406	-0.0592	-0.0730	-0.0966	-0.1016	-0.1043
50	-0.0176	-0.0424	-0.0656	-0.0856	-0.1076	-0.1164	-0.1198
60	-0.0184	-0.0532	-0.0768	-0.0944	-0.1176	-0.1296	-0.1421

Effect the fineness of RHA particles

Based on the experimental results the RHA mean particles size, amorphous silica percentage are particularly effective on the dry shrinkage of RHA mortars performance. Generally, there is a linear correlation between the particle size distributions to the development of dry shrinkage of RHA mortars which is presented in Table 5 (Figure 1).

Effect of RHA properties on the dry shrinkage of mortar

As shown in Figure 1, there is a general trend on dry shrinkage decreasing with increasing replacement ratio up to 20 %. This can be justified by the pozzolanic and the filler effects.[6] This fact has been reported by other researchers also.[7,8] These results correspond to the average micro deformations (10^{-6} mm/mm) of the two specimens tested for each mix. From data presented in Table 2, it can be noted that RHA-D at 5 % replacement ratio exhibited higher dry shrinkage than that of reference mortar by about 12.25 %. The increases in dry shrinkage strain of RHA-D at 5 %, can be justified by the pozzolanic and the filler effects.[6] Even though, RHA-C consists of entirely amorphous silica, it exhibited lower dry-shrinkage compare to OPC mortar at 5 % replacement ratio. This behaviour of RHA-C specimens can be attributed to the high residual carbon content. On the other hand, the dry shrinkage of RHA mortar specimens was noticeably reduced by the addition of RHA-A and B. Specimens at 180 days showed a reduction in dry shrinkage strain by 30.11 % and 12.64 % compared to OPC. Partial replacement crystalline silica with coarse particles of RHA provides a positive effect on the dry shrinkage of mortar, which is attributed to the filler effect. This correlation was determined for 20% RHA; however, it's same for other RHA replacement ratio. Where, mortar specimens containing RHA-C and D with a particles size of 15.804 and 12.64 µm, exhibited higher dry-shrinkage compare to RHA-A and B with 23.397 and 20.948 µm, respectively. According to Habeeb and Fayyadh[6] RHA with fine particles significantly affected on the dry shrinkage of concrete mixtures containing 20 % RHA, Thus, it can be concluded that the addition of RHA content higher amount of microfine particles to mortar would increase the drying shrinkage.

Conclusions

The drying shrinkage was significantly affected by RHA silica structure and fineness of particles. RHA-D recorded the higher shrinkage value, while RHA-A exhibited lower values than the control, this could be due to the effect of the microfine particles.

The use of the RHA for application in mortar showed excellent performance in drying shrinkage at 60 % RHA-A and B compare to control mortar. Strains due to drying shrinkage are ranged from 1016 to 1391 $\times 10^{-6}$ (mm/mm) at 180 days.

The parameters affecting the dry shrinkage strain are RHA silica structure, size of RHA grain particles and replacement ratio. The effective mean particle size of RHA on mitigating dry shrinkage of RHA mixtures was suggested to be over 20.0 µm, where with coarser particles size less dry shrinkage reported.

Maximum dry shrinkage development registered was in between 3 to 7 days for all RHA mortars mixtures.

The behaviour of RHA dry shrinkage strain is linear concerning the composition of RHA. Where, with a high amount of crystalline silica content and coarser particles size, lower dry shrinkage was obtained as shown with results of RHA-B to A.

As the proportion of replacement ratio increases the dry shrinkage of the mortar decreased up to 15% RHA-A, and 20% RHA-B, C and D, beyond this limitation increased.

A linear relationship is established between compressive strength and dry shrinkage, this correlation is more significant for the dry shrinkage, and it will be more adequate if the shrinkage is measured starting from the setting time. It is shown that there is a strength value for each type of RHA mortar mixtures from which the shrinkage behaviour between blended cement and ordinary cement changes.

According to the literature, there is some debate among the researchers, about the advantageous use of RHA in mortar and concrete in respect of dry shrinkage. However, this study proves the point view of the majority of the researchers about the positive impact of RHA on the decrease of mortar dry shrinkage at the extended period.

References

[1]Xu, Y., Chung, D. D. L., Reducing the drying shrinkage of cement paste by admixture surface treatments, *Cement, Concrete Res.*, **2000**, *30* (*2*), 241-245. https://doi.org/10.1016/S0008-8846(99)00239-2

[2]Park, S. B., Lee, B. I., echanical properties of carbon-®ber-reinforced polymer-impregnated cement composites, *Cement Concrete Compos.*, **1993**, *15* (*3*), 153–163. https://doi.org/10.1016/0958-9465(93)90004-S

[3]De Sensale, G. R., Strength development of concrete with rice-husk ash, *Cement, Concrete Compos.*, **2006**, *28*(2), pp.158-160. https://doi.org/10.1016/j.cemconcomp.2005.09.005

[4]Cezar D. S., *Characteristics of durability of concrete with fly ash and rice husk ash with and without processing*, Master's thesis. Santa Maria: College of Civil Engineering, Federal University of Santa Maria, **2011**, 143.

[5]ASTM, C., 490/C 490 M-09. Standard Practice for Use of Apparatus for the Determination of Length Change of Hardened Cement Paste, Mortar, and Concrete, **2009**.

[6]Habeeb, G., Fayyadh, M., Rice Husk Ash Concrete: the Effect of RHA Average Particle Size on Mechanical Properties and Drying Shrinkage, *Aust. J. Basic Appl. Sci.*, **2009**, *3*(*3*), 1616-1622.

[7]Zhang, M. H. and Malhotra, M. V., High-performance concrete incorporating rice husk ash as supplementary cementing material, *ACI Mater. J.*, **1996**, *93*(*6*), 629-636.

[8]Chatveera, B., Lertwattanaruk, P., Durability of conventional concretes containing black rice husk ash, *J. Environ. Manage.*, **2011**, *92(1)*, 59-66. doi: 10.1016/j.jenvman.2010.08.007.

Received: 10.05.2018.
Accepted: 13.06.2018.

AN EXPEDITIOUS AND GREEN APPROACH FOR THE SYNTHESIS OF 2-AMINO-4*H*-CHROMENES USING A CATALYST OF NATURAL ORIGIN

H. D. Bhosale,[a] S. U. Shisodia,[a] R. D. Ingle,[a]* P. S. Kendrekar,[b]* A. U. Shisodia,[a] László Kótai,[c] and R. P. Pawar[a]*

Keywords: Green synthesis; benzaldehyde; malononitrile; catalyst of natural origin; ultrasound; 2-amino-4H-chromenes.

A highly efficient three-component one step system for the synthesis of 2-amino-4H-chromens is developed. Excellent yields were obtained simply by mixing malononitrile, aromatic aldehyde and α-napthol in lemon juice as a catalyst of natural origin and solvent, avoiding using hazardous organic solvents. The main advantages of this method are its green method character, short reaction time and simple workup procedures and the lack of using any metal containing catalysts.

* Corresponding Authors
E-Mail: rppawar@yahoo.com, rajitaingle@yahoo.in, kkpravin@gmail.com
[a] Department of Chemistry, Deogiri College, Station Road, Aurangabad, Maharashtra- 431005, Maharashtra, India
[b] Departmental Health Science, Central University of Technology, Bloemfontein 9300, Free State, South Africa
[c] Research Centre for Natural Sciences, Hungarian Academy of Sciences, P. O. Box 17, HU-1525, Budapest, Hungary

Introduction

Heterocyclic compounds containing chromene moieties are of considerable interest as they are a class of natural and synthetic compounds that possess a great variety of biological as well as pharmaceutical activities.[1–5] Chromene derivatives having a wide range of valuable pharmacological properties, such as diuretic, spasmolytic, analgesic, anticoagulant, anti-anaphylactic, anti-tumor activities.[6–8.] Some among them are extremely effective against such kind of diseases which influenced by nitrogen-activated protein kinase enzyme inhibitors. Some of them have antimicrobial activity ,[11] cytotoxic effect against human cancer cells,[12] antiallergic activity,[13] central nervous system influencing activity,[14] antiproliferation activty.[15] Several derivatives are also widely used as agrochemicals,[16] antioxidant[17] and anti-inflammatory agent.[18].

Literature survey revealed the several reports on one pot three components system for the synthesis of 2-amino-4H-chromenes. This reaction can be catalyzed by both basic as well as by acidic compounds. As acid catalyst can be used heteropoly acids like $H_{14}[NaP_5W_{30}O_{110}]$,[19] methanesulfonic acid (MSA),[20] p-toluenesulfonic acid (PTSA),[21] tungstic acid functionalized mesoporous SBA-15 silica,[22] Fe_3O_4@sulphochitosan nanoparticles (CS-SO_3H NPs),[23] sulfonic acid-functionalized metal-organic frameworks like MIL-101(Cr),[24] etc.

Recently, reactions carried out in green solvent like water have attracted much attention of researchers for environmentally benign. In the continuation of our previous work on the synthesis of 2 amino-4H-chromenes,[25-27] here we report three component one pot synthesis of biologically important substituted 2-amino-4H-chromenes using lemon juice as green catalyst and solvent under ultrasound waves irradiation.

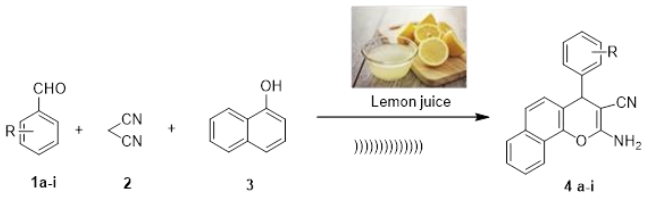

Scheme 1. Synthesis of 2-amino-(substituted phenyl)-4H-benzo[h]chromene-3-carbonitriles

Experimental

All starting materials and chemical reagents were purchased from SD fine chemical company and used without further purification; melting points were determined in open capillaries using electrochemical MK3 apparatus. IR spectra were recorded using Perkin-Elmer FT-IR spectrometer by using KBr pellets, 1H & 13C NMR spectra were recorded on Bruker 250 MHz NMR spectrometer in $CDCl_3$ and chemical shift values were recorded in δ (ppm) by using tetramethylsilane (Me_4Si) as an internal standard.

General procedure for the synthesis of 2-amino-4H-chromenes

In a single neck round bottom flask, p-methoxy benzaldehyde 1 (1 mmol), malononitrile 2 (1.2 mmol), α-napthol 3 (1 mmol) were taken and in it lemon juice (extract) 10 mL was added and this resulting reaction mixture was irradiated to ultrasound for 20-30 minutes. The progress of reaction was monitored by thin layer chromatography. After completion of reaction, the reaction mixture was poured on crushed ice and the solid obtained was filtered, washed with cold water and recrystallized from

methanol to afford pure product. The obtained product was characterized by using ^{1}H NMR and ^{13}C NMR spectroscopy. The NMR spectroscopic data of the known compounds (**4a-4i**) are agreed well with the literature data.[28-30]

2-Amino-4-(4-nitrophenyl)-4H-benzo[h]chromene-3-carbonitrile (4g)

^{1}H NMR (250 MHz, $CDCl_3$) δ (ppm): 8.25 (d, 1H, ArH), 7.79 (t, 1H, Ar-H), 7.51 (m, 3H, Ar-H), 7.43 (d, 2H, Ar-H), 7.15 (d, 2H, ArH), 7.01 (d, 1H, ArH), 6.92 (s, 2H, NH_2), 4.83(s, 1H, CH).

2-Amino-4-(2-bromophenyl)-4H-benzo[h]chromene-3-carbonitrile (4i)

^{1}H NMR (250 MHz, $CDCl_3$) δ (ppm): 8.21 (d, 1H, ArH), 7.81 (d, 1H, Ar-H), 7.51 (m, 3H, Ar-H), 7.49 (m, 2H, Ar-H), 7.23 (m, 3H, ArH), 6.96 (s, 2H, NH2), 4.87 (s, 1H, CH).

Results and discussion

In this communication, we have reported the use of lemon juice as a catalyst and solvent for the synthesis of 2-amino-(substituted phenyl)-4H-benzo[h]chromene-3-carbonitrile derivatives (Scheme 1). We have performed the three-component condensation reaction using lemon juice under sonification conditions (45 ºC). We got better result regarding purity and product yield of synthesized compounds.

We have carried out the standard model reaction of p-methoxybenzaldehyde, malononitrile and α-naphthol in presence of lemon juice. In order to optimize reaction conditions we have carried out reaction at room temperature, 80 ºC and under ultrasonication conditions at (45 ºC) and found that reaction carried out under sonification condition have given good yield in short reaction time (Table 1).

Table 1. Model reaction of p-methoxybenzaldehyde, malononitrile and α-naphthol in presence of lemon juice

Reaction condition	*T*, C°	Time, h	Yield, %
Without catalyst	50 ºC	7	00
Room temperature	30 ºC	10	70
Heating	80 ºC	6	78
Sonification	45 ºC	1/3	84

The scope of catalyst on different substituted benzaldehydes has been examined such as electron donating or withdrawing groups, all the results obtained are presented in (Table 2).

Table 2. Synthesis of 2-amino-(substituted phenyl)-4H-benzo[h]chromene-3-carbonitrile (**4a-i**)

Arylaldehyde	Product	Time, min	Yield, %	Melting point, ºC	
				Observed	Reported
Benzaldehyde	**4a**	30	76	274-275	205-207[28]
o-Chlorobenzaldehyde	**4b**	28	77	231-232	253-254[28]
p-Chlorobenzaldehyde	**4c**	27	78	210-212	229-200[28]
m-Methoxybenzaldehyde	**4d**	29	74	247-248	248-250[29]
p-Methoxybenzaldehyde	**4e**	20	76	187-189	193-194[28]
m-Nitrobenzaldehyde	**4f**	25	82	233-237	212-214[30]
p-Nitrobenzaldehyde	**4g**	28	84	240-241	238-239[28]
p-Hydroxybenzaldehyde	**4h**	29	76	242-243	244-245[28]
p-Bromobenzaldehyde	**4i**	27	72	238-239	240-241[28]

Reaction works well for all substituted benzaldehydes which means reaction is compatible with this catalytic system. However, ortho substituted derivatives have shown less yield as compare to the meta and para substituted due to electronic effect.

Conclusion

In conclusion, we have successfully synthesized, 2-amino-4H-chromens by using ultrasound waves from malononitrile, benzaldehyde and α-napthol by using lemmon juice as an biocatalyst as well as it acts as solvent, it show high catalytic activity and clean reaction procedure, easy workup, with high yields of products and purity.

Acknowledgment

The authors are thankful to the Dr. S. N. Thore, Principal Deogiri College for continuous encouragement and providing laboratory facilities.

References

[1]Curini, M., Cravotto, G., Epofano, F., Chemistry and Biological Activity of Natural and Synthetic Prenyloxycoumarins, *Curr. Med. Chem.*, **2006**, *13*, 199–222. DOI: 10.2174/092986706775197890.

[2]Litvinov, Y. M., Shestopalov, A. M., Synthesis, Structure, Chemical Reactivity, and Practical Significance of 2-Amino-4H-pyrans, *Adv. Heterocycl. Chem.*, **2011**, *103*, 175–260. DOI: 10.1016/B978-0-12-386011-8.00003-4.

[3]Desimone, R. W., Currie, K. S., Mitchell, S. A., Darrow, J. W., Pippin, D. A., Privileged Structures: Applications in Drug Discovery, *Comb. Chem. High Throughput Screen*., **2004**, *7*, 473–794, DOI: 10.2174/1386207043328544

[4]Patchett A. A., Nargund R. P., Privileged structures – an update, *Ann. Rep. Med. Chem*., **2000**, *35*, 289–298. https://doi.org/10.1016/S0065-7743(00)35027-8

[5]Kemnitzer W., Kasibhatla S., Jiang S., Zhang, H., Zhao, J., Jia, S., Xu, L., Crogan-Grundy, C., Denis, R., Barriault, N., Vaillancourt, L., Charron, S., Dodd, J., Attardo, G., Labrecque, D., Lamothe, S., Gourdeau, H., Tseng, B., Drewe, J., Cai, S. X., Discovery of 4-aryl-4H-chromenes as a new series of apoptosis inducers using a cell- and caspase-based high-throughput screening assay. 2. Structure-activity relationships of the 7- and 5-, 6-, 8-positions, *Bioorg. Med. Chem. Lett.*, **2005**, *15*, 4745–4751. DOI: 10.1016/j.bmcl.2005.07.066.

[6]Hafez, E. A., Elnagdi, M. H., Elagamey, A. G. A., El Taweel, F. M. A. A., Nitriles in Heterocyclic Synthesis: Novel Synthesis of Benzo[c]coumarin and of Benzo[c]pyrano[3,2-c]quinoline Derivatives, *Heterocycles*, **1987**, *26*, 903–907. DOI: 10.3987/R-1987-04-0903.

[7]Sofan, M. A., El-Taweel, F. M. A. A., Elnagdi, M. H., Studies on Cinnamonitriles: The Reaction of Cinnamonitriles with Cyclopentanone, *Liebigs Ann. Chem*. **1989**, 935–936. DOI: 10.1002/jlac.198919890246

[8]Bonsignore L. , Loy G., Secci D., Calignano A., Synthesis and pharmacological activity of 2-oxo-(2H) 1-benzopyran-3-carboxamide derivatives, *Eur. J. Med. Chem.* **1993**, *28*, 517–520. DOI: 10.1016/0223-5234(93)90020-F

[9]Kidwai, M. , Saxena, S., Khan, M. K. R. and Thukral, S. S., Aqua mediated synthesis of substituted 2-amino-4H-chromenes and in vitro study as antibacterial agents, *Bioorg. Med. Chem. Lett.*, **2005**, *15*, 4295. DOI: 10.1016/j.bmcl.2005.06.041

[10]Anderson, D. R., Hegde, S., Reinhard, E. , Gomez, L., Vernier, W. F., Lee L., Liu, S., Sambandam, A., Snider, P. A., Masih, L., Aminocyanopyridine inhibitors of mitogen activated protein kinase-activated protein kinase 2 (MK-2), *Bioorg. Med. Chem. Lett*. **2005**, *15*, 1587. DOI: 10.1016/j.bmcl.2005.01.067.

[11]Naimi-Jamal, M. R., Mashkouri, S., Sharifi, A., An efficient, multicomponent approach for solvent-free synthesis of 2-amino-4H-chromene scaffold, *Mol. Divers*., **2010**, *14*, 473–477. DOI: 10.1007/s11030-010-9246-5

[12]Kemnitzer, W., Kasibhatla, S., Jiang, S. C., Zhang, H., Zhao, J. H., Jia, S. J., Xu, L. F., Crogan-Grundy, C., Denis, R., Barriault, N., Vaillancourt, L., Charron, S., Dodd, J., Attardo, G., Labrecque, D., Lamothe, S., Gourdeau, H., Tseng, B., Drewe, J. and. Cai, S. X., Discovery of 4-aryl-4H-chromenes as a new series of apoptosis inducers using a cell- and caspase-based high-throughput screening assay. 2. Structure-activity relationships of the 7- and 5-, 6-, 8-positions, *Bioorg. Med. Chem. Lett*., **2005**, *15*, 4745–4751. DOI: 10.1016/j.bmcl.2005.07.066.

[13]Ling, R., Yoshida, M., Mariano, P. S., Exploratory Investigations Probing a Preparatively Versatile, Pyridinium Salt Photoelectrocyclization−Solvolytic Aziridine Ring Opening Sequence, *J. Org Chem.*, **1996**, *61*, 4439–4449. DOI: 10.1021/jo960316i.

[14]Anderson, D. R., Hegde, S., Reinhard, E., Gomez, L., Vernier, W. F., Lee, L., Liu, S., Sambandam, A., Snider, P. A., Masih, L., Aminocyanopyridine inhibitors of mitogen activated protein kinase-activated protein kinase 2 (MK-2), *Bioorg. Med. Chem. Lett*., **2005**, *15*, 1587–1590. DOI: 10.1016/j.bmcl.2005.01.067

[15]Dell, C. P., Williams, A. C., Pyrano[3,2-h]quinolines for treating restenosis, European Patent Appl EP 1004584, **1993**.

[16]Hafez, E. A., Elnagdi, M. H., Elagemey, A. G. A., . El-Taweel, F. M. A., Nitriles in Heterocyclic Synthesis: Novel Synthesis of Benzo[c]coumarin and of Benzo[c]pyrano[3,2-c]quinoline Derivatives, *Heterocycles*, **1987**, *26*, 903-907. DOI: 10.3987/R-1987-04-0903

[17]Vats, P., Hadjimitova, V., Yoncheva, K., Kathuria, A., Sharma, A., Chand, K., Duraisamy, A. J., Sharma, A. K., Sharma, A. K., Saso, L., Sharma, S. K., Chromenone and quinolinone derivatives as potent antioxidant agents, *Med. Chem. Res*., **2014**, *23*, 4907. DOI 10.1007/s00044-014-1054-5

[18]Hiramoto, K., Nasuhara, A., Michiloshi, K., Kato, T., Kikugawa, K., DNA strand-breaking activity and mutagenicity of 2,3-dihydro-3,5-dihydroxy-6-methyl-4H-pyran-4-one (DDMP), a Maillard reaction product of glucose and glycine, *Mutat. Res*., **1997,** *395*, 47–56. DOI: 10.1016/S1383-5718(97)00141-1

[19]Heravi, M. M., Bakhtiari, K., Zadsirjan, V., Bamoharram, F. F., Heravic, O. M., Aqua mediated synthesis of substituted 2-amino-4H-chromenes catalyzed by green and reusable Preyssler heteropolyacid, *Biol. Med. Chem. Lett.*, **2007**, *17*, 4262–4265. DOI: 10.1016/j.bmcl.2007.05.023

[20]Heravi, M. M., Baghernejad, B., Oskooie, H. A., A Novel and Efficient Catalyst to One‐Pot Synthesis of 2-Amino-4H-chromenes by Methanesulfonic Acid, *J. Chin. Chem. Soc*. **2008**, *55*, 659-662. DOI: 10.1002/jccs.200800098

[21]Baghernejad, B., Heravi, M. M., Oskooie, H. A., A Novel and Efficient Catalyst to One-Pot Synthesis of 2-Amino-4H-chromenes by p-Toluenesulfonic Acid, *Korean J. Chem. Soc*., **2009**, *53*, 631-634.

[22]Kundu, S. K., Mondal, J., Bhaumik, A., *Dalton Trans*., **2013**, *42*, 10515–10524. DOI: 10.1039/C3DT50947H

[23]Mohammadi, R., Kassaee, M. Z., Sulfochitosan encapsulated nano-Fe_3O_4 as an efficient and reusable magnetic catalyst for green synthesis of 2-amino-4H-chromen-4-yl phosphonates, *J. Mol. Catal. A. Chem*., **2013**, *380*, 152–158. DOI:10.1016/j.molcata.2013.09.027

[24]Saikia, M., Saikia, L., Sulfonic acid-functionalized MIL-101(Cr) as a highly efficient heterogeneous catalyst for one-pot synthesis of 2-amino-4H-chromenes in aqueous medium, *RSC Adv*., **2016**, *6*, 15846-15853. DOI 10.1039/C5RA28135K

[25]Throat, V. V., Dake, S. A., Katariya, M. V., Pawar, R. P., Cesium carbonate as a heterogeneous reusable and efficient catalyst for the synthesis of 2-amino-4H-chromene derivatives, *Der Chemica Sinica*, **2015**, *6(6)*, 37-50.

[26]Khandare, P. M., Ingale, R. D., Taware, A. S., Shisodia, S. U., Pawar, S. S., Kotai, L. and Pawar, R. P., One-pot synthesis and biological evaluation of pyranopyrazoles in aqueous medium, *Eur. Chem. Bull.*, **2017,** *6(9)*, 410-414. DOI: 10.17628/ecb.2017.6.410-414. 410.

[27]Joshi, V. M., Magar, R. L., Throat, P. B., Tekale, S. U., Patil B. R., Kale, M. P., Pawar, R. P., Novel one-pot synthesis of 4H-chromene derivatives using amino functionalized silica gel catalyst, *Chin. Chem. Lett*., **2014**, *25(3)*, 455–458. DOI: 10.1016/j.cclet.2013.12.016.

[28]Shinde, S., Damate, S., Morbale, S., Patil M., Patil, S. S., Aegle marmelos in heterocyclization: greener, highly efficient, one-pot three-component protocol for the synthesis of highly functionalized 4H-benzochromenes and 4H-chromenes, *RSC Adv*., **2017**, *7*, 7315-7328. DOI: 10.1039/c6ra28779d.

[29]Mohammad Nikpassand, Leila Zare Fekri, Parvin Ahmadi., Grinding synthesis of 2-amino-4*H*-chromenes using 3,3-(butane 1,4-diyl) bis (1,2-dimethyl-1*H*-imidazole-3-ium)Br-can as a novel reagent, J. Chilean Chem. Soc., **2017**, *62(1)*, 3399-3402. DOI: 10.4067/S0717-97072017000100019.

[30]Kumbhar, Arjun, Jadhav, Sanjay, Shejwal, Rajendra, Rashinkar, Gajanan, Salunkhe, Rajshri, Application of novel multi-cationic ionic liquids in microwave assisted 2-amino-4H-chromene synthesis, *RSC Adv*., **2016**, *6*, 19612-19619. DOI: 10.1039/c6ra01062h.

Received: 10.05.2018.
Accepted: 13.06.2018.

KINETIC EQUATIONS OF FREE-RADICAL NONBRANCHED-CHAIN PROCESSES OF ADDITION TO ALKENES, FORMALDEHYDE, AND OXYGEN

Michael M. Silaev[a]

Keywords: Low-reactive radical, autoinhibitor, competing reaction, nonbranched-chain addition, thermochemical data.

The aim of this study was to devise simple kinetic equations to describe *ab initio* initiated nonbranched-chain processes of addition of saturated free-radical to double bonds of unsaturated molecules in binary reaction systems of saturated and unsaturated components. In these processes the formation rate of the molecular addition products (1:1 adducts) as a function of concentration of the unsaturated component reaches a limiting value. Five reaction schemes are suggested for the addition processes. The proposed schemes include the reaction competing with chain propagation reactions through a reactive free radical. The chain evolution stage in these schemes involves three or four types of free radicals. One of them is relatively low-reactive and inhibits the chain process by shortening of the kinetic chain length. Based on the suggested schemes, nine rate equations are deduced using quasi-steady-state treatment. These equations provide good fits for the non-monotonic (peaking) dependences of the formation rates of the molecular products (1:1 adducts) on the concentration of the unsaturated component in the binary systems. The unsaturated compound in these systems is both a reactant and an autoinhibitor generating low-reactive free radicals. A similar kinetic description is applicable to the nonbranched-chain process of the free-radical hydrogen oxidation, in which the oxygen with the increase of its concentration begins to act as an oxidation autoinhibitor (or an antioxidant). The energetics of the key radical-molecule reactions are considered.

* Corresponding Authors
E-Mail: mmsilaev@rc.chem.msu.ru
[a] Chemistry Faculty, Lomonosov Moscow State University, Vorobievy Gory, Moscow 119991, Russia

Introduction

A free radical may be low-reactive if its unpaired *p*-electron is delocalized, e.g., over conjugated bonds as in the case of allyl radical CH_2=$CH\dot{C}H_2$ or along a double bond from carbon to the more electronegative oxygen as in the case of formyl radical $H\dot{C}$=O. The activity of a free radical is also connected to the heat of reaction in which it participates. In nonbranched-chain processes of addition of reactive free radical (addendum) to double bonds of molecules, the formation of rather low-reactive free radicals in reactions, which are parallel to or competing with propagation *via* a reactive radicals, lead to chain termination, because these low-reactive radicals do not participate in further chain propagation and because they decay when colliding with each other or with chain-carrier reactive radicals thus resulting in inefficient expenditure of the latter and process inhibition.

In similar processes involving the addendum and inhibitor radicals in diffusion controlled bimolecular chain-termination reactions of three types, the dependences of the rate of molecular 1:1 adduct formation on the concentration of the unsaturated component (which is the source of low-reactive free radicals in a binary system of saturated and unsaturated components) have a maximum, usually in the region of small (optimal) concentrations. The progressive inhibition of nonbranched chain processes upon exceeding this optimal concentration may be an element of self-regulation of the natural processes returning them to a steady state condition.

Here, addition reactions of reactive free radicals to multiple bonds of alkene, formaldehyde, and oxygen molecules to give 1:1 adduct radicals are taken as examples to consider the role of low-reactive free radicals as inhibitors of the nonbranched chain processes at moderate temperatures. In the case of oxidation, there are tetraoxyl 1:2 adduct radical arising upon addition of a peroxyl 1:1 adduct radical to molecular oxygen at high enough concentrations of the latter.

The 1:1 adduct radical (which is the heaviest and the largest among the free radicals that result from the addition of one addendum radical to the double bond of the molecule) may have an increased energy owing to the energy liberated in the transformation of a double bond to an ordinary bond (30-130 kJ mol^{-1} for the gas phase under standard conditions[1-4]). Therefore, it can decompose or react with one of the surrounding molecules in the place of its formation without diffusing in the solution and, hence, without participating in radical-radical chain termination reactions. Which of the two reactions of the adduct radical, the reaction with the saturated component or the reaction with the unsaturated component, dominates the kinetics of the process will depend on the reactivity and concentration ratios of the components in the binary system.

Earlier[5,6] there were attempts to describe such peaking dependences fragmentarily, assuming that the saturated or unsaturated component is in excess, in terms of the direct and inverse proportionalities, respectively, that result from the simplification of a particular case of the kinetic equation set up by the quasi-steady-state treatment of binary copolymerization involving fairly long chains.[5] This specific equation is based on an irrational function, whose plot is a monotonic curve representing the dependence of the product formation rate on the concentration of the unsaturated component. This curve comes out of the origin of

coordinates, is convex upward, and has an asymptote parallel to the abscissa axis. Replacing the component concentrations with the corresponding mole fractions generates a peak in this irrational function and thereby makes it suitable to describe the experimental data.[7] However, this circumstance cannot serve as a sufficient validation criterion for the mechanism examined, because the new property imparted to the function by the above artificial transformation does not follow from the solution of the set of algebraic equations that are set up for the reaction scheme accepted for the process in a closed system and express the equality of the steady-state formation and disappearance rates of the reactive intermediates.

This publication presents a comprehensive review of the nonbranched-chain kinetic models developed for particular types of additions of saturated free radicals to multiple bonds.[8-14] It covers free radical additions to alkenes,[10,11] their derivatives,[8,9] formaldehyde,[8,9,12] and molecular oxygen[13,14] (which can add an unsaturated radical as well) yielding various 1:1 molecular adducts, whose formation rates as a function of the unsaturated compound concentration pass through a maximum (free radical chain additions to the C=N bond have not been studied adequately). In the kinetic description of these nontelomerization chain processes, the reaction between the 1:1 adduct radical and the unsaturated molecule, which is in competition with chain propagation through a reactive free radical ($^{\bullet}PCl_2$, $C_2H_5\dot{C}HOH$, etc.), is included for the first time in the chain propagation stage. This reaction yields a low-reactive radical (such as $CH_2=C(CH_3)\dot{C}H_2$ or $H\dot{C}=O$) and thus leads to chain termination because this radical does not continue the chain and thereby inhibits the chain process.[8] We will consider kinetic variants for the case of comparable component concentrations with an excess of the saturated component[10,11] and the case of an overwhelming excess of the saturated component over the unsaturated component.[8,9,12] Based on the reaction schemes suggested for the kinetic description of the addition process, we have derived kinetic equations with one to three parameters to be determined directly.

Reducing the number of unknown parameters in a kinetic equation will allow one to decrease the narrowness of the correlation of these parameters and to avoid a sharp build-up of the statistical error in the nonlinear estimation of these parameters in the case of a limited number of experimental data points.[15] The rate constant of the addition of a free radical to the double bond of the unsaturated molecule, estimated as a kinetic parameter, can be compared to its reference value if the latter is known. This provides a clear criterion to validate the mathematical description against experimental data.

The kinetic equations were set up using the quasi-steady-state treatment. This method is the most suitable for processes that include eight to ten or more reactions and four to six different free radicals and are described by curves based on no more than three to seven experimental points. In order to reduce the exponent of the $2k_5[R_1^{\bullet}]^2$ term in the $d[R_1^{\bullet}]/dt = 0$ equation to unity,[8] we used the following condition for the early stages of the process: $k_6 = \sqrt{2k_5 2k_7}$ and, hence, $V_1 = V_5 + 2V_6 + V_7 = (\sqrt{2k_5}[R_1^{\bullet}] + \sqrt{2k_7}[R_2^{\bullet}])^2$.[16] Here, $[R_1^{\bullet}]$ and $[R_2^{\bullet}]$ are the concentrations of the addendum radical and the low-reactive (inhibitor) radical, respectively; V_1 is the initiation rate; V_5, $2V_6$, and V_7 are the rates of the three types of diffusion-controlled quadratic-law chain termination reactions; $2k_5$ and $2k_7$ are the rate constants of the loss of identical free radicals *via* the reactions $R_1^{\bullet} + R_1^{\bullet}$ and $R_2^{\bullet} + R_2^{\bullet}$, respectively; k_6 is the rate constant of the loss of different free radicals *via* the $R_1^{\bullet} + R_2^{\bullet}$ reaction (Schemes 1-5). The kinetic equations thus obtained fit the peaking rate curves well throughout the range of unsaturated component concentrations in the binary systems. Our mathematical simulation was based on experimental data obtained for γ-radiation-induced addition reactions for which the initiation rate V_1 is known. The analysis of stable liquid-phase products was carried out by the gas chromatographic method.

Addition to the C=C bond of alkenes and their derivatives

When reacting with alkenes not inclined to free-radical polymerization, the free radicals originating from inefficient saturated telogens, such as alcohols[17] and amines[18], usually add to the least substituted carbon atom at the double bond, primarily yielding a free 1:1 adduct radical. This radical accumulates an energy of 90–130 kJ mol^{-1}, which is released upon the transformation of the C=C bond to an ordinary bond (according to the data reported for the addition of nonbranched C_1–C_4 alkyl radicals to propene and of similar C_1 and C_2 radicals to 1-butene in the gas phase under standard conditions[1-4]). Such adduct radicals, which do not decompose readily for structural reasons, can abstract the most labile atom from a neighbouring molecule of the saturated or unsaturated component of the binary reaction system, thus turning into a 1:1 adduct molecule.

The consecutive and parallel reactions involved in this free-radical nonbranched-chain addition process are presented below (Scheme 1). In the case of comparable component concentrations with a non-overwhelming excess of the saturated component, extra reaction (1b) ($k_{1b} \neq 0$) is included in the initiation stage.[10,11] In the case of an overwhelming excess of the saturated component reaction (1b) is ignored ($k_{1b} = 0$).[8,9,12]

Comparable component concentrations

In this scheme, I is an initiator (e.g., a peroxide[5,12,13]), $R_0^{\bullet}$ is a reactive (initiating) radical, A and B are hydrogen or halogen atoms,[2,5,17-24] $R_1^{\bullet}$ is $^{\bullet}PCl_2$,[19] $^{\bullet}CCl_3$,[20] alkyl,[2,5] 1-hydroxyalkyl,[5,6,17,22-24] or a similar functionalized reactive addend radical,[5] $R_2^{\bullet}$ is an alkenyl radical (allyl or higher),[2,5,17-24] 1-hydroxyalkenyl,[5,17,18,23,24] or a similar functionalized low-reactive radical (inhibitor),[5,18] $R_3^{\bullet}$ is a saturated reactive 1:1 adduct radical, R_0A, R_0B, and R_1A are saturated molecules, R_2B is an unsaturated molecule (alkene or its derivative) and R_3A and R_3B are 1:1 adduct molecules. Prod designates the molecular products resulting from the dimerization or disproportionation of free radicals. The chain evolution (propagation and inhibition) stage of Scheme 1 include consecutive reactions 2 and 3, parallel

(competing) reaction pairs 3 and 4, and consecutive-parallel reaction pair 2-4.

Chain initiation

1. $I \xrightarrow{2k_1} 2R_0^{\bullet}$;

1a. $R_0^{\bullet} + R_1A \xrightarrow{k_{1a}} R_0A + R_1^{\bullet}$;

1b. $R_0^{\bullet} + R_2A \xrightarrow{k_{1b}} R_0A + R_2^{\bullet}$.

Chain propagation

2. $R_1^{\bullet} + R_2B \xrightarrow{k_2} R_3^{\bullet}$;

3. $R_3^{\bullet} + R_1A \xrightarrow{k_3} R_3A + R_1^{\bullet}$.

Inhibition

4. $R_3^{\bullet} + R_2B \xrightarrow{k_4} R_3B + R_2^{\bullet}$.

Chain termination

5. $2R_1^{\bullet} \xrightarrow{2k_5}$ Prod;

6. $R_1^{\bullet} + R_2^{\bullet} \xrightarrow{k_6}$ Prod;

7. $2R_2^{\bullet} \xrightarrow{2k_7}$ Prod.

Scheme 1. Consecutive and parallel reactions involved in the free-radical nonbranched-chain addition processes.

The initiation reaction 1 is either the decomposition of a chemical initiator,[5,17,18] a reaction induced by light[5,17,18] or ionizing radiation.[19-13] The overall rate of chain initiation (reactions 1, 1a, and 1b) is determined by the rate of the rate-limiting step ($k_{1b} > k_{1a}$). The reaction between the free radical $R_2^{\bullet}$, which results from reactions 1b and 4, and the saturated molecule R_1A is energetically unfavourable because it implies the formation of the free radical $R_1^{\bullet}$, which is less stable than the initial one.

The addition reaction 2 may be accompanied by the abstraction reaction 2a. $R_1^{\bullet} + R_2B \xrightarrow{k_{2a}} R_1B + R_2^{\bullet}$ which yields the product R_1B *via* a nonchain mechanism.

Reaction 2a does not regenerate the addend radical $R_1^{\bullet}$ and is not necessary for a kinetic description of the process, because the rate ratio of reactions 2 and 2a, $V_2/V_{2a} = k_2/k_{2a}$, is independent of the concentration of the unsaturated component R_2B in the system. The inhibition of the nonbranched-chain addition process is due to reaction 4, in which the adduct radical $R_3^{\bullet}$ is spent in an inefficient way, since this reaction, unlike reaction 3, does not regenerate $R_1^{\bullet}$. The inhibiting effect is also due to the loss of chain carriers $R_1^{\bullet}$ through their collisions with low-reactive unsaturated radicals $R_2^{\bullet}$, but to a much lesser extent.

The rates of the formation (V, mol dm^{-3} s^{-1}) of the 1:1 adducts R_3A (*via* a chain mechanism) and R_3B (*via* a nonchain mechanism) in reactions 3 and 4 are given by the eqns. (1) and (2) where V_1 is the rate of the initiation reaction 1; $l = [R_1A]$ and $x = [R_2B]$ are the molar concentrations of the initial components, with $l > x$; k_2 is the rate constant of the addition of the $R_1^{\bullet}$ radical from the saturated component R_1A to the unsaturated molecule R_2B (reaction 2) and $\gamma = k_{1a}/k_{1b}$ and $\alpha = k_3/k_4$ are the rate constant ratios for competing (parallel) reactions (α is the first chain-transfer constant for the free-radical telomerization process[5]). The rate ratio for the competing reactions is $V_3/V_4 = \alpha l/x$, and the chain length is $\nu = V_3/V_1$.

$$V_3(R_3A) = \frac{[\gamma l/(\gamma l + x)]V_1 \alpha l k_2 x}{k_2 x^2 + (\alpha l + x)\sqrt{2k_5 V_1}}, \quad (1)$$

$$V_4(R_3B) = \frac{[\gamma l/(\gamma l + x)]V_1 k_2 x^2}{k_2 x^2 + (\alpha l + x)\sqrt{2k_5 V_1}}, \quad (2)$$

Earlier mathematical simulation [8] demonstrated that replacing the adduct radical R_3 with the radical R_2 [5] in the reaction between identical radicals and in the reaction involving R_1 gives rise to a peak in the curve of the 1:1 adduct formation rate as a function of the concentration of the unsaturated component. Reaction 1b, which is in competition with reaction 1a, is responsible for the maximum in the curve described by eqn. (2), and reaction 4, which is in competition with reaction (3), is responsible for the maximum in the curve defined by eqn. (1).

The number of unknown kinetic parameters to be determined directly (k_2,α, and γ) can be reduced by introducing the condition $\gamma \cong \alpha$, which is suggested by the chemical analogy between the competing reactions pairs 1a-1b and 3-4. For example, the ratios of the rate constants of the reactions of $^{\bullet}OH$, $CH_3O^{\bullet}$, $^{\bullet}CH_3$, $NO_3^{\bullet}$, and $H_2PO_4^{\bullet}$ with methanol to the rate constants of the reactions of the same radicals with ethanol in aqueous solution at room temperature are 0.4–0.5.[25,26]

For the same purpose, the rate constant of reaction 2 in the kinetic equation can be replaced with its analytical expression $k_2 = \alpha l_m \sqrt{2k_5 V_1}\big/ x_m^2$, which is obtained by solving the quadratic equation following from the reaction rate extremum condition $\partial V_{3,4}(1:1\,\text{Adduct})/\partial x = 0$, where $\partial V_{3,4}(1:1\,\text{Adduct}) = V_3 + V_4$.

After these transformations, the overall formation rate equation for the 1:1 adducts R_3A and R_3B (which may be identical, as in the case of R_3H[5,8,9,12,13,18-21]) appears as eqns. (3) and (3a) where l_m and x_m are the component concentrations l and x at the points of maximum of the function. Provided that V_1 is known, the only parameter in eqn. (3a) to be determined directly is α. If V_1 is known only for the saturated component R_1A, then, for the binary system containing comparable R_1A and R_2B concentrations, it is

better to use the quantity λV_1 , where $\lambda = l/(l + x)$ is the mole fraction of R_1A, in place of V_1 in eqns. (3) and (3a).

$$V_{3,4}(\text{1:1 Adduct}) = \frac{V_1 \alpha l k_2 x}{k_2 x^2 + (\alpha l + x)\sqrt{2k_5 V_1}} = \quad (3)$$

$$= \frac{V_1 \alpha l x}{x^2 + (\alpha l + x)x_m^2 / \alpha l_m}, \quad (3a)$$

The two variable concentrations in the kinetic eqn. (3), l and x, can be reduced to one variable by replacing them with the corresponding mole fractions. Substituting the expression $k_2 = \left\{\alpha\left[(1/\chi_m) - 1\right]^2 - 1\right\}\sqrt{2k_5 V_1}\Big/(l_m + x_m)$, derived from the rate extremum condition, into this transformed equation for the binary system containing comparable component concentrations, we obtain eqn. (3b) where $1 - \chi = l/(l + x)$ and $\chi = x/(l + x)$ are the mole fractions of the components R_1A and R_2B ($0 < \chi < 1$), respectively, and χ_m is the χ value at the point of maximum.

$$V_{3,4}(\text{Adduct 1:1}) = \frac{V_1 \alpha (1-\chi)\chi}{\chi^2 + [\alpha(1-\chi) + \chi]\Big/\left\{\alpha[(1/\chi_m) - 1]^2 - 1\right\}}, \quad (3b)$$

The overall formation rate of the 1:1 adducts R_3A and R_3B is a sophisticated function of the formation and disappearance rates of the radicals $R_1^{\bullet}$ and $R_2^{\bullet}$ i.e., $V(R_3A, R_3B) = (V_{1a} + V_3 - V_5) - (V_{1b} + V_4 - V_7)$. The application of the above rate equations to particular single nonbranched-chain additions is illustrated in Figure 1. Curve *1* represents the results of simulation in terms of eqn. (3b) for the observed 1:1 adduct formation rate as a function of the mole fraction of the unsaturated component in the phosphorus trichloride–methylpropene reaction system at 303 K.[19] In an earlier work,[10] the methylpropene concentration in this system was overvalued by a factor of 1.7 when it was derived from the mole fractions given in.[19]

In this simulation, the ^{60}Co γ-radiation dose rate was set at P = 0.01 Gy s^{-1} and the initiation yield was taken to be $G(^{\bullet}PCl_2)$ = 2.8 particles per 100 eV (1.60×10^{-17} J) of the energy absorbed by the solution.[19] The product of reaction 3 is $Cl_2PCH_2C(Cl)(CH_3)CH_3$ (two isomers), $V_1 = 4.65 \times 10^{-9}$ mol dm^{-3} s^{-1} at $\chi = 0$, and $2k_5 = 3.2 \times 10^8$ dm^3 mol^{-1} s^{-1}. This leads to $\alpha = (2.5 \pm 0.4) \times 10^3$, and the rate constant of reaction 2 derived from this α value is $k_2 = (1.1 \pm 0.2) \times 10^4$ dm^3 mol^{-1} s^{-1}.

Note that, if the R_2–B bond dissociation energy for the unsaturated component of the binary system is approximately equal to or above, not below, the R_1–A bond dissociation energy for the saturated component, then the rate of reaction 4 relative to the rate of the parallel reaction 3 (chain propagation through the reactive free radical $R_1^{\bullet}$) will be sufficiently high for adequate description of R_3A and R_3B adduct formation in terms of eqns. (1)-(3b) only at high temperatures.[20] In the phosphorus trichloride–propene system, the difference between the R_2–B (B = H) and R_1–A (A = Hal) bond dissociation energies in the gas phase under standard conditions [1] is as small as 5 kJ mol^{-1}, while in the tetrachloromethane–methylpropene (or cyclohexene) and bromoethane–2-methyl-2-butene systems, this difference is 20.9 (37.7) and ~24 kJ mol^{-1}, respectively.

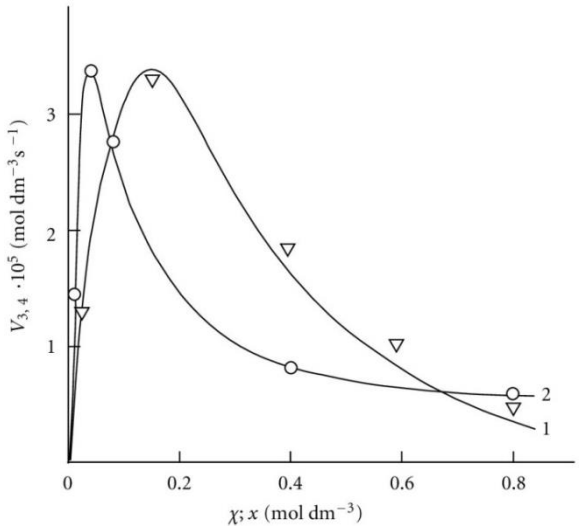

Figure 1. Reconstruction of the functional dependences (curves) of the product formation rates $V_{3,4}$ (*1*, ▽) on the mole fraction of the unsaturated component (χ) from empirical data (symbols) using Eqn. (3b) (model optimization with respect to the parameter α) for the phosphorus trichloride–methylpropene reaction system at 303 K[19] (standard deviation of $S_Y = 2.58 \times 10^{-6}$) and (*2*, ○) on the concentration of the unsaturated component (x) from empirical data (symbols) using Eqn. (4a) (model optimization with respect to V_1, x_m, and α) for the 2-propanol–2-propen-1-ol system at 433 K [23] ($S_Y = 5.91 \times 10^{-7}$).

Excess of the saturated component

If the concentration of the saturated component exceeds the concentration of the unsaturated component in the binary system, reaction 1b can be neglected. If this is the case (k_{1b} = 0), then, in the numerators of the rate equations for reactions 3 and 4 (eqns. (1) and (2)), $\gamma l/(\gamma l + x) = 1$ and the overall rate equation for the formation of the 1:1 adducts R_3A and R_3B will appear as

$$V_{3,4}(\text{1:1 Addduct}) = \frac{V_1(\alpha l + x)k_2 x}{k_2 x^2 + (\alpha l + x)\sqrt{2k_5 V_1}} = \quad (4)$$

$$= \frac{V_1 x}{\dfrac{x^2}{\alpha l + x} + \left(\dfrac{\sqrt{\alpha l_m}}{x_m} + \dfrac{1}{\sqrt{\alpha l_m}}\right)^{-2}} \quad (4a)$$

where the parameters are designated in the same way as in eqns. (1)–(3a), $l >> x$, and

$$k_2 = \left[\left(\sqrt{\alpha l_m}\Big/ x_m\right) + \left(1\Big/\sqrt{\alpha l_m}\right)\right]^2 \sqrt{2k_5 V_1}$$

is determined from the condition

$\partial V_{3,4}(\text{1:1 Adduct}) / \partial x = 0$.

The rate equations for the chain termination reactions 5–7 (Scheme 1, $k_{1b} = 0$) are identical to eqns. (12)-(14) (see below) with $\beta = 0$.

If it is necessary to supplement Scheme 1 for $k_{1b} = 0$ with the formation of R_1B *via* the possible nonchain reaction 2a, the parameter k_{2a} should be included in the denominator of eqn. (4) to obtain $k_2x^2 + (\alpha l + x)(k_{2a}x + \sqrt{2k_5V_1})$. The analytical expression for k_2 in the case of $k_{2a} \neq 0$ is identical to the expression for k_2 for eqn. (4). The equation for the rate $V_{2a}(R_1B)$ can be derived by replacing k_2 with k_{2a} in the numerator of eqn (4) containing k_{2a} in its denominator.

Curve *2* in Figure 1 illustrates the good fit between eqn. (4a) and the observed 1:1 adduct formation rate as a function of the concentration of the unsaturated component in the reaction system 2-propanol–2-propen-1-ol at 433 K.[8,9] In this description, we used a ^{60}Co γ-radiation dose rate of P = 4.47 Gy s^{-1}.[23] The product of reactions 3 and 4 is $CH_3(CH_3)C(OH)CH_2CH_2CH_2OH$, and $2k_5 = 1.0 \times 10^{10}$ dm^3 mol^{-1} s^{-1}. The following parameters were obtained: $V_1 = (3.18 \pm 0.4) \times 10^6$ mol dm^{-3} s^{-1}, $x_m = (3.9 \pm 0.5) \times 10^{-2}$ mol dm^{-3}, and $\alpha = (6.8 \pm 0.8) \times 10^{-2}$. The rate constant of reaction 2 derived from this α is $k_2 = (1.0 \pm 0.14) \times 10^5$ dm^3 mol^{-1} s^{-1}.

Addition to the C=O bond of formaldehyde

Free radicals add to the carbon atom at the double bond of the carbonyl group of dissolved free (unsolvated, monomer) formaldehyde. The concentration of free formaldehyde in the solution at room temperature is a fraction of a percent of the total formaldehyde concentration, which includes formaldehyde chemically bound to the solvent.[27] The concentration of free formaldehyde exponentially increases with increasing temperature.[28] The energy released as a result of this addition, when the C=O bond is converted into an ordinary bond, is 30 to 60 kJ mol^{-1} (according to the data on the addition of C_1–C_4 alkyl radicals in the gas phase under standard conditions[1-4]). The resulting free 1:1 adduct radicals can both abstract hydrogen atoms from the nearest-neighbour molecules of the solvent or unsolvated formaldehyde and, due to its structure, decompose by a monomolecular mechanism including isomerization.[9,12]

Addition of Free 1-Hydroxyalklyl Radicals with Two or More Carbon Atoms

Free 1-hydroxyalkyl radicals, which result from the abstraction of a hydrogen atom from the carbon atom bonded to the hydroxyl group in molecules of saturated aliphatic alcohols except methanol under the action of chemical initiators,[29,30] light,[17,31] or ionizing radiation,[32,33] add at the double bond of free formaldehyde dissolved in the alcohol, forming 1,2-alkanediols,[8,9,12,29-36] carbonyl compounds, and methanol[8,33] *via* the chain mechanism. The yields of the latter two products in the temperature range of 303 to 448 K are one order of magnitude lower. In these processes, the rate determining role in the reactivity of the alcohols can be due to desolvation of formaldehyde in alcohol–formaldehyde solutions, which depends both on the temperature and on the polarity of the solvent.[28,33] For the γ-radiolysis of 1(or 2)-propanol–formaldehyde system at a constant temperature, the dependences of the radiation-chemical yields of 1,2-alkanediols and carbonyl compounds as a function of the formaldehyde concentration show maxima and are symbatic.[8,32] For a constant total formaldehyde concentration of 1 mol dm^{-3}, the dependence of the 1,2-alkanediol yields as a function of temperature for 303-473 K shows a maximum, whereas the yields of carbonyl compounds and methanol increase monotonically[33] along with the concentration of free formaldehyde.[28] In addition to the above products, the nonchain mechanism in the γ-radiolysis of the solutions of formaldehyde in ethanol and 1- and 2-propanol gives ethanediol, carbon monoxide, and hydrogen in low radiation-chemical yields, which, however, exceed the yields of the same products in the γ-radiolysis of individual alcohols.[8,9,33] The available experimental data can be described in terms of Scheme 2.

Chain initiation

1. $I \xrightarrow{2k_1} 2\,R_0^{\bullet}$;

1a. $R_0^{\bullet} + ROH \xrightarrow{k_{1a}} ROH + {}^{\bullet}R_{(-H)}OH$.

Chain propagation

2. ${}^{\bullet}R_{(-H)}OH + CH_2O \xrightarrow{k_2} R_{(-H)}(OH)CH_2O^{\bullet}$;

3. $R_{(-H)}(OH)CH_2O^{\bullet} + ROH \xrightarrow{k_3} R_{(-H)}(OH)CH_2OH + {}^{\bullet}R_{(-H)}OH$;

3a. $R_{(-H)}(OH)CH_2O^{\bullet} \xrightarrow{k_{3a}} R_{(-2H)}HO + {}^{\bullet}CH_2OH$ (or $R'R''CO + {}^{\bullet}CH_2OH$);

3b. ${}^{\bullet}CH_2OH + ROH \xrightarrow{k_{3b}} CH_3OH + {}^{\bullet}R_{(-H)}OH$.

Inhibition

4. $R_{(-H)}(OH)CH_2O^{\bullet} + CH_2O \xrightarrow{k_4} R_{(-H)}(OH)CH_2OH + {}^{\bullet}CHO$.

Chain termination

5. $2\,{}^{\bullet}R_{(-H)}OH \xrightarrow{2k_5} R_{(-H)}(OH)R_{(-H)}OH$ (or: $ROH + R_{(-2H)}HO$, $ROH + R'R''CO$);

6. ${}^{\bullet}R_{(-H)}OH + {}^{\bullet}CHO \xrightarrow{k_6} R_{(-H)}(OH)CHO$ (or: $R_{(-2H)}HO + CH_2O$, $R'R''CO + CH_2O$, $ROH + CO$);

7. $2\,{}^{\bullet}CHO \xrightarrow{2k_7} HC(O)CHO$ (or: $CH_2O + CO$, $2CO + H_2$).

Scheme 2. Addition of free 1-hydroxyalkyl radicals to formaldehyde.

In these reactions, I is an initiator, e.g., a peroxide;[29,30] $R_0^{\bullet}$ a reactive radical (initiator radical); R an alkyl group; ROH, a saturated aliphatic alcohol, either primary or secondary, beginning from ethanol; $^{\bullet}CH_2OH$, the hydroxymetyl fragment radical; $^{\bullet}R_{(-H)}OH$, the reactive 1-hydroxyalkyl addendum radical, beginning from 1-hydroxyethyl; $R_{(-H)}(OH)CH_2O^{\bullet}$, the reactive hydroxyalkoxyl 1:1 adduct radical; $^{\bullet}CHO$, the low-reactive formyl radical (inhibitor radical); R_0H, the molecular product; $R_{(-H)}(OH)CH_2OH$, 1,2-alkanediol; $R_{(-2H)}HO$, an aldehyde in the case of a primary alcohol and an R'R"CO ketone in the case of a secondary alcohol; $R_{(-H)}(OH)R_{(-H)}OH$, a vicinal alkanediol and $R_{(-H)}(OH)CHO$, a hydroxyaldehyde. The chain evolution stage of Scheme 2 includes consecutive reaction pairs 2–3, 2–3a, and 3a–3b, parallel (competing) reaction pairs 3–3a, 3–3b, 3–4, and 3a–4 and consecutive–parallel reactions 2 and 4.

Scheme 2 does not include the same types of radical-molecule reactions as were considered for Scheme 1. In addition, it seems unlikely that free adduct radicals will add to formaldehyde at higher temperatures. An addition reaction is unlikely because this would result in an ether bond. The addition of hydroxymethyl radicals to formaldehyde, which is in competition with reaction 3b, is not included as well, because there is no chain formation of ethanediol at 303-448 K.[33] At the same time, small amounts of ethanediol can form *via* the dimerization of a small fraction of hydroxymethyl radicals, but this cannot have any appreciable effect on the kinetics of the overall process. The addition of free formyl radicals to formaldehyde cannot proceed at a significant rate, indicated by the lack of formation of glycol aldehyde in the systems examined .[33]

The mechanism of the decomposition of the free adduct radical *via* reaction 3a, which includes the formation of an intramolecular H···O bond and isomerization, can be represented as follows.[8,9,12]

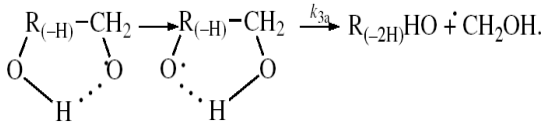

Scheme 2. Possible mechanism of reaction 3a.

The probability of the occurrence of reaction 3a should increase with increasing temperature. This is indicated by experimental data presented above.[8,9,12] The decomposition of the hydroxyalkoxyl radical. $R_{(-H)}(OH)CH_2O^{\bullet}$ (reaction 3a) is likely to be endothermic. The endothermic nature of reaction 3a is indirectly indicated by the fact that the decomposition of simple C_2–C_4 alkoxyl radicals $RO^{\bullet}$ in the gas phase is accompanied by heat absorption[2-4] (ΔH°_{298} = 30–90 kJ mol^{-1}). Reaction 3b, subsequent to reaction 3a, is exothermic, and its heat for C_2–C_3 alcohols in the gas phase is ΔH°_{298} = –40 to –60 kJ mol^{-1}.[2-4] As follows from the above scheme of the process, reactions 3a and 3b, in which the formation and consumption of the highly reactive free radical hydroxymethyl take place (at equal rates under steady-state conditions), can be represented as a single bimolecular reaction 3a, b occurring in a "cage" of solvent molecules.

The free formyl radical resulting from reaction 4, which is in competition with reactions 3 and 3a, is comparatively low-reactive because its spin density can be partially delocalized from the carbon atom *via* the double bond toward the oxygen atom, which possesses a higher electron affinity.[1] For example, in contrast to the methyl and alkoxyl π-radicals, the formyl σ-radical can be stabilized in glassy alcohols at 77 K.[37] In gas phase, the dissociation energy of the C–H bond in formyl radicals is half that for acetyl radicals and is about 5 times lower than the dissociation energy of the C_α–H bond in saturated C_1–C_3 alcohols.[1]

As distinct from reactions 3 and 3a, b, reaction 4 leads to an inefficient consumption of hydroxyalkoxyl adduct radicals, without regenerating the initial 1-hydroxyalkyl addendum radicals. Reaction 4 together with reaction 6 (mutual annihilation of free formyl and chain-carrier 1-hydroxyalkyl radicals) causes the inhibition of the nonbranched-chain process. For the disproportionation of the free radicals, the heats of reactions 5-7 for C1–C3 alcohols in the gas phase vary in the range of ΔH°_{298} = –135 to –385 kJ mol^{-1}.[1-4]

The rates of the chain formation of 1,2-alkanediols in reaction 3 (and their nonchain formation in reaction 4), carbonyl compounds in reaction 3a, and methanol in reaction 3b are given by the following equations, where V_1 is the initiation rate, l is the molar concentration of the saturated alcohol at a given total concentration of formaldehyde dissolved in it, x is the molar concentration of free formaldehyde ($l >> x$), k_2 is the rate constant of reaction 2 (addition of 1-hydroxyalkyl free radical to free formaldehyde), and $\alpha = k_3/k_4$ and $\beta = k_{3a}/k_4$ (mol dm^{-3}) are the ratios of the rate constants of the competing (parallel) reactions. The alcohol concentration in alcohol–formaldehyde solutions at any temperature can be estimated by the method suggested in.[38,39] The data necessary for estimating the concentration of free formaldehyde using the total formaldehyde concentration in the solution are reported by Silaev *et al*.[28,29]

$$V_{3,4}(R_{(-H)}(OH)CH_2OH) = \frac{V_1(\alpha l + x)k_2 x}{k_2 x^2 + (\alpha l + \beta + x)\sqrt{2k_5 V_1}}, \quad (5)$$

$$V_{3a}(R_{(-2H)}HO) = V_{3b}(CH_3OH) = \frac{V_1 \beta\, k_2 x}{k_2 x^2 + (\alpha l + \beta + x)\sqrt{2k_5 V_1}}, \quad (6)$$

Estimates of $2k_5$ were reported by Silaev *et al*.[39,40] From the extremum condition for the reaction 3a rate function, $\partial V_{3a} / \partial x = 0$, we derived the following analytical expression: $k_2 = (\alpha l_m + \beta)\sqrt{2k_5 V_1} \big/ x_m^2$.

The overall process rate is a complicated function of the formation and disappearance rates of the $^{\bullet}R_{(-H)}OH$ and $^{\bullet}CHO$ free radicals: $V(R_{(-H)}(OH)CH_2OH, R_{(-2H)}HO, CH_3OH) = V_{1a} + V_3 + V_{3b} - V_4 - V_5 + V_7$. The ratios of the rates of the competing reactions are $V_3/V_4 = \alpha l/x$ and $V_{3a}/V_4 = \beta/x$, and the chain length is $\nu = (V_3 + V_{3a})/V_1$. The ratio of the rates of formation of 1,2-alkanediol and the carbonyl compound is a simple linear function of x:

$$V_{3,4}(R_{(-H)}(OH)CH_2OH)/V_{3a}(R_{(-2H)}HO)=(k_4/k_{3a})x + (k_3/k_{3a})l.$$

The equations for the rates of chain-termination reactions 5-7 are identical to eqns. (12)-(14).

Neutral formaldehyde solutions in alcohols at room temperature primarily consist of a mixture of formaldehyde polymer solvates reversibly bound to alcohols. These polymer solvates differ in molecular mass and have the general formula $RO(CH_2O)_nH$, where n=1-4.[27] The concentration of formaldehyde that occurs in solution as a free, unsolvated active species chemically unbound to the solvent (this species is capable of scavenging free radicals) at room temperature is lower than 1 % of the total formaldehyde concentration.[27] The concentration x of the free formaldehyde species in solutions was determined by high-temperature UV spectrophotometry in the range 335–438 K at the total formaldehyde concentration c_0 (free and bound species including the concentration of polymer solvates) of 1.08.4 mol dm^{-3} in water, ethanediol, methanol, ethanol, 1-propanol, 2-propanol, and 2-methyl-2-propanol[28] (see Table of the Appendix). This concentration increases with temperature according to an exponential law, and it can be as high as a few percent of the total concentration in solution under the test conditions, up to 19.3 % in the case of 2-methyl-2-propanol at a total concentration of 1.0 mol dm^{-3} and a temperature of 398 K. The following empirical equation relating the concentration x (mol dm^{-3}) of free formaldehyde to temperature T (K) and the total concentration c_0 in the solution (measured at room temperature), was developed by the treatment of 101 data points,[28,39] where the coefficients a and b were calculated as the parameters of a straight-line equation by the least-squares technique from the dependence of log x on $1/T$ at c_0 = 1.0 mol dm^{-3} for various solvents, and the coefficient h was obtained as the average value of the slopes of log x as linear functions of log c_0 at various series of fixed temperatures.

Table 1. Coefficients of eqn. (7) for the estimation of the concentration x of free formaldehyde in polar solvent–formaldehyde systems.

Solvent	Coefficient		
	a	***b***	***h***
Water	2.36	4.45	0.80
Ethanediol	1.83	2.60	1.28
Methanol	3.11	5.58	0.22 c_0 / log c_0
Ethanol	3.10	5.92	1.10 ($10^3/T$) – 1.44
1-Propanol	2.42	4.47	1.30
2-Propanol	2.42	4.64	1.05
2-Methyl-2-propanol	3.19	7.31	0.96

$$\log x = -a\,(10^3/T) + b + h \log c_0, \qquad (7)$$

The coefficients for each solvent are summarized in Table 1. As regards the experimental data, the error in the calculations of the concentration x of free formaldehyde made by eqn. (7) in the specified temperature range was no higher than 25 %.

On the assumption that the dependence of the density of a given solution on the concentration of formaldehyde is similar to the analogous linear dependence found for aqueous formaldehyde solutions (0-14 mol dm^{-3}, 291 K),[27] the concentrations l_T (mol dm^{-3}) of alcohols in alcohol–formaldehyde solutions at a certain temperature can be estimated by eqn. (8), where c_0 is the total formaldehyde concentration (mol dm^{-3}); M is the molecular mass (g mol^{-1}) of the solvent; d and d_T are the solvent densities (g cm^{-3}) at room and given temperatures, respectively; the coefficients 8.4×10^{-3} and 21.6 have the units of 10^3g mol^{-1} and g mol^{-1}, respectively.[38]

$$l_T = \frac{(10^3 d - 21.6\,c_0)d_T}{(d + 8.4\times10^{-3}\,c_0)M}, \qquad (8)$$

Earlier,[28] it was found that the concentration x of the free formaldehyde species decreased with the solvent permittivity D_{298} at a constant temperature. Water is an exception. Although water is more polar than alcohols, the concentration x of free formaldehyde in an aqueous solution is anomalously high and reaches the level of its concentration in 2-propanol, all other factors being the same (Figure 2).[28,39] This can be due to the specific instability of hydrated formaldehyde species and the ease of their conversion into free formaldehyde with increasing temperature.

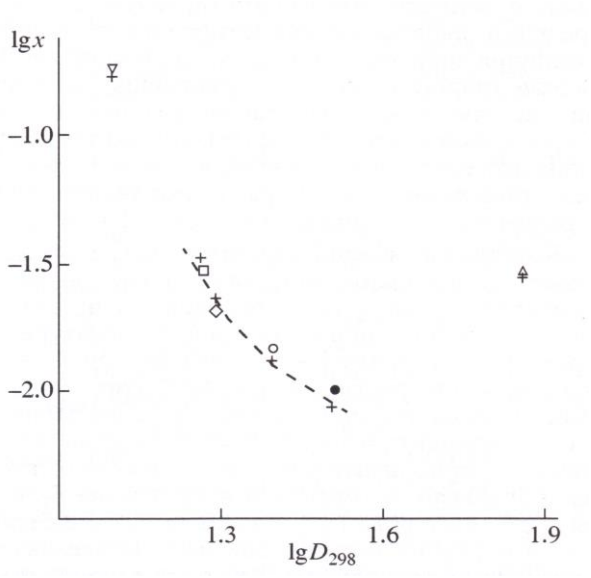

Figure 2. Logarithmic plot of the experimental concentrations x (mol dm^{-3}) of free formaldehyde at its total concentration c_0 = 1.0 mol dm^{-3} and 395 ± 3 K in (△) water, (●) methanol, (○) ethanol, (◇) 1-propanol, (□) 2-propanol, and (▽) 2-methyl-2-propanol as functions of the permittivity D_{298} of these solvents (+ refers to the concentrations x in the above solvents calculated by eqn. (8)).

Figure 3 illustrates the use of eqns. (5) and (6) for describing the experimental dependences of the formation rates of 1,2-butanediol (curve *1*) in reactions 3 and 4 and propanal (curve *2*) in reaction 3a on the concentration of

free formaldehyde in the 1-propanol–formaldehyde reacting system at a total formaldehyde concentration of 2.0 to 9.5 mol dm^{-3} and temperature of 413 K.[8,9,41] The concentration dependence of the propanal formation rate was described using the estimates of kinetic parameters obtained for the same dependence of the 1,2-butanediol formation rate. We considered these data more reliable for the reason that the carbonyl compounds forming in the alcohol–formaldehyde systems can react with the alcohol and this reaction depends considerably on the temperature and acidity of the medium.[27] The mathematical modelling of the process was carried out using a ^{137}Cs γ-radiation dose rate of P = 0.8 Gy s^{-1},[32,41] a total initiation yield[8,9] of $G(CH_3CH_2\dot{C}HOH)$ = 9.0 particles per 100 eV ($V_1 = 4.07 \times 10^{-7}$ mol dm^{-3} s^{-1}), and $2k_5 = 4.7 \times 10^9$ dm^3 mol^{-1} s^{-1}). The following values of the parameters were obtained: $\alpha = 0.36 \pm 0.07$, $\beta = 0.25 \pm 0.05$ mol dm^{-3}, and $k_2 = (6.0 \pm 1.4) \times 10^3$ dm^3 mol^{-1} s^{-1}.

It may be noted that, as compared to the yields of 1,2-propanediol in the γ-radiolysis of the ethanol–formaldehyde system, the yields of 2,3-butanediol in the γ-radiolysis of the ethanol–acetaldehyde system are one order of magnitude lower.[41] Using data from,[8,9] it can be demonstrated that, at 433 K, the double bond of 2-propen-1-ol accepts the 1-hydroxyethyl radical 3.4 times more efficiently than the double bond of formaldehyde.[42]

Addition of hydroxymethyl radicals

The addition of hydroxymethyl radicals to the carbon atom at the double bond of free formaldehyde molecules in methanol, initiated by the free-radical mechanism, results in the chain formation of ethanediol.[34] In this case, reaction 3a in Scheme 2 is the reverse of reaction 2, the 1-hydroxyalkyl radical $^{\bullet}R_{(-H)}OH$ is the hydroxymethyl radical $^{\bullet}CH_2OH$, so reaction 3b is eliminated (k_{3b} = 0), and reaction 5 yields an additional amount of ethanediol *via* the dimerization of chain-carrier hydroxymethyl radicals (their disproportionation can practically be ignored[43]). The scheme of these reactions has been reported.[35]

The rate equation for ethanediol formation by the chain mechanism in reaction 3 and by the nonchain mechanism in reactions 4 and 5 in the methanol–formaldehyde system has a complicated form as compared to eqn. (1) for the formation rate of the other 1,2-alkanediols.[12] In an earlier publication,[8] this equation does not take into account reaction 3a.

$$V_{3,\,4,\,5}(CH_2OH)_2 = V_1[\,f(\alpha l + x)k_2 x + V_1 2k_5(\alpha l + \beta + x)^2\,]\big/ f^2\,, \quad (9)$$

where $f = k_2x^2 + (\alpha l + \beta + x)\sqrt{2k_5V_1}$.

If the rate of ethanediol formation by dimerization in reaction 5 is ignored for the reason that it is small as compared to the total rate of ethanediol formation in reactions 3 and 4, eqn. (9) will be identical to eqn. (5). After the numerator and denominator on the right-hand side of eqn. (5) are divided by $k_{-2} \equiv k_{3a}$, one can replace k_2 in this equation with $K_2 = k_2/k_{-2}$, which is the equilibrium constant for the reverse of reaction 2. Ignoring the reverse of reaction 2 (k_{3a} = 0, β = 0) makes eqn. (5) identical to eqn. (4) for Scheme 1 at k_{3b} = 0. In this case, the rate constant k_2 is effective.

Addition to Oxygen

The addition of a free radical or an atom to one of the two multiply bonded atoms of the oxygen molecule yields a peroxyl free radical and thus initiates oxidation, which is the basic process of chemical evolution. The peroxyl free radical then abstracts the most labile atom from a molecule of the compound being oxidized or decomposes to turn into a molecule of an oxidation product. The only reaction that can compete with these two reactions at the chain evolution stage is the addition of the peroxyl radical to the oxygen molecule (provided that the oxygen concentration is sufficiently high). This reaction yields a secondary, tetraoxyalkyl, 1:2 adduct radical, which is the heaviest and the largest among the reactants. It is less reactive than the primary, 1:1 peroxyl adduct radical and, as a consequence, does not participate in further chain propagation. At moderate temperatures, the reaction proceeds *via* a nonbranched-chain mechanism.

Addition of hydrocarbon free radicals

Usually, the convex curve of the hydrocarbon (RH) autooxidation rate as a function of the partial pressure of oxygen ascends up to some limit and then flattens out.[6] When this is the case, the oxidation kinetics is satisfactorily describable in terms of the conventional reaction scheme,[2,5,6,16,44,45] which involves two types of free radicals. These are the hydrocarbon radical R$^{\bullet}$ (addend radical) and the addition product $RO_2^{\bullet}$ (1:1 adduct radical). However, the existing mechanisms are inapplicable to the cases in which the rate of initiated oxidation as a function of the oxygen concentration has a maximum (Figures. 4, 5).[46,47] Such dependences can be described in terms of the competition kinetics of free-radical chain addition, whose reaction scheme involves not only the above two types of free radicals, but also the $RO_4^{\bullet}$ radical (1:2 adduct) inhibiting the chain process.[13,14]

Chain initiation

1. $I \xrightarrow{2k_1} 2R_0^{\bullet}$;

1a. $R_0^{\bullet} + RH \xrightarrow{k_{1a}} R_0H + R^{\bullet}$.

Chain propagation

2. $R^{\bullet} + O_2 \xrightarrow{k_2} RO_2^{\bullet}$;

3. $RO_2^{\bullet} + RH \xrightarrow{k_3} RO_2H + R^{\bullet}$

(or ROH + RO$^{\bullet}$);

3a. $RO_2^{\bullet} \xrightarrow{k_{3a}} R'_{(-H)}HO + R''O^{\bullet}$

(or $R_{(-2H)}HO + {}^{\bullet}OH$);

3b. $R''O^{\bullet}(RO^{\bullet}) + RH \xrightarrow{k_{3b}} R''OH\ (ROH) + R^{\bullet}$

(or $^{\bullet}OH + RH \xrightarrow{k_{3b}} H_2O + R^{\bullet}$).

Inhibition

4. $RO_2^{\bullet} + O_2 \xrightarrow{k_4} RO_4^{\bullet}$.

Chain termination

5. $2R^{\bullet} \xrightarrow{2k_5} RR$

(or $R_{(-2H)}H + RH$);

6. $R^{\bullet} + RO_4^{\bullet} \xrightarrow{k_6} RH + R_{(-2H)}HO + O_3$

(or: $ROH + R_{(-2H)}HO + O_2$,

$ROR + O_3$, $RO_2R + O_2$);

7. $2\,RO_4^{\bullet} \xrightarrow{2k_7} RO_2R + 2O_3$.

Scheme 3. Kinetic model of oxidation.

The only difference between the kinetic model of oxidation represented by Scheme 3 and the kinetic model of the chain addition of 1-hydroxyalkyl radicals to the free (unsolvated) form of formaldehyde in nonmethanolic alcohol–formaldehyde systems[8,9] (Scheme 2) is that in the former does not include the formation of the molecular 1:1 adduct *via* reaction 4.

The decomposition of the initiator I in reaction 1 yields a reactive $R_0^{\bullet}$ radical, which turns into the ultimate product R_0H *via* reaction 1a, generating an alkyl radical $R^{\bullet}$, which participates in chain propagation. In reaction 2, the addition of the free radical $R^{\bullet}$ to the oxygen molecule yields a reactive alkylperoxyl 1:1 adduct radical $RO_2^{\bullet}$ [45] which possesses increased energy owing to the energy released upon the conversion of the O=O bond into the ordinary bond RO–O$^{\bullet}$ (for addition in the gas phase under standard conditions, this energy is 115-130 kJ mol^{-1} for C_1-C_4 alkyl radicals[1,2,4] and 73 kJ mol^{-1} for the allyl radical).[4] Because of this, the adduct radical can decompose (reaction 3a) or react with some neighboring molecule (reaction 3 or 4) on the spot, without diffusing in the solution and, accordingly, without entering into any chain termination reaction. In reaction 3, the interaction between the radical adduct $RO_2^{\bullet}$ and the hydrocarbon molecule RH yields, *via* a chain mechanism, the alkyl hydroperoxide RO_2H (this reaction regenerates the chain carrier $R^{\bullet}$ and, under certain conditions, can be viewed as being reversible[2]) or the alcohol ROH (this is followed by the regeneration of $R^{\bullet}$ *via* reaction 3b). The latter (alternative) pathway of reaction 3 consists of four steps, namely, the breaking of old bonds and the formation of two new bonds in the reacting structures. In reaction 3a, the isomerization and decomposition of the alkylperoxyl radical adduct $RO_2^{\bullet}$ with O–O and C–O or C–H bond breaking take place,[6,44] yielding the carbonyl compound $R'_{(-H)}HO$ or $R_{(-2H)}HO$. Reaction 3b produces the alcohol R″OH or water and regenerates the free radical $R^{\bullet}$ (here, R′ and R″ are radicals having a smaller number of carbon atoms than R). As follows from the above scheme of the process, consecutive reactions 3a and 3b (whose rates are equal within the quasi-steady-state treatment), in which the highly reactive fragment, oxyl radical R″O$^{\bullet}$ (or $^{\bullet}$OH) forms and then disappears, respectively, can be represented as a single, combined bimolecular reaction 3a, b occurring in a "cage" of solvent molecules. Likewise, the alternative (parenthesized) pathways of reactions 3 and 3b, which involve the alkoxyl radical RO$^{\bullet}$, can formally be treated as having equal rates. For simple alkyl C_1–C_4 radicals R, the pathway of reaction 3 leading to the alkyl hydroperoxide RO_2H is endothermic (ΔH°_{298} = 30-80 kJ mol^{-1}) and the alternative pathway yielding the alcohol ROH is exothermic (ΔH°_{298}= –120 to –190 kJ mol^{-1}), while the parallel reaction 3a, which yields a carbonyl compound and the alkoxyl radical R″O$^{\bullet}$ or the hydroxyl radical $^{\bullet}$OH, is exothermic in both cases (ΔH°_{298} = –80 to –130 kJ mol^{-1}), as also is reaction 3b (ΔH°_{298} = –10 to –120 kJ mol^{-1}), consecutive to reaction 3a, according to thermochemical data for the gas phase.[2-4] In reaction 4, which is competing with (parallel to) reactions 3 and 3a (chain propagation through the reactive radical $R^{\bullet}$), the resulting low-reactive radical that does not participate in further chain propagation and inhibits the chain process is supposed to be the alkyltetraoxyl 1:2 radical adduct $RO_4^{\bullet}$, which has the largest weight and size. It has been hypothesized that raising the oxygen concentration in the *o*-xylene–oxygen system can lead to the formation of the [RO$^{\bullet}\cdots O_2$] intermediate complex[46] similar to the [ROO$^{\bullet}\cdots$(π-bond)RH] complex between the alkylperoxyl 1:1 adduct radical and an unsaturated hydrocarbon suggested in this work. The electronic structure of the π-complexes is considered elsewhere.[48] Thermochemical data are available for some polyoxyl free radicals (the enthalpy of formation of the methyltetraoxyl radical without the energy of the possible intramolecular hydrogen bond H$\cdots$O taken into account is $\Delta H_f^{\circ}{}_{298}(CH_3O_4^{\bullet})$ = 121.3 ± 15.3 kJ mol^{-1}) and polyoxides ($\Delta H_f^{\circ}{}_{298}(CH_3O_4H)$ = –21.0 ± 9 kJ mol^{-1}).[49] These data were obtained using the group contribution approach. Some physicochemical and geometric parameters were calculated for the methyl hydrotetraoxide molecule as a model compound.[50-52] The IR spectra of dimethyl tetraoxide with isotopically labeled groups in Ar–O_2 matrices are also reported.[53] For reliable determination of the number of oxygen atoms in an oxygen-containing species, it is necessary to use IR and EPR spectroscopy in combination with the isotope tracer method.[53]

This radical is possibly stabilized by a weak intramolecular H$\cdots$O hydrogen bond[54] shaping it into a six-membered cyclic structure (seven-membered cyclic structure in the case of aromatic and certain branched acyclic hydrocarbons).[56,57]

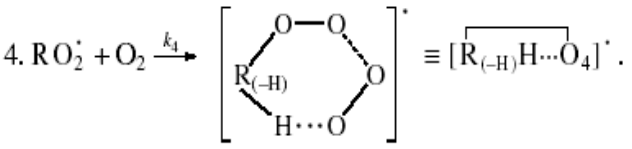

Scheme 3. Possible mechanism of reaction 4.

Note that the $\overline{R_{(-H)}H\cdots O(R)O_3}$ ring consisting of the same six atoms (C, H, and 4O), presumably with a hydrogen bond,[6] also forms in the transition state of the dimerization of primary and secondary alkylperoxyl radicals $RO_2^{\bullet}$ *via* the Russell mechanism.[5,55]

Reaction 4 in the case of the methylperoxyl radical $CH_3O_2^{\bullet}$, addition to the oxygen molecule to yield the methyltetraoxyl radical $CH_3O_4^{\bullet}$, takes place in the gas phase, with heat absorption equal to 110.0 ± 18.6 kJ mol^{-1} (without the energy of the possible formation of a hydrogen bond taken into account).[49] The exothermic reactions 6 and 7, in which the radical R$^{\bullet}$ or $RO_4^{\bullet}$ undergoes disproportionation, include the isomerization and decomposition of the $RO_4^{\bullet}$ radical (taking into account the principle of detailed balance for the various pathways of formation of products, whose numbers in the elementary reaction should not exceed three for possible involvement in the triple collisions in the case of the reverse reaction, since the probability of simultaneous interaction of four particles is negligible). The latter process is likely accompanied by chemiluminescence typical of hydrocarbon oxidation.[52] It may be noted that the alkylperoxyl radicals $RO_2^{\bullet}$ are effective quenchers of singlet oxygen $O_2(a^1\Delta_g)$.[58] These reactions regenerate oxygen as O_2 molecules, including singlet oxygen,[52,59] and partially, as O_3 molecules and yield the carbonyl compound $R_{(-2H)}HO$, possibly in the triplet excited state.[52] Depending on the decomposition pathway, the other possible products are alcohol ROH, ether ROR, and alkyl peroxide RO_2R. It is likely that the isomerization and decomposition of the $RO_4^{\bullet}$ radical *via* reactions 6 and 7 can take place through the breaking of a C–C bond to yield carbonyl compounds, alcohols, ethers, and organic peroxides containing fewer carbon atoms than the initial hydrocarbon, as in the case of the alkylperoxyl radical $RO_2^{\bullet}$ in reaction 3a. At later stages of oxidation and at sufficiently high temperatures, the resulting aldehydes can be further oxidized into respective carboxylic acids. They can also react with molecular oxygen so that a C–H bond in the aldehyde molecule breaks to yield two free radicals ($HO_2^{\bullet}$ and $^{\bullet}R'_{(-H)}O$ or $^{\bullet}R_{(-2H)}O$). This process, like possible ozone decomposition yielding an $^{\bullet}O^{\bullet}$ atom or peroxide decomposition with O–O bond breaking, leads to degenerate chain branching.[6]

The equations describing the rates of formation of molecular products at the chain propagation and termination stages of the above reaction scheme, using the quasi-steady-state treatment, appear as follows, where V_1 is the initiation rate, l = [RH] and x = [O_2] are the molar concentrations of the starting components ($l >> x$), $\alpha = k_3/k_4$ and $\beta = k_{3a}/k_4$ (mol dm^{-3}) are the ratios of the rate constants of the competing (parallel) reactions, $k_2 = (\alpha l_m + \beta)\sqrt{2k_5V_1}/x_m^2$ is the rate constant of the addition of the alkyl radical R$^{\bullet}$ to the oxygen molecule (reaction 2) as determined by solving the quadratic equation following from the rate function extremum condition $\partial V_{3,3a}/\partial x = 0$, l_m and x_m are the values of l and x at the maximum point of the function,

$f = k_2x^2 + (\alpha l + \beta + x)\sqrt{2k_5V_1}$, and $f_m = x^2 + (\alpha l + \beta + x)x_m^2/(\alpha l_m + \beta)$:

$$V_3(RO_2H;\ ROH) = V_1\alpha l k_2 x/f = \quad (10)$$

$$= V_1\alpha l x/f_m, \quad (10a)$$

$$V_{3a}(R'_{(-H)}HO;\ R_{(-2H)}HO) = V_{3b}(R''OH;\ H_2O) =$$

$$= V_1\beta\, k_2 x/f = \quad (11)$$

$$= V_1\beta\, x/f_m, \quad (11a)$$

$$V_5 = V_1^2 2k_5\left(\alpha l + \beta + x\right)^2/f^2, \quad (12)$$

$$2V_6 = 2V_1\sqrt{2k_5V_1}\left(\alpha l + \beta + x\right)k_2x^2/f^2, \quad (13)$$

$$V_7 = V_1\left(k_2x^2\right)^2/f^2, \quad (14)$$

The ratios of the rates of the competing reactions are $V_3/V_4 = \alpha l/x$ and $V_{3a}/V_4 = \beta/x$, and the chain length is $\nu = (V_3 + V_{3a})/V_1$. eqn. (11) is identical to eqn. (6). Eqns. (10a) and (10a) were obtained by replacing the rate constant k_2 in eqns. (10) and (11) with its analytical expression (for reducing the number of unknown parameters to be determined directly).

For $\alpha l >> \beta$ ($V_3 >> V_{3a}$), when the total yield of alkyl hydroperoxides and alcohols having the same number of carbon atoms as the initial compound far exceeds the yield of carbonyl compounds, as in the case of the oxidation of some hydrocarbons, the parameter β in eqns. (10) and (10a) can be neglected (β = 0) and these equations become identical to eqns. (3) and (3a) with the corresponding analytical expression for k_2.

In the alternative kinetic model of oxidation, whose chain termination stage involves, in place of R$^{\bullet}$ (Scheme 4), $RO_2^{\bullet}$ radicals reacting with one another and with $RO_4^{\bullet}$ radicals, the dependences of the chain formation rates of the products on the oxygen concentration x derived by the same method have no maximum: $V_3 = V_1k_3l/(k_4x + \sqrt{2k_5V_1})$ and $V_{3a} = V_1k_{3a}/(k_4x + \sqrt{2k_5V_1})$. In the kinetic model of oxidation that does not include the competing reaction 4 (k_4 = 0) and involves the radicals R$^{\bullet}$ and $RO_2^{\bullet}$ (the latter instead of $RO_4^{\bullet}$ in Scheme *3*) in reactions 5–7, the reaction rate functions V_3 and V_{3a} obtained in the same way are fractional rational functions in the form of $a_0x/(b_0x + c_0)$, where a_0, b_0, and c_0 are coefficients having no extremum. For a similar kinetic model in which reactions 3a, b and 4 appearing in the above scheme are missing ($k_{3a} = k_4 = 0$), Walling,[5] using the quasi-steady-state treatment in the long kinetic chain approximation, when it can be assumed that $V_2 = V_3$, without using the substitution[5,6,16] $k_6 = \sqrt{2k_5 2k_7}$ (as distinct from this work), found that $V_2 = V_3$ is an irrational function of x: $a_1x/\sqrt{b_1x^2 + c_1x + d_1}$ where a_1, b_1, c_1, and d_1 are coefficients. Again, this function has no maximum with respect to the concentration of any of the two components.

Thus, of the three kinetic models of oxidation mathematically analyzed above, which involve the radicals $R^{\bullet}$ and $RO_2^{\bullet}$ in three types of quadratic-law chain termination reactions (reactions 5-7) and are variants of the conventional model,[2,5,6,16,44,45] the last two lead to an oxidation rate versus oxygen concentration curve that emanates from the origin of coordinates, is convex upward and has an asymptote parallel to the abscissa axis. Such monotonic dependences are observed when the oxygen solubility in the liquid is limited under given experimental conditions and the oxygen concentration attained is $[O_2]_{top} \leq x_m$. The oxygen concentration attained in the liquid may be below the thermodynamically equilibrium oxygen concentration because of diffusion limitations hampering the establishment of the gas–liquid saturated solution equilibrium under given experimental conditions (for example, when the gas is bubbled through the liquid) or because the Henry law is violated for the given gas–liquid system under real conditions.

Unlike the conventional model, the above kinetic model of free-radical nonbranched-chain oxidation, which includes the pairs of competing reactions 3-4 and 3a-4 (Scheme 4), allows us to describe the nonmonotonic (peaking) dependence of the oxidation rate on the oxygen concentration (Figure 4).

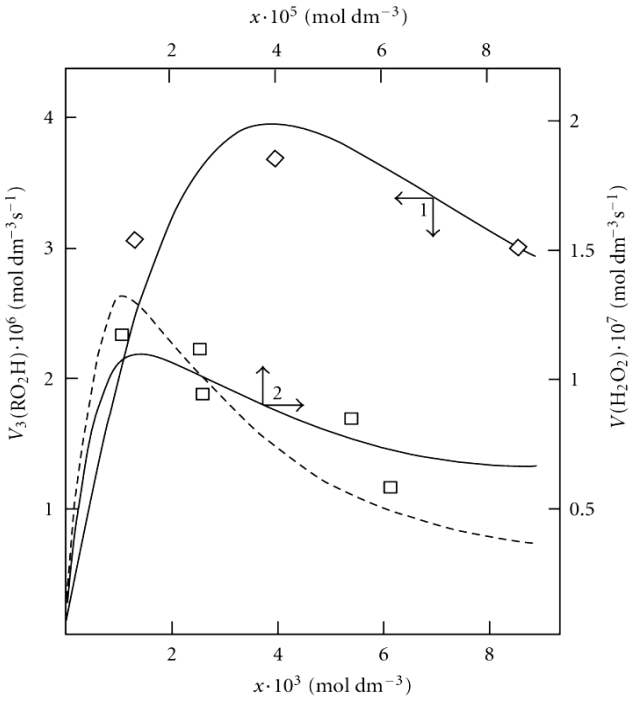

Figure 4. (*1*, ◇) Reconstruction of the functional dependence of the 2-methylbenzyl hydroperoxide formation rate $V_3(RO_2H)$ on the dissolved oxygen concentration *x*. (*2*, □) Reconstruction of the functional dependence of the total hydrogen peroxide formation rate $V_{3,\gamma}(H_2O_2)$ on the dissolved oxygen concentration *x* from empirical data (symbols) using eqns. (3a) and (14a) with $\beta = 0$ (model optimization with respect to the parameter α) for the γ-radiolysis of water saturated with hydrogen and containing different amounts of oxygen at 296 K[63] ($S_Y = 1.13 \times 10^{-8}$). The dashed curve described $V_3(H_2O_2)$ as a function of the oxygen concentration *x* based on eqn. (3a) (model optimization with respect to α) and the experimental data of curve *2* ($S_Y = 1.73 \times 10^{-8}$).

In this oxidation model, as the oxygen concentration in the binary system is increased, oxygen begins to act as an oxidation autoinhibitor or an antioxidant *via* the further oxidation of the alkylperoxyl 1:1 adduct radical $RO_2^{\bullet}$ into the low-reactive 1:2 adduct radical $RO_4^{\bullet}$ (reactions 4 and 6 lead to inefficient consumption of the free radicals $RO_2^{\bullet}$ and $R^{\bullet}$ and cause shortening of the kinetic chains).

The optimum oxygen concentration x_m, at which the oxidation rate is the highest, can be calculated using kinetic equations (10a) and (11a) and eqn. (3a) with $\beta = 0$ or the corresponding analytical expression for k_2. Semenov[60] has noted that raising the oxygen concentration when it is already sufficient usually slows down the oxidation process by shortening the chains. The existence of the upper (second) ignition limit in oxidation is due to chain termination in the bulk through termolecular collisions between an active species of the chain reaction and two oxygen molecules (at sufficiently high oxygen partial pressures). In the gas phase at atmospheric pressure, the number of termolecular collisions is roughly estimated to be 10^3 times smaller than the number of binary collisions and the probability of a reaction taking place depends on the specificity of the action of the third particle.[60] In case of a gas-phase oxidation of hydrogen at low pressures of 25-77 Pa and a temperature of 77 K[47] when termolecular collisions are unlikely, the dependence of the rate of formation of hydrogen peroxide on oxygen concentration also has a pronounced maximum (see curves 3 and 4 in figure 5) that indicates a chemical mechanism providing the appearance of a maximum (see reaction 4 of Scheme 3).

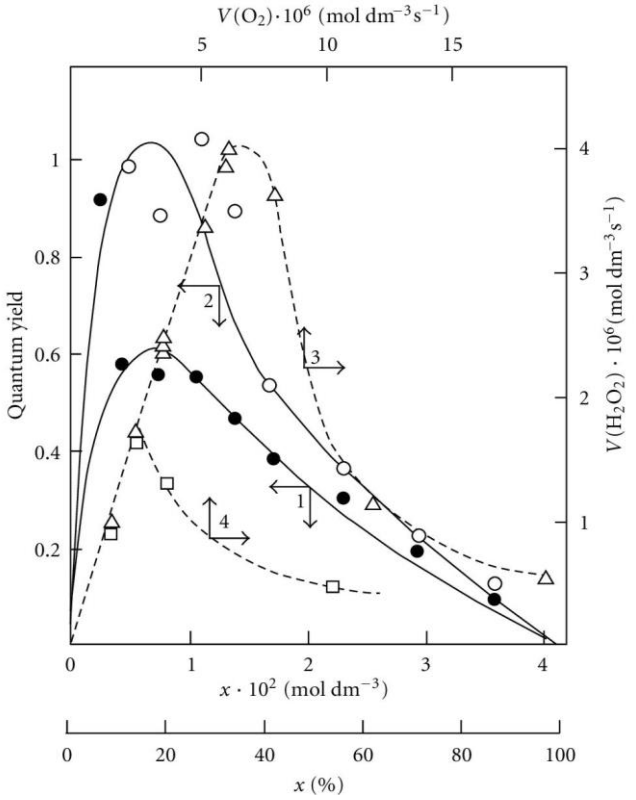

Figure 5. (1, 2) Quantum yields of (1, ●) hydrogen peroxide and (2, ○) water resulting from the photochemical oxidation of hydrogen in the hydrogen–oxygen system as a function of the oxygen concentration *x* (light wavelength of 171.9-172.5 nm, total pressure of 10^5 Pa, room temperature[64]). (3, 4) Hydrogen peroxide formation rate $V(H_2O_2)$ (dashed curves) as a function of the rate $V(O_2)$ at which molecular oxygen is passed through a gas-discharge tube filled with (3, △) atomic and (4, □) molecular hydrogen. The symbols represent experimental data.

Curve *1* in figure 4 illustrates the fit between eqn. (3a) at $\alpha l >> \beta$ and experimental data for the radiation-induced oxidation of *o*-xylene in the liquid phase at 373 K where 2-methylbenzyl hydroperoxide is formed much more rapidly than *o*-tolualdehyde ($V_3 >> V_{3a}$ and $\alpha l >> \beta$).[46] The oxygen concentration limit in *o*-xylene is reached at an oxygen concentration of $[O_2]_{top} > x_m$, which corresponds to the third experimental point.[46]

The oxygen concentration was calculated from the oxygen solubility in liquid xylene at 373 K.[61]

The following quantities were used in this mathematical description, ^{60}Co γ-radiation dose rate of $P = 2.18$ Gy s^{-1} and total initiation yield of $G(o\text{-}CH_3C_6H_4\dot{C}H_2) = 2.6$ particles per 100 eV of the energy absorbed by the solution;[46] $V_1 = 4.73 \times 10^{-7}$ mol dm^{-3} s^{-1} and $2k_5 = 1.15 \times 10^{10}$ dm^3 mol^{-1} s^{-1}. The resulting value of the parameter α is $(9.0 \pm 1.8) \times 10^{-3}$; hence, $k_2 = (3.2 \pm 0.8) \times 10^5$ dm^3 mol^{-1} s^{-1}. From the earlier data,[62] it was estimated that $k_4 = k_3/\alpha = (5.2 \pm 1.2) \times 10^2$ dm^3 mol^{-1} s^{-1}.

Addition of the hydrogen atom

A number of experimental findings concerning the autoinhibiting effect of an increasing oxygen concentration at modest temperatures on the oxidation of hydrogen both in the liquid phase[63] (Figure 4, curve 2) and in the gas phase[47,64,65] (Figure 5), considered in our earlier work,[13,56,57,66] can also be explained in terms of the competition kinetics of free radical addition.[14,67] From Figure 5 it is apparent that the quantum yields of hydrogen peroxide and water (products of photochemical oxidation of hydrogen at atmospheric pressure and room temperature) are maximum in the region of small concentrations of oxygen in the hydrogen–oxygen system (curves *1* and 2, respectively).[64]

Nonbranched-chain oxidation of hydrogen and changes in enthalpy (ΔH°_{298}, kJ mol^{-1}) for elementary reactions are given in the following reaction Scheme 4.

Chain initiation

1. $H_2 \xrightarrow{h\nu,\gamma} 2H^\bullet$, $\Delta H^\circ_{298} = 436.0 \pm 0.0$.

Chain propagation

2. $H^\bullet + O_2 \xrightarrow{k_2} HO_2^\bullet$, $\Delta H^\circ_{298} = -205.4 \pm 1.7$;

3. $HO_2^\bullet + H_2 \xrightarrow{k_3} H_2O + HO^\bullet$, $\Delta H^\circ_{298} = -215.4 \pm 2.9$

(or $H_2O_2 + H^\bullet$), $\Delta H^\circ_{298} = 69.4 \pm 1.7$;

3′. $HO^\bullet + H_2 \xrightarrow{k_{3'}} H_2O + H^\bullet$, $\Delta H^\circ_{298} = -62.8 \pm 1.2$.

Inhibition

4. $HO_2^\bullet + O_2 \xrightarrow{k_4} HO_4^\bullet$, $\Delta H^\circ_{298} = 110.0 \pm 15.4$.

Chain termination

5. $2H^\bullet(+M) \xrightarrow{2k_5} H_2(+M)$, $\Delta H^\circ_{298} = -436.0 \pm 0.0$;

6. $H^\bullet + HO_4^\bullet \xrightarrow{k_6} H_2O_2 + O_2$, $\Delta H^\circ_{298} = -476.6 \pm 13.7$

(or: $H_2O + O_3$, $\Delta H^\circ_{298} = -439.3 \pm 15.4$,

$H_2 + 2O_2$), $\Delta H^\circ_{298} = -340.6 \pm 13.7$;

7. $2\,HO_4^\bullet \xrightarrow{2k_7} H_2O_2 + 2O_3$, $\Delta H^\circ_{298} = -95.0 \pm 30.8$.

Scheme 4. Nonbranched-chain oxidation of hydrogen.

Calculations for the $HO_4^\bullet$ radical with a helical structure were carried out using the G2(MP2) method.[68] The stabilization energies of $HO_2^\bullet$, $HO_4^\bullet$, and $HO_3^\bullet$ were calculated in the same work to be 64.5 ± 0.1, 69.5 ± 0.8, and 88.5 ± 0.8 kJ mol^{-1}, respectively. The types of the O_4 molecular dimers, their IR spectra, and higher oxygen oligomers were reported.[69,70] The structure and IR spectrum of the hypothetical cyclotetraoxygen molecule O_4, a species with a high- energy density, were calculated by the CCSD method, and its enthalpy of formation was estimated.[71] The photochemical properties of O_4 and the van der Waals nature of the O_2-O_2 bond have investigated [72,73].[72,73] The most stable geometry of the dimer is two O_2 molecules parallel to one another. The O_4 molecule was identified by NR mass spectrometry.[74]

The hydroperoxyl free radical $HO_2^\bullet$, resulting from reaction 2, possesses an increased energy due to the energy released on the conversion of the O=O multiple bond into the HO–O$^\bullet$ ordinary bond.[75-78] Therefore, before its possible decomposition, it can interact with a hydrogen or oxygen molecule as the third body *via* parallel (competing) reactions 3 and 4, respectively. The hydroxyl radical HO$^\bullet$ that appears and disappears in consecutive parallel reactions 3 (first variant) and 3′ possesses additional energy owing to the exothermicity of the first variant of reaction 3, whose heat is distributed between the two products. As a consequence, this radical has a sufficiently high reactivity not to accumulate in the system during these reactions, whose rates are equal ($V_3 = V_{3'}$) under quasi-steady-state conditions, according to the above scheme. Parallel reactions 3 (second, parenthesized variant) and 3′ regenerate hydrogen atoms. It is assumed[56.57] [56,57] that the hydrotetraoxyl radical,[79,80] $HO_4^\bullet$ resulting from endothermic reaction 4, which is responsible for the peak in the experimental rate curve (Figure 4, curve *2*), is a five-membered $[\overline{OO—H\cdots OO}]^\bullet$ cycle due to weak intramolecular hydrogen bonding.[54,81] This structure imparts additional stability to this radical and makes it least reactive.

The $HO_4^\bullet$ radical was discovered by Staehelin et al.[82] in a pulsed radiolysis study of ozone degradation in water. Its UV spectrum with an absorption maximum at 260 nm ($\varepsilon(HO_4^\bullet)_{280\ nm} = 320 \pm 15$ m^2 mol^{-1}) was reported. The spectrum of the $HO_4^\bullet$ radical is similar to that of ozone, but the molar absorption coefficient $\varepsilon(HO_4^\bullet)_{\lambda_{max}}$ of the former is almost two times larger.[82]

The assumption about the cyclic structure of the $HO_4^{\bullet}$ radical may be due to its mean lifetime in water at 294 K, which is $3.6 \pm 0.4 \times 10^{-5}$ s, as estimated[66] from the value of $1/k$ for the reaction[82] $HO_4^{\bullet} \xrightarrow{k} HO_2^{\bullet} + O_2$, is 3.9 times longer than that of the linear $HO_3^{\bullet}$ radical[68,83] estimated in the same way[66] for the same conditions,[84] $9.1 \pm 0.9 \times 10^{-6}$ s. MP2/6-311++G** calculations using the Gaussian-98 program confirmed that the cyclic structure[85] of $HO_4^{\bullet}$ is energetically more favorable than the helical structure.[68] The difference in energy is 4.8–7.3 kJ mol^{-1}, depending on the computational method and the basis set.[86] For example, with the MP2(full)/6-31G(d) method, the difference between the full energies of the cyclic and acyclic $HO_4^{\bullet}$ conformers with their zero-point energies (ZPE) values taken into account (which reduces the energy difference by 1.1 kJ mol^{-1}) is –5.1 kJ mol^{-1} and the entropy of the acyclic-to-cyclic $HO_4^{\bullet}$ transition is ΔS°_{298} = –1.6 kJ mol^{-1} K^{-1}. Therefore, under standard conditions, $HO_4^{\bullet}$ can exist in both forms, but the cyclic structure is obviously dominant (87 %, K_{eq} = 6.5).[85]

Reaction 4 and, to a much lesser degree, reaction 6 inhibit the chain process, because they lead to inefficient consumption of its main participants – $HO_2^{\bullet}$ and H$^{\bullet}$.

The hydrogen molecule that results from reaction 5 in the gas bulk possesses an excess energy, and, to acquire stability within the approximation used in this work, it should have time for deactivation via collision with a particle M capable of accepting the excess energy.[87] To simplify the form of the kinetic equations, it was assumed that the rate of the bimolecular deactivation of the molecule substantially exceeds the rate of its monomolecular decomposition, which is the reverse of reaction 5.[2]

Reactions 6 and 7 (taking into account the principle of detailed balance for the various pathways) regenerate hydrogen and oxygen (in the form of $O_2(X^3\Sigma_g^-)$ molecules, including the singlet states[49,70] with $\Delta H^{\circ}_{f\,298}(O_2, a^1\Delta_g)$ = 94.3 kJ mol^{-1} and $\Delta H^{\circ}_{f\,298}(O_2, b^1\Sigma_g^+)$ = 161.4 kJ mol^{-1}, which are deactivated by collisions, and in the form of O_3) and yield hydrogen peroxide or water via a nonchain mechanism, presumably through the formation of an unstable intermediate hydrogen tetraoxide molecule H_2O_4.[88] The energy of planar, six-atom, cyclic, hydrogen-bonded dimer $(HO_2^{\bullet})_2$ was calculated using B3LYP DFT.[88] The hydrogen bond energy is 47.7 and 49.4 kJ mol^{-1} at 298 K for the triplet and singlet states of the dimer, respectively. Ozone does not interact with molecular hydrogen. At moderate temperatures, it decomposes fairly slowly, particularly in the presence of $O_2(X^3\Sigma_g^-)$ [70].[70] The reaction of ozone with H$^{\bullet}$ atoms, which is not impossible, results in their replacement with HO$^{\bullet}$ radicals. The relative contributions from reactions 6 and 7 to the process kinetics can be roughly estimated from the corresponding enthalpy increments (Scheme 4).

When there is no excess hydrogen in the hydrogen–oxygen system and the homomolecular dimer O_4,[71-74,89,90] which exists at low concentrations (depending on the pressure and temperature) in equilibrium with O_2,[70] can directly capture the H$^{\bullet}$ atom to yield the heteronuclear cluster $HO_4^{\bullet}$,which is more stable than O_4 and cannot abstract a hydrogen atom from the hydrogen molecule,[70] nonchain hydrogen oxidation will occur to give molecular oxidation products *via* the disproportionation of free radicals. It may be mentioned that it is impossible to make a sharp distinction between the two-step bimolecular interaction of three species *via* the equilibrium formation of the labile intermediate O_4 and the elementary trimolecular reaction $O_2 + O_2 + H^{\bullet} \rightarrow HO_4^{\bullet}$.

The low-reactive hydrotetraoxyl radical $HO_4^{\bullet}$,[82] which presumably has a high-energy density,[71] may be an intermediate in the efficient absorption and conversion of biologically hazardous UV radiation energy in the upper atmosphere of the earth. The potential energy surface for the atmospheric reaction HO$^{\bullet}$ + O_3, in which the adduct $HO_4^{\bullet}(^2A)$ was considered as an intermediate, was calculated by the DMBE method.[91] From this standpoint, the following reactions[80,82,90,91] are possible in the upper troposphere, as well as in the lower and middle stratosphere, where most of the ozone layer is situated (altitude of 1630 km, temperature of 217–227 K, pressure of 1.0×10^4–1.2×10^3 Pa,[92] the corresponding ΔH°_{298} reaction values[49] are given in kJ mol^{-1}.

8. $H_2O(\text{vapor}) + h\nu \rightarrow H^{\bullet} + HO^{\bullet}$

9. $HO^{\bullet} + O_3 \rightarrow HO_4^{\bullet}$ ΔH°_{298} = –59.5;

10. $HO_4^{\bullet} \rightarrow HO_2^{\bullet} + O_2(X^3\Sigma_g^-)$ ΔH°_{298} = –110.0

(or $HO_2^{\bullet} + O_2(a^1\Delta_g)$ ΔH°_{298} = –15.7

The $HO_4^{\bullet}$ radical can disappear *via* disproportionation with a molecule, free radical, or atom in addition to dissociation. Emission from $O_2(a^1\Delta_g)$ and $O_2(b^1\Sigma_g^+)$ is observed at altitudes of 30-80 and 40-130 km, respectively.[93]

Staehelin et al.[82] pointed out that, in natural systems in which the concentrations of intermediates are often very low, kinetic chains in chain reactions can be very long in the absence of scavengers since the rates of the chain termination reactions decrease with decreasing concentrations of the intermediates according to a quadratic law, whereas the rates of the chain propagation reactions decrease according to a linear law.

The kinetic description of the noncatalytic oxidation of hydrogen, including in an inert medium,[87] in terms of the simplified scheme of free-radical nonbranched-chain reactions (Scheme 4), which considers only quadratic-law chain termination and ignores the surface effects,[47] at moderate temperatures and pressures, in the absence of transitions to unsteady-state critical regimes, and at a substantial excess of the hydrogen concentration over the oxygen concentration was obtained by means of quasi-steady-state treatment, as in the previous studies on the kinetics of the branched-chain free-radical oxidation of hydrogen,[76] even though the applicability of this method in the latter case under unsteady states conditions was insufficiently substantiated. The method was used with the condition that $k_6 = \sqrt{2k_5 2k_7}$ (see Introduction). For example,

the ratio of the rate constants of the bimolecular disproportionation and dimerization of free radicals at room temperature is $k(HO^{\bullet} + HO_2^{\bullet})/[2k(2HO^{\bullet})2k(2HO_2^{\bullet})]^{0.5} = 2.8$ in the atmosphere[92] and $k(H^{\bullet} + HO^{\bullet})/ [2k(2H^{\bullet})2k(2HO^{\bullet})]^{0.5} = 1.5$ in water.[94] These values that are fairly close to unity.

The equation for the rate of the chain formation of hydrogen peroxide and water, $V_3(H_2O_2; H_2O) = V_{3'}(H_2O)$, *via* reactions 3 and 3′ is identical to eqn. (3, 3a) with the corresponding analytical expression for k_2. The ratio of the rates of the competing reactions is $V_3/V_4 = \alpha l/x$, and the chain length is $\nu = V_3/V_1$. The rates of nonchain formation of hydrogen peroxide and water *via* reactions (6) and (7), the quadratic-law chain termination, are identical to eqns. (13) and (14) provided that $\beta = 0$. In these equations, l and x are the molar concentrations of hydrogen and oxygen ($l >> x$), l_m and x_m are the respective concentrations at the maximum point of the function, V_1 is the rate of initiation (reaction 1), $\alpha = k_3/k_4$, the rate constant $k_2 = \alpha l_m \sqrt{2k_5V_1}\,/x_m^2$ is derived from the condition $\partial V_3/\partial x = 0$, and $2k_5$ is the rate constant of reaction 5 (hydrogen atom recombination), which is considered as bimolecular within the given approximation. This rate constant in the case of the pulsed radiolysis of ammonia–oxygen (+ argon) gaseous mixtures at a total pressure of 10^5 Pa and a temperature of 349 K was calculated[65] to be 1.6×10^8 dm^3 mol^{-1} s^{-1} (a similar value of this constant for the gas phase was reported in an earlier publication[95]). Pagsberg *et al*.[65] found that the dependence of the yield of the intermediate HO$^{\bullet}$ on the oxygen concentration has a maximum close to 5×10^{-4} mol dm^{-3}. In the computer simulation of the process, they considered the strongly exothermic reaction $HO_2^{\bullet} + NH_3 \rightarrow H_2O + {}^{\bullet}NHOH$, which is similar to reaction 3 in Scheme 4, whereas the competing reaction 4 was not taken into account.

In the case of nonchain hydrogen oxidation *via* the above addition reaction ($H^{\bullet} + O_4 \xrightarrow{k_{add}} HO_4^{\bullet}$), the formation rates of the molecular oxidation products in reactions 6 and 7 (Scheme 4, $k_2 = k_3 = k_4 = 0$) are defined by modified eqns. (13) and (14) in which $\beta = 0$, ($\alpha l + x$) is replaced with 1, and k_2 is replaced with $k_{add}K_{eq}$ ($k_{add}K_{eq}$ is the effective rate constant of H$^{\bullet}$ addition to the O_4 dimer, $K_{eq} = k/k'$ is the equilibrium constant of the reversible reaction $2O_2 \underset{k'}{\overset{k}{\Leftrightarrow}} O_4$ with $k' >> k_{add}[H^{\bullet}]$). The formation rates of the stable products of nonchain oxidation ($k_3 = 0$), provided that either reactions (2) and (4) or reaction (2) alone ($k_4 = 0$) occurs (Scheme 4, in the latter case, reactions 6 and 7 involve the $HO_2^{\bullet}$ radical rather than $HO_4^{\bullet}$), are given by modified eqns. (13) and (14) with $\beta = 0$, ($\alpha l + x$) replaced with 1, and x^2 replaced with x.

If in Scheme 4 chain initiation *via* reaction 1 is due to the interaction between molecular hydrogen and molecular oxygen yielding the hydroxyl radical HO$^{\bullet}$ instead of H$^{\bullet}$ atoms and if this radical reacts with an oxygen molecule (reaction 4) to form the hydrotrioxyl radical $HO_3^{\bullet}$ (which was obtained in the gas phase by neutralization reionization (NR) mass spectrometry[83] and has a lifetime of $>10^{-6}$ s at 298 K) and chain termination takes place *via* reactions 5-7 involving the HO$^{\bullet}$ and $HO_3^{\bullet}$, radicals instead of H$^{\bullet}$ and $HO_4^{\bullet}$, respectively, the expressions for the water chain formation rates derived in the same way will appear as a rational function of the oxygen concentration x without a maximum: $V_{3'}(H_2O) = V_1k_{3'}l/(k_4x + \sqrt{2k_5V_1})$.

Curve *2* in Figure 4 describes, in terms of the overall equation $V_{3,7} = V_1x(\alpha l f_m + x^3)/f_m^2$ for the rates of reactions 3 and 7 (which was derived[96] from eqns. 3a and 14, respectively, the latter in the form of $V_7 = V_1x^4/f_m^2$ (14a) in which k_2 is replaced with its analytical expression derived from eqn. (10) with $\beta = 0$ everywhere), the dependence of the hydrogen peroxide formation rate (minus the rate $V_{H_2O_2} = 5.19 \times 10^{-8}$ mol dm^{-3} s^{-1} of the primary formation of hydrogen peroxide after completion of the reactions in spurs) on the concentration of dissolved oxygen during the γ-radiolysis of water saturated with hydrogen (at the initial concentration 7×10^{-4} mol dm^{-3}) at 296 K.[63] These data were calculated in the present work from the initial slopes of hydrogen peroxide buildup versus dose curves for a ^{60}Co γ-radiation dose rate of $P = 0.67$ Gy s^{-1} and absorbed doses of $D \cong 22.5$–304.0 Gy. The following values of the primary radiation-chemical yield G (species per 100 eV of energy absorbed) for water γ-radiolysis products in the bulk of solution at pH 4-9 and room temperature were used (taking into account that $V = GP$ and $V_1 = G_HP$): $G_{H_2O_2} = 0.75$ and $G_H = 0.6$ (initiation yield; see below),[94] $V_1 = 4.15 \times 10^{-8}$ mol dm^{-3} s^{-1} and $2k_5 = 2.0 \times 10^{10}$ dm^3 mol^{-1} s^{-1}.[94]

As that is apparent from Figure 4, the best description of the data with an increase in the oxygen concentration in water is attained when the rate V_7 of the formation of hydrogen peroxide *via* the nonchain mechanism in the chain termination reaction 7 (curve *1*, $\alpha = (8.5 \pm 2) \times 10^{-2}$) is taken into account in addition to the rate V_3 of the chain formation of this product *via* the propagation reaction 3 (dashed curve 2, $\alpha = 0.11 \pm 0.026$). The rate constant, $k_2 = 1.34 \times 10^7$, of addition reaction 2 determined from α is substantially lower than 2.0×10^{10} dm^3 mol^{-1} s^{-1} estimated earlier.[94] The difference can be due to the fact that the radiation-chemical specifics of the process were not considered in the kinetic description of the experimental data. These include oxygen consumption *via* reactions that are not involved in the hydrogen oxidation scheme[66,97,98] and reverse reactions resulting in the decomposition of hydrogen peroxide by intermediate products of water radiolysis (e_{aq}^-, H$^{\bullet}$, HO$^{\bullet}$), with the major role played by the hydrated electron.[94]

General scheme of the addition of free radicals to molecules of alkenes, formaldehyde, and oxygen

The general scheme of the nonbranched-chain addition of a free radical from a saturated compound to an alkene (and its functionalized derivative), formaldehyde, or dioxygen (which can add an unsaturated radical as well) in liquid homogeneous binary systems of these components includes the following reactions (Scheme 5).[57,97,09]

Initiation

1. $I \xrightarrow{2k_1} 2R_0^{\bullet}$;

1a. $R_0^{\bullet} + R_1A \xrightarrow{k_{1a}} R_0A + R_1^{\bullet}$

for addition to an alkene at comparable component concentrations,

1b. $R_0^{\bullet} + R_2B \xrightarrow{k_{1b}} R_0B + R_2^{\bullet}$

Chain propagation

2. $R_1^{\bullet} + R_2B \xrightarrow{k_2} R_3^{\bullet}$

3. $R_3^{\bullet} + R_1A \xrightarrow{k_3} R_3A + R_1^{\bullet}$

for addition to O_2 and the 1-hydroxyalkyl radical to CH_2O,

3a. $R_3^{\bullet} \xrightarrow{k_{3a}} R'R''CO + R_4^{\bullet}$

3b. $R_4^{\bullet} + R_1A \xrightarrow{k_{3b}} R_4A + R_1^{\bullet}$

Inhibition

For addition to an alkene or CH_2O,

4. $R_3^{\bullet} + R_2B \xrightarrow{k_4} R_3B + R_2^{\bullet}$

for addition to O_2,

4a. $R_3^{\bullet} + R_2B \xrightarrow{k_{4a}} R_{2a}^{\bullet}$

Chain termination

5. $2R_1^{\bullet} \xrightarrow{2k_5} Prod$

6. $R_1^{\bullet} + R_{2(2a)}^{\bullet} \xrightarrow{k_6} Prod$

7. $2R_{2(2a)}^{\bullet} \xrightarrow{2k_7} Prod$

Scheme 5. General scheme of addition of free radicals to molecules of alkenes, formaldehyde, and oxygen.

In this scheme, I is the initiator, for example, a peroxide;[5,17,18,29,30] $R_0^{\bullet}$ is any reactive radical (initiator); A is an atom of hydrogen[2,5,6,17,18,22-24,29-31] or halogen;[2,519-21] B is an atom of hydrogen,[5,17-21,23,24,29-32] halogen,[22] or oxygen[2,5,6.16,44-46] (in oxidation); $R_1^{\bullet}$ is a radical such as $^{\bullet}PCl_2$,[19] $^{\bullet}CCl_3$,[20] an alkyl,[2,5,6,21] a 1-hydroxyalkyl,[5,6,17,22-24,29,32] or a similar functionalized radical addendum;[5] $R_2^{\bullet}$ is the formyl,[8,9,29] propenyl or higher alkenyl,[2,5,17-22] a 1-hydroxyalkenyl,[5,17,18,23,24] or a similar functionalized low-reactive radical inhibitor[5,18] or the oxygen atom (in oxidation);[2,5,6,13,14,16,44-46,56,57,96-98] $R_{2a}^{\bullet}$ is the low-reactive alkyltetraoxyl 1:2 adduct inhibitor radical $RO_4^{\bullet}$;[13,14,56,57,96-98] $R_3^{\bullet}$ is the active 1:1 adduct radical; $R_4^{\bullet}$ is an active fragment radical, such as hydroxymethyl,[8,9,12,29,32] an alkoxyl radical, or hydroxyl (in oxidation);[2,5,6,13,14,16,44,46,56,57,96-98] R_0A, R_0B, R_1A, and R_4A are saturated molecules; R_2B is an unsaturated molecule, *viz.*, an alkene,[2,5,11,17-22] formaldehyde [8,9,12,29–32], or dioxygen (in oxidation);[2,5,6,13,14,16,44-46,56,57,96-98] R′R″CO is a carbonyl compound *viz.*, aldehyde[2,6,8,9,12,14,29-32,44] or ketone;[2,6,14,29,32,44] R_3A and R_3B are molecular products (1:1 adducts), and Prod stands for molecular products of the dimerization and disproportionation of free radicals.

The chain evolution stage of Scheme 5 includes consecutive reactions 2, 3; 2, 3a; and 3a, 3b; parallel (competitive) reactions 3, 3a; 3, 3b; 3, 4 (or 4a); and 3a, 4 (or 4a); and consecutive-parallel reactions 2 and 4 (or 4a). Addition to alkenes is described by reactions 1–3, 4, and 5–7 and the corresponding rate eqns. (1)–(4a). Addition to the carbonyl carbon atom of the free (unsolvated) form of formaldehyde is represented by reactions 1, 1a, 2–4 (the main products are a 1,2-alkanediol, a carbonyl compound, and methanol), and 5-7 and is described by eqns. (5) and (6). In the case of hydroxymethyl addition, the process includes reactions 1, 1a, 2, 3, 5a, 4 (the main product is ethanediol), and 5–7 and is described by eqn. (9). If the nonchain formation of ethanediol in reaction 5 is ignored, the process can be described by eqn. (5). Addition to the oxygen molecule is described by reactions 1, 1a, 2–3b, 4a (the main products are an alkyl hydroperoxide, alcohols, carbonyl compounds, and water), and 5–7 and eqns. (10) and (11).

The main molecular products of the chain process i.e., R_3A, R′R″CO, and R_4A result from chain propagation reactions 3, 3a, and 3b through the reactive free radical $R_1^{\bullet}$ or $R_4^{\bullet}$, R′R″CO. The competing reaction 4, which opposes this chain propagation, yields the by-product R_3B a nonchain mechanism. The rate of formation of the products is a complicated function of the formation rates ($V_{3a} = V_{3b}$) and disappearance rates of the free radicals $R_1^{\bullet}$ and $R_{2(2a)}^{\bullet}$: $V(R_3A, R'R''CO, R_4A, R_3B) = V_2 = V_3 + V_{3a} + V_{4(4a)} = (V_{1a} + V_3 + V_{3b} - V_5) - (V_{1b} + V_{4(4a)} - V_7)$. The rates of reactions 5-7 at $k_{1b} = 0$ ($[R_1A] >> [R_2B]$) are given by eqns. (12)–(14). The rate ratios of the competing reactions are $V_3/V_{4(4a)} = \alpha l/x$ and $V_{3a}/V_{4(4a)} = \beta/x$ (where $\alpha = k_3/k_{4(4a)}$, $\beta = k_{3a}/k_{4(4a)}$ mol dm^{-3}, and l and x are the molar concentrations of the reactants R_1A and R_2B, respectively), and the chain length is $\nu = (V_3 + V_{3a})/V_1$. Unlike the dependences of the rates of reactions 4a (or 4 at $k_{1b} = 0$, with $V_{4(4a)} \le V_1$), 5, and 7 (for the last two – eqns. (12) and (14)), the dependences of the rates V of reactions 3, 3a,b, 4 (at $k_{1b} \neq 0$), and 6 (eqns. (1), (3)–(6), (10), (11), and (13)) on x have a maximum. Reaction 1b, which competes with reaction 1a, gives rise to a maximum in the dependence described by eqn. (2), whereas reaction 4 or 4a, competing with reactions 3 and 3a,b, is responsible for the maxima in the dependences defined by eqns. (1), (3)–(6) or (10) and (11). The low-reactive radicals $R_2^{\bullet}$ and $R_{2a}^{\bullet}$, resulting from reactions 4 and 4a, inhibit the nonbranched-chain addition of $R_1^{\bullet}$ to alkenes (or formaldehyde) and dioxygen, respectively. The stabilization energy of the low-reactive free radicals $CH_2{=}C(CH_3)\dot{C}H_2$, $CH_2{=}CH\dot{C}HOH$, and $H\dot{C}{=}O$ in the standard state in the gas phase is –52.0, –42.1, and –24.3 kJ mol^{-1}, respectively.[4,99] Reaction 4a leads to non-productive loss of $R_3^{\bullet}$ adduct radicals.

For approximate estimation of the parameters of the kinetic equations (3), (4), (10), and (11), eqn. (4) under the conditions (a) $k_2x^2 << (\alpha l + x)\sqrt{2k_5V_1}$ (ascending branch of a peaked curve) and (b) $k_2x^2 >> (\alpha l + x)\sqrt{2k_5V_1}$ (descending branch) is transformed into simple functions (direct and inverse proportionality, respectively) of the concentration x of the unsaturated compound. These functions allow

tentative estimates of the parameters k_2 and α to be derived from the experimental product formation rate V provided that V_1 and $2k_5$ are known:

$$V_{3,4} = \sqrt{V_1}k_2x/\phi\sqrt{2k_5}, \quad (15)$$

$$V_{3,4} = (V_1/\varphi)[(\alpha l/x) + 1], \quad (16)$$

where $\varphi = 1$ under conditions (a) and (b) and $\varphi = 2$ at the point of maximum (where $k_2x^2 \cong (\alpha + x)\sqrt{2k_5V_1}$). Equations (10) and (11) under the condition $k_2x^2 >> (\alpha l + \beta + x)\sqrt{2k_5V_1}$ (descending branch of a peaked curve) can be transformed into eqns. (17) and (18), respectively, which express the simple, inversely proportional dependences of reaction rates on x and provide tentative estimates of α and β:

$$V_3 = V_1\alpha l/\varphi x, \quad (17)$$

$$V_{3a} = V_1\beta/\varphi x, \quad (18)$$

where $\varphi = 2$ at the point of maximum (where $k_2x^2 \cong (\alpha l + \beta + x)\sqrt{2k_5V_1}$) and $\varphi = 1$ for the descending branch of the curve. Equation (3) for $V_{3,4}$ under condition (b) transforms into eqn. (17).

For radiation-chemical processes, the rates V in the kinetic equations should be replaced with radiation-chemical yields G using the necessary unit conversion factors and the relationships $V = GP$ and $V_1 = \varepsilon_1 G(R_1^{\bullet})P$, where P is the dose rate, ε_1 is the electron fraction of the saturated component R_1A in the reaction system [100], and $G(R_1^{\bullet})$ is the initial yield of the chain-carrier free radicals (addends) – initiation yield.[39,94]

Conclusions

In summary, the material on the kinetics of nonbranched-chain addition of free saturated radicals to multiple bonds of alkene (and its derivative), formaldehyde, or oxygen molecules makes it possible to describe, using rate eqns. (1)–(6), (9)–(11) obtained by quasi-steady-state treatment, experimental dependences with a maximum of the formation rates of molecular 1:1 adducts on the concentration of an unsaturated compound over the entire region of its change in binary reaction systems consisting of saturated and unsaturated components (Figures 1, 3, 4).

The proposed addition mechanism involves the reaction of a free 1:1 adduct radical with an unsaturated molecule yielding a low-reactive free radical (the reaction 4 competing with the chain propagation reactions in Schemes 1–5). In such reaction systems, the unsaturated compound is both a reactant and an autoinhibitor, specifically, a source of low-reactive free radicals shortening kinetic chains. The progressive inhibition of the nonbranched-chain processes, which takes place as the concentration of the unsaturated compound is raised (after the maximum process rate is reached), can be an element of the self-regulation of the natural processes that returns them to the stable steady state.

A similar description is applicable to the nonbranched-chain free-radical hydrogen oxidation in water at 296 K[63] (Figure 4, curve *2*). Using the hydrogen oxidation mechanism considered here, it has been demonstrated that, in the Earth's upper atmosphere, the decomposition of O_3 in its reaction with the $HO^{\bullet}$ radical can occur *via* the addition of the latter to the ozone molecule, yielding the $HO_4^{\bullet}$ radical, which is capable of efficiently absorbing UV radiation.[82]

The optimum concentration x_m of unsaturated component in the binary system at which the process rate is maximal can be derived with the help of obtained kinetic equations (3a), (4a), (10a), and (11a) or from the corresponding analytical expressions for k_2 if other parameters are known. This opens a way to intensification of some technological processes that are based on the addition of free radicals to the double bonds of unsaturated molecules and occur *via* a nonbranched-chain mechanism through the formation of 1:1 adducts.

References

[1]Gurvich, L. V., Karachevtsev, G. V., Kondrat'ev, V. N., Lebedev, Yu. A., Medvedev, V. A., Potapov, V. K., and Khodeev, Yu. S., "*Energii razryva khimicheskikh svyazei. Potentsialy ionizatsii i srodstvo k elektronu" ("Bond Dissociation Energies, Ionization Potentials, and Electron Affinity*"), Kondrat'ev, V. N., Editor, Nauka, Moscow, **1974**.

[2]Benson, S. W., "*Thermochemical Kinetics: Methods for the Estimation of Thermochemical Data and Rate Parameters*", 2nd Edition, Wiley, New York, **1976**.

[3]Pedley, J. B., Naylor, R. D., and Kirby, S. P., "*Thermochemical Data of Organic Compounds*", 2nd Edition, Chapman & Hall, London, **1986**. https://doi.org/10.1007/978-94-009-4099-4

[4]Orlov, Yu. D., Lebedev, Yu. A., and Saifullin, I. Sh., "Termokhimiya organicheskikh svobodnykh radikalov" ("Thermochemistry of Organic Free Radicals"), A. M. Kutepov, Editor., Nauka, Moscow, **2001**.

[5]Walling, Ch., "*Free Radicals in Solution*", Wiley, New York, **1956**.

[6]Emanuel, N. M., Denisov, E. T., and Maizus, Z. K., "*Tsepnye reaktsii okisleniya uglevodorodov v zhidkoi faze" ("Chain Oxidation Reactions of Hydrocarbons in the Liquid Phase"*), Nauka, Moscow, **1965**.

[7]Poluektov, V. A., Babkina, E. I., and Begishev, I. R., "On the Dependence of the Rate of a Chain Reaction on the Reactant Ratio", *Dokl. Akad. Nauk SSSR*, **1974**, *215*, 649–652.

[8]Silaev, M. M. and Bugaenko, L. T., "Mathematical Simulation of the Kinetics of Radiation Induced Hydroxyalkylation of Aliphatic Saturated Alcohols", *Radiat. Phys. Chem.,* **1992**, *40*, 1–10. https://doi.org/10.1016/1359-0197(92)90131-X

[9]Silaev, M. M. and Bugaenko, L. T., "Kinetics of the Addition of α-Hydroxyalkyl Radicals to 2-Propen-1-ol and Formaldehyde", *Kinet. Katal.*, **1994**, *35*, 509–513.

[10]Silaev, M. M., "Competition Kinetics of Nonbranched Chain Processes of Free-Radical Addition to Double Bonds of Molecules with the Formation of 1:1 Adducts", *Kinet. Katal.*, **1999**, *40*, 281–284, English Translation in: *Kinetics and Catalysis*, **1999**, *40*, 256–259.

[11]Silaev, M. M., "Simulation of the Nonbranched-Chain Addition of Saturated Free Radicals to Alkenes and Their Derivatives Yielding 1:1 Adducts", *Teor. Osnov. Khim. Tekhnol.*, **2007**, *41*, 280–295, English Translation in: *Theor. Found. Chem. Eng.*, **2007**, *41*, 273–278. https://doi.org/10.1134/S0040579507030062

[12]Silaev, M. M., "Simulation of Nonbranched Chain Processes for Producing 1,2-Alkanediols in Alcohol–Formaldehyde Systems", *Teor. Osnov. Khim. Tekhnol.*, **2007**, *41*, 379–384, English Translation in: *Theor. Found. Chem. Eng.*, **2007**, *41*, 357–361. https://doi.org/10.1134/S0040579507040045

[13]Silaev, M. M., "A New Competitive Kinetic Model of Radical Chain Oxidation: Oxygen as an Autoinhibitor", *Biofizika*, **2001**, *46*, 203–209, English Translation in: *Biophysics*, **2001**, *46*, 202–207.

[14]Silaev, M. M., "Simulation of the Initiated Addition of Hydrocarbon Free Radicals and Hydrogen Atoms to Oxygen *via* a Nonbranched Chain Mechanism", *Teor. Osnov. Khim. Tekhnol.*, **2007**, *41*, 634–642, English Translation in: *Theor. Found. Chem. Eng.*, **2007**, *41*, 831–838. https://doi.org/10.1134/S0040579507060073

[15]Bard, Y., *Nonlinear Parameter Estimation*, Academic Press, New York, **1974**.

[16]Bateman, L., "Alkene Oxidation", *Quart. Rev.*, **1954**, *8*, 147–167. https://doi.org/10.1039/qr9540800147

[17]Urry, W. H., Stacey, F. W., Huyser, E. S., and Juveland, O. O., "The Peroxide- and Light-Induced Additions of Alcohols to Alkenes", *J. Am. Chem. Soc.*, **1954**, *76*, 450–455. https://doi.org/10.1021/ja01631a037

[18]Urry, W. H., Juveland, O. O., *J. Am. Chem. Soc.*, **1958**, *80*, 3322–3328. https://doi.org/10.1021/ja01546a033

[19]Shostenko, A. G., Zagorets, P. A., Dodonov, A. M., and Greish, A. A., "γ-Radiation-Induced Addition of Phosphorus Trichloride to Isobutylene", *Khim. Vys. Energ.*, **1970**, *4*, 357.

[20]Kim, V., Shostenko, A. G., and Gasparyan, M. D., "Reactivity of Polychloroalkyl Radicals in the Telomerization of CCl_4 with 1-Propene and 2-Methyl-1-Propene" (in Russian), *React. Kinet. Catal. Lett.*, **1979**, *12*, 479–484.

[21]Myshkin, V. E., Shostenko, A. G., Zagorets, P. A., Markova, K. G., and Pchelkin, A. I., "Determination of Absolute Rate Constants for the Addition of the Ethyl Radical to Alkenes", *Teor. Eksp. Khim.*, **1977**, *13*, 266–271.

[22]Zamyslov, R. A., Shostenko, A. G., Dobrov, I. V., and Tarasova, N. P., "Kinetics of γ-Radiation-Induced Reactions of 2-Propanol with Trifluoropropene and Hexaflu-oropropene", *Kinet. Katal.*, **1987**, *28*, 977–979.

[23]Silaev, M. M., "Dependence of Radiation-chemical γ-Diol Yields on the 2-Propen-1-ol Concentration in the Radiolysis of Aliphatic Saturated C_1-C_3 Alcohol + 2-Propen-1-ol Systems", *Khim. Vysok. Energ.*, **1990**, *24*, 282–283.

[24]Silaev, M. M., "γ-Diol Formation *via* the Autooxidation of 2-Propen-1-ol Solutions in Saturated Alcohols", *Vestn. Moskovsk. Univ., Ser. 2: Khim.*, **1994**, *35*, 40–42.

[25]Bugaenko, L. T., Kuzmin, M. G., and Polak, L. S., "*High-Energy Chemistry"*, Horwood Hall, New York, **1993**, p. 112.

[26]Thomas, J. K., "Pulse Radiolysis of Aqueous Solutions of Methyl Iodide and Methyl Bromide. The Reactions of Iodine Atoms and Methyl Radicals in Water" *J. Phys. Chem.*, **1967**, *71*, 1919–1925. https://doi.org/10.1021/j100865a060

[27]Walker, J. F., *Formaldehyde*, Reinhold, New York, 1953, English Translation under the title *Formal'degid*, Goskhimizdat, Moscow, **1957**, p. 106.

[28]Silaev, M. M., Rudnev, A. V., and Kalyazin, E. P., "Formaldehyde. III. Concentration of Free Formaldehyde as a Function of Temperature, Polarity of Solvents, and Total Concentration of Formaldehyde in Solution", *Zh. Fiz. Khim.*, **1979**, 53, 1647–1651.

[29]Oyama, M., "A Free-Radical Reaction of Primary and Secondary Alcohols with Formaldehyde", *J. Org. Chem.*, **1965**, *30*, 2429–2432. https://doi.org/10.1021/jo01018a079

[30]Nikishin, G. I., Lefor, D., and Vorob'ev, E. D., "Free Radical Reaction of Primary Alcohols with Formaldehyde", *Izv. Akad. Nauk SSSR, Ser. Khim.*, **1966**, *7*, 1271–1272. https://doi.org/10.1007/BF00847774

[31]Dzhurinskaya, M. B., Rudnev, A. V., and Kalyazin, E. P., "High Temperature UV Photolysis of Formaldehyde in Liquid Methanol", *Vestn. Moskovsk. Univ., Ser. 2: Khim.*, **1984**, *25*, 173–176.

[32]Kalyazin, E. P., Petryaev, E. P., and Shadyro, O. I, "Reaction between Oxyalkyl Radicals and Aldehydes", *Zh. Org. Khim.*, **1977**, *13*, 293–295.

[33]Novoselov, A. I., Silaev, M. M., and Bugaenko, L. T., "Effect of Temperature on the Yields of Final Products in the γ-Radiolysis of Formaldehyde Solutions in C_1-C_3 Alkanols", *Khim. Vysok. Energ.*, **2004**, *38*, 270–272, English Translation in: *High Energy Chem.*, **2004**, *38*, 236–238. https://doi.org/10.1023/B:HIEC.0000035410.87205.09

[34]Novoselov, A. I., Silaev, M. M., and Bugaenko, L. T., "Dependence of Ethanediol Yield on Formaldehyde Concentration in γ-Radiolysis of Methanol–Formaldehyde System at 373–473 K", *Khim. Vysok. Energ.*, **2008**, *42*, 74–75, English Translation in: *High Energy Chem.*, **2008**, *42*, 69–70. https://doi.org/10.1134/S0018143908010141

[35]Novoselov, A. I., Silaev, M. M., and Bugaenko, L. T., "γ-Induced Single-Step Synthesis of Ethylene Glycol from Methanol–Formaldehyde Solution", *Theor. Osnov. Khim. Tekhnol.*, **2010**,*44*, 450–453, English Translation in: *Theor. Found. Chem. Eng.*, **2010**, *44*, 432–435. https://doi.org/10.1134/S0040579510040111

[36]Novoselov, A. I., Silaev, M. M., and Bugaenko, L. T., "Dependence of 1,2-Propanediol Yield on Formaldehyde Concentration in γ-Radiolysis of Ethanol–Formaldehyde System at 373473 K", *Khim. Vysok. Energ.*, **2007**, *41*, 58, English Translation in: *High Energy Chem.*, **2007**, *41*, 53. https://doi.org/10.1134/S0018143907010110

[37]Pshezhetskii, S. Ya., Kotov, A. G., Milinchuk, V. K., Roginskii, V. A., and Tupikov, V. I., "*EPR svobodnykh radikalov v radiatsionnoi khimii"* ("ESR of Free Radicals in Radiation Chemistry"), Khimiya, Moscow, **1972**.

[38]Silaev, M. M., "Estimating the Solvent Concentration in Formaldehyde Solutions at Various Temperatures", *Zh. Fiz. Khim.*, **1993**, *67*, 1944.

[39]Silaev, M. M., "Applied Aspects of the γ-Radiolysis of C_1-C_4 Alcohols and Binary Mixtures on Their Basis", *Khim. Vysok. Energ.*, Vol. 36, No. 2, 2002, pp. 97–101, English Translation in: *High Energy Chem.*, **2002**, *36*, 70–74. https://doi.org/10.1023/A:1014650726821

[40]Silaev, M. M., Bugaenko, L. T., and Kalyazin, E. P., "On the Possibility of Adequately Estimating the Rate Constants for the Reaction of Hydroxyalkyl Radicals with Each Other Using the Self-Diffusion Coefficients or Viscosities of the Corresponding Alcohols", *Vestn. Moskovsk.. Univ, Ser. 2: Khim.*, **1986**, *27*, 386–389.

[41]Shadyro, O. I., "*Radiation-chemical Conversions of Aldehydes in Various Systems"*, Ph.D. Thesis (Chemistry), Belarusian State University, Minsk, **1975**.

[42]Silaev, M. M., "Relative Reactivity of α-Hydroxyethyl Radicals for 2-Propene-1-ol and Formaldehyde Double-Bond Addition", *Vestn. Moskovsk. Univ., Ser. 2: Khim.*, **1993**, *34*, 311.

[43]Seki H., Nagai, R., and Imamura, M., "γ-Radiolysis of a Binary Mixture of Methanol and Water. The Formation of Formaldehyde in the Radiolysis of Liquid Methanol", *Bull. Chem. Soc. Japan..*, **1968**, *41*, 2877–2881. https://doi.org/10.1246/bcsj.41.2877

[44]Shtern, V. Ya., "*Mekhanizm okisleniya uglevodorodov v gazovoi faze* (Mechanism of the Gas-Phase Oxidation of Hydrocarbons)", Akademiya Nauk SSSR, Moscow, **1960**.

[45]Bäckström, H. L. J., "Der Kettenmechanismus bei der Autoxydation von Aldehyden", *Z. Phys. Chem. (B)"*, **1934**, *25*, 99–121. https://doi.org/10.1515/zpch-1934-2509

[46]Aliev, A. A. and Saraeva, V. V., "Isomerization of Peroxy Radicals Resulting from the Radiation-Induced Oxidation of

o-Xylene", *Vestn Moskovsk. Univ., Ser. 2: Khim.*, **1983**, *34*, 371–374.

[47]Badin, E. J., "The Reaction between Atomic Hydrogen and Molecular Oxygen at Low Pressures. Surface Effects", *J. Am. Chem. Soc.*, **1948**, *70*, 3651–3655. https://doi.org/10.1021/ja01191a032

[48]Buchachenko, A. L., "*Kompleksy radikalov i molekulyarnogo kisloroda s organicheskimi molekulami"* ("Complexes of Radicals and Dioxygen with Organic Molecules"), Beletskaya, I. P., Editor, Nauka, Moscow, **1984**.

[49]Francisco, J. S. and Williams, I. H., "The Thermochemistry of Polyoxides and Polyoxy Radicals", *Int. J. Chem. Kinet.*, **1988**, *20*, 455–466. https://doi.org/10.1002/kin.550200605

[50]Kokorev, V. N., Vyshinskii, N. N., Maslennikov, V. P., Abronin, I. A., Zhidomirov, G. M., and Aleksandrov, Yu. A., "Electronic Structure and Chemical Reactions of Peroxides: I. MINDO/3 Calculation of the Geometry and Enthalpy of Formation of the Ground States of Organic and Organoelement Peroxides", *Zh. Strukt. Khim.*, **1981**, *22*, *4*, 9–15.

[51]Dmitruk, A. F., Lobanov, V. V., and Kholoimova, L. I., "Role of Tetroxide Conformation in the Mechanism of Peroxy Radical Recombination", *Teor. Eksp. Khim.*, **1986**, *22*, 363–366.

[52]Belyakov, V. A., Vasil'ev, R. F., Ivanova, N. M., Minaev, B. F., Osyaeva, O. V., and Fedorova, G. F., "Electronic Model of the Excitation of Chemiluminescence in the Oxidation of Organic Compounds", *Izv. Akad. Nauk SSSR, Ser.: Fiz.*, **1987**, *51*, 540–547.

[53]Ase, P., Bock, W., and Snelson, A., "Alkylperoxy and Alkyl Radicals. 1. Infrared Spectra of CH_3O_2 and $CH_3O_4CH_3$ and the Ultraviolet Photolysis of CH_3O_2 in Argon + Oxygen Matrices", *J. Phys. Chem.*, **1986**, *90*, 2099–2109. https://doi.org/10.1021/j100401a024

[54]Pimentel G. C. and McClellan, A. L., "*The Hydrogen Bond"*, L. Pauling, Editor, Freeman, San Francisco, **1960**, 200.

[55]Russell, G. A., "Deuterium-Isotope Effects in the Autooxidation of Aralkyl Hydrocarbons: Mechanism of the Interaction of Peroxy Radicals", *J. Am. Chem. Soc.*, **1957**, *79*, 3871–3877. https://doi.org/10.1021/ja01571a068

[56]Silaev, M. M., "The Competition Kinetics of Nonbranched Chain Processes of Free-Radical Addition to Double Bonds of Molecules with the Formation of 1:1 Adducts and the Inhibition by the Substrate", *Oxid. Commun.*, **1999**, *22*, 159–170.

[57]Silaev, M. M., "The Competition Kinetics of Radical-Chain Addition", *Zh. Fiz. Khim.*, Vol. 73, No. 7, 1999, pp. 1180–1184, English Translation in: *Russ. J. Phys. Chem.*, **1999**, *73*, 1050–1054.

[58]Darmanyan, A. P., Gregory, D. D., Guo, Y., Jenks, W. S., Burel L., Eloy, D., and Jardon, P., "Quenching of Singlet Oxygen by Oxygen- and Sulfur-Centered Radicals: Evidence for Energy Transfer to Peroxy Radicals in Solution", *J. Am. Chem. Soc.*, **1998**, *120*, 396–403. https://doi.org/10.1021/ja9730831

[59]Kanofsky, J. R., "Singlet Oxygen Production from the Reactions of Alkylperoxy Radicals. Evidence from 1268-nm Chemiluminescence", *J. Org. Chem.*, **1986**, *51*, 3386–3388. https://doi.org/10.1021/jo00367a032

[60]Semenov, N. N., "*Tsepnye reaktsii"* ("Chain Reactions"), Goskhimtekhizdat, Leningrad, **1934**, 241, 203.

[61]Reznikovskii, M., Tarasova, Z., and Dogadkin, B., "Oxygen Solubility in Some Organic Liquids", *Zh. Obshch. Khim.*, **1950**, *20*, 63–67.

[62]Howard, J. A. and Ingold, K. U., "Absolute Rate Constants for Hydrocarbon Autooxidation. VI. Alkyl Aromatic and Alkeneic Hydrocarbons", *Can. J. Chem.*, **1967**, *45*, 793–802. https://doi.org/10.1139/v67-132

[63]Barr, N. F. and Allen, A. O., "Hydrogen Atoms in the Radiolysis of Water", *J. Phys. Chem.*, **1959**, *63*, 928–931. https://doi.org/10.1021/j150576a037

[64]Smith, H. A. and Napravnik, A., "Photochemical Oxidation of Hydrogen", *J. Am. Chem. Soc.*, **1940**, *62*, 385–393. https://doi.org/10.1021/ja01859a043

[65]Pagsberg, P. B., Eriksen, J., and Christensen, H. C., "Pulse Radiolysis of Gaseous Ammonia–Oxygen Mixtures", *J. Phys. Chem.*, **1979**, *83*, 582–590. https://doi.org/10.1021/j100468a006

[66]Silaev, M. M., "Competitive Mechanism of the Non-branched Radical Chain Oxidation of Hydrogen Involving the Free Cyclohydrotetraoxyl Radical [ȮȮ···H···ȮȮ]•, Which Inhibits the Chain Process", "*Khim. Vysok. Energ.*, **2003**, *37*, 27–32, English Translation in: *High Energy Chem.*, **2003**, *37*, 24–28. https://doi.org/10.1023/A:1021909509430

[67]Silaev, M. M., "Simulation of Initiated Nonbranched Chain Oxidation of Hydrogen: Oxygen as an Autoinhibitor", *Khim. Vysok. Energ.*, **2008**, *42*, 124–129, English Translation in: *High Energy Chem.*, 2008, *42*, 95–100. https://doi.org/10.1134/S0018143908020069

[68]McKay, D. J. and Wright, J. S., "How Long Can You Make an Oxygen Chain?", *J. Am. Chem. Soc.*, **1998**, *120*, 1003–1013. https://doi.org/10.1021/ja971534b

[69]Lipikhin, N. P., "Dimers, Clusters, and Cluster Ions of Oxygen in the Gas Phase", *Usp. Khim.*, **1975**, *44*, 366–376. https://doi.org/10.1070/RC1975v044n08ABEH002366

[70]Razumovskii, S. D., "*Kislorod – elementarnye formy i svoistva"* ("Oxygen: Elementary Forms and Properties"), Khimiya, Moscow, **1979**.

[71]Dunn, K. M., Scuceria, G. E., and Schaefer III, H. F., "The infrared spectrum of cyclotetraoxygen, O_4: a theoretical investigation employing the single and double excitation coupled cluster method", *J.Chem. Phys.*, **1990**, *92*, 6077–6080. https://doi.org/10.1063/1.458380

[72]Brown L. and Vaida V., "Photoreactivity of Oxygen Dimers in the Ultraviolet", *J. Phys. Chem.*, **1996**, *100*, 7849–7853. https://doi.org/10.1021/jp9526713

[73]Aquilanti, V., Ascenzi, D., Bartolomei, M., Cappelletti, D., Cavalli, S., de Castro-Vitores, V, and Pirani, F., "Molecular Beam Scattering of Aligned Oxygen Molecules. The Nature of the Bond in the O_2–O_2 Dimer", *J. Am. Chem. Soc.*, **1999**, *121*, 10794–1080. https://doi.org/10.1021/ja9917215

[74]Cacace, F., de Petris, G., and Troiani, A., "Experimental Detection of Tetraoxygen", *Angew. Chem., Int. Ed.* (in English), **2001**, *40*, 4062–4065. https://doi.org/10.1002/1521-3773(20011105)40:21<4062::AID-ANIE4062>3.0.CO;2-X

[75]Taylor, H. S., "Photosensitisation and the Mechanism of Chemical Reactions", *Trans. Faraday Soc.*, **1926**, 63(3), 560–568.

[76]Nalbandyan, A. B. and Voevodskii, V. V., "*Mekhanizm okisleniya i goreniya vodoroda"* ("Mechanism of Hydrogen Oxidation and Combustion"), Kondrat'ev, V. N., Editor, Akad. Nauk SSSR, Moscow, **1949**.

[77]Foner, S. N. and Hudson, R. L., "Mass spectrometry of the HO_2 free radical", *J. Chem. Phys.*, **1962**, *36*, 2681. https://doi.org/10.1063/1.1732352

[78]Hochanadel, C. J., Ghormley, J. A., and Ogren, P. J., "Absorption Spectrum and Reaction Kinetics of the HO_2 Radical in the Gas Phase", *J. Chem. Phys.*, **1972**, *56*, 4426–4432. https://doi.org/10.1063/1.1677885

[79]Robertson, J. B., "A Mass Spectral Search for H_2O_4 and HO_4 in a Gaseous Mixture Containing HO_2 and O_2", *Chem. Ind.*, **1954**, no. 48, 1485.

[80]Bahnemann, D. and Hart, E. J., "Rate Constants of the Reaction of the Hydrated Electron and Hydroxyl Radical with Ozone

in Aqueous Solution", *J. Phys. Chem.*, **1982**, *86*, 252–255. https://doi.org/10.1021/j100391a024

[81] *"Vodorodnaya svyaz': Sbornik statei"* ("The Hydrogen Bonding: Collection of Articles") Sokolov, N. D., Editor, Nauka, Moscow, **1981**.

[82]Staehelin, J., Bühler, R. E., and Hoigné, J., "Ozone Decomposition in Water Studied by Pulse Radiolysis. 2. OH and HO_4 as Chain Intermediates", *J. Phys. Chem.*, **1984**, *88*, 5999–6004. https://doi.org/10.1021/j150668a051

[83]Cacace, F., de Petris, G., Pepi, F., and Troiani, A., "Experimental Detection of Hydrogen Trioxide", *Science*, **1999**, *285*, 81–82. https://doi.org/10.1126/science.285.5424.81

[84]Bühler, R. F., Staehelin, J., and Hoigné, J., "Ozone Decomposition in Water Studied by Pulse Radiolysis. 1. HO_2/O_2^- and HO_3/O_3^- as Intermediates", *J. Phys. Chem.*, **1984**, *88*, 2560–2564. https://doi.org/10.1021/j150656a026

[85]Trushkov, I. V., Silaev, M. M., and Chuvylkin, N. D., "Acyclic and Cyclic Forms of the Radicals $HO_4^{\bullet}$, $CH_3O_4^{\bullet}$, and $C_2H_5O_4^{\bullet}$: *Ab Initio* Quantum Chemical Calculations", *Izv. Akad. Nauk, Ser.: Khim.*, **2009**, no. 3, 479–482, English Translation in: *Russ. Chem. Bull., Int. Ed.*, **2009**, *58*, 489–492.

[86]Mansergas, A., Anglada, J. M., Olivella, S., Ruiz-López, M. F., "On the Nature of the Unusually Long OO Bond in HO_3 and HO_4 Radicals", *Phys. Chem. Chem. Phys.*, **2007**, *9*, 5865–5873. https://doi.org/10.1039/b711464h

[87]Wong, W. and Davis, D. D., "A Flash Photolysis Resonance Fluorescence Study of the Reactions of Atomic Hydrogen and Molecular Oxygen: $H + O_2 + M \rightarrow HO_2 + M$", *Int. J. Chem. Kinet.*, **1974**, *6*, 401–416. https://doi.org/10.1002/kin.550060310

[88]Xu, X., Muller, R. P., and Goddard III, W. A., "The Gas Phase Reaction of Singlet Dioxygen with Water: a Water-Catalyzed Mechanism", *Proc. Natl. Acad. Sci. USA*, **2002**, *99*, 3376–3381. https://doi.org/10.1073/pnas.052710099

[89]Seidl, E. T. and Schaefer III, H. F., "Is There a Transition State for the Unimolecular Dissociation of Cyclotetraoxygen (O_4)?", *J. Chem. Phys.*, **1992**, *96*, 1176–1182. https://doi.org/10.1063/1.462205

[90]Hernández-Lamoneda, R. and Ramírez-Solís, A., "Reactivity and Electronic States of O_4 along Minimum Energy Paths", *J. Chem. Phys.*, **2000**, *113*, 4139–4145. https://doi.org/10.1063/1.1288370

[91]Varandas, A. J. C. and Zhang, L., "Test Studies on the Potential Energy Surface and Rate Constant for the OH + O_3 Atmospheric Reaction", *Chem. Phys. Lett.*, **2000**, *331*, 474–482. https://doi.org/10.1016/S0009-2614(00)01222-7

[92] *"Atmosfera. Spravochnik"* ("Atmosphere: A Handbook"), Gidrometeoizdat, Leningrad, **1991**.

[93]Okabe, H., "*Photochemistry of Small Molecules"*, Wiley, New York, **1978**.

[94]Pikaev, A. K., "*Sovremennaya radiatsionnaya khimiya. Radioliz gazov i zhidkostei"* ("Modern Radiation Chemistry: Radiolysis of Gases and Liquids"), Nauka, Moscow, **1986**.

[95]Boyd, A. W., Willis, C., and Miller, O. A., "A Re-examination of the Yields in the High Dose Rate Radiolysis of Gaseous Ammonia", *Can. J. Chem.*, **1971**, *49*, 2283–2289. https://doi.org/10.1139/v71-369

[96]Silaev, M. M., "Competition Mechanism of Substrate-Inhibited Radical Chain Addition to Double Bond", *Neftekhimiya*, Vol. **2000**, *40*, 33–40, English Translation in: *Peroleum Chem.*, **2000**, *40*, 29–35.

[97]Silaev, M. M.,"Competition Kinetics of Nonbranched Chain Processes of Free Radical Addition to the C=C, C=O, and O=O Double Bonds of Molecules", *Neftekhimiya*, **2003**, *43*, 302–307, English Translation in: *Petroleum Chem.*, **2003**, *43*, 258–273.

[98]Silaev, M. M., "Low-reactive Free Radicals Inhibiting Nonbranched Chain Processes of Addition", *Biofizika*, **2005**, *50*, 585–600, English Translation in: *Biophysics*, **2005**, *50*, 511–524.

[99]Sanderson, R. T. ,"Radical Reorganization and Bond Energies in Organic Molecules", *J. Org. Chem.*, **1982**, *47*, 3835–3839. https://doi.org/10.1021/jo00141a006

[100]Vereshchinskii, I. V. and Pikaev, A. K., "*Vvedenie v radiatsionnuyu khimiyu"* ("Introduction to Radiation Chemistry"), Spitsyn, V.I., Editor, Akademiya Nauk SSSR, Moscow, **1963**, 190.

Received: 10.05.2018.
Accepted: 14.06.2018.

Appendix

The experimental concentrations x (mol dm^{-3}) of free formaldehyde at different temperatures T (K) and total formaldehyde concentrations c_0 (mol dm^{-3}) in various solvents

c_0	T	10^2x	c_0	T	10^2x	c_0	T	10^2x	c_0	T	10^2x
Water			4.44	389	5.20	4.0	381	5.00	1.8	371	2.08
1.0	358	0.78	4.44	405	7.50	4.0	397	8.80	1.8	393	6.00
1.0	387	2.22	4.44	418	10.0	4.0	409	12.00	1.8	418	12.20
1.0	393	3.23	**Methanol**			6.2	347	2.80	1.8	438	16.70
1.0	407	4.55	1.0	375	0.33	6.2	376	7.80	3.0	343	1.25
2.0	353	1.44	1.0	395	1.00	6.2	393	12.50	3.0	375	5.40
2.0	387	4.70	1.0	423	2.90	**1-Propanol**			3.0	403	15.80
2.0	397	6.60	2.5	373	0.60	1.0	371	0.83	3.0	413	19.40
2.0	407	8.55	2.5	385	1.15	1.0	393	2.10	5.6	343	2.80
4.0	343	0.78	2.5	398	1.80	1.0	413	4.30	5.6	358	3.35
4.0	363	2.33	5.4	351	0.78	1.0	435	7.65	5.6	363	5.80
4.0	385	6.45	5.4	383	3.70	1.9	353	0.70	5.6	371	6.50
4.0	403	8.90	5.4	398	6.80	1.9	383	3.06	5.6	383	12.10
4.0	413	11.10	7.0	365	4.70	1.9	405	7.65	**2-Methyl-2-propanol**		
6.0	351	2.22	7.0	383	12.50	1.9	417	11.70	1.0	347	1.20
6.0	375	6.70	7.0	391	16.00	4.0	349	1.67	1.0	367	4.50
6.0	389	10.70	**Ethanol**			4.0	373	6.10	1.0	387	11.00
6.0	398	14.10	1.0	367	0.33	4.0	393	13.30	1.0	398	19.30
8.4	364	5.50	1.0	387	0.67	6.0	338	1.39	2.0	335	1.10
8.4	376	8.32	1.0	397	1.45	6.0	357	5.00	2.0	357	4.30
8.4	388	10.97	1.0	413	2.70	6.0	377	11.70	2.0	375	13.00
Ethanediol			1.0	423	4.00	6.0	389	18.30	2.0	383	18.50
1.0	409	1.30	2.0	373	1.10	7.8	343	3.06	3.0	338	1.70
1.0	418	1.80	2.0	394	2.90	7.8	358	6.25	3.0	353	4.70
1.0	435	2.45	2.0	409	5.80	7.8	377	16.90	3.0	365	9.60
3.33	358	1.20	2.0	419	8.20	**2-Propanol**			3.0	373	15.50
3.33	387	3.30	3.0	361	1.20	1.0	365	0.98	6.0	345	6.90
3.33	401	5.10	3.0	387	3.70	1.0	393	3.05	6.0	351	9.00
3.33	415	7.20	3.0	409	7.80	1.0	411	6.00	6.0	361	13.40
4.44	338	1.00	4.0	355	2.30	1.0	433	10.40	6.0	365	18.30